

A THERMODYNAMICAL FRAMEWORK FOR THE SOLIDIFICATION OF
MOLTEN POLYMERS AND ITS APPLICATION TO FIBER EXTRUSION

A Dissertation

by

KRISHNA KANNAN

Submitted to the Office of Graduate Studies of
Texas A&M University
in partial fulfillment of the requirements for the degree of
DOCTOR OF PHILOSOPHY

December 2004

Major Subject: Mechanical Engineering

A THERMODYNAMICAL FRAMEWORK FOR THE SOLIDIFICATION OF
MOLTEN POLYMERS AND ITS APPLICATION TO FIBER EXTRUSION

A Dissertation

by

KRISHNA KANNAN

Submitted to Texas A&M University
in partial fulfillment of the requirements
for the degree of

DOCTOR OF PHILOSOPHY

Approved as to style and content by:

K.R. Rajagopal
(Chair of Committee)

J.D. Humphrey
(Member)

J.R. Walton
(Member)

I. Karaman
(Member)

Dennis O'Neal
(Head of Department)

December 2004

Major Subject: Mechanical Engineering

ABSTRACT

A Thermodynamical Framework for the Solidification of Molten Polymers and Its
Application to Fiber Extrusion. (December 2004)

Krishna Kannan, B.E., PSG Tech, India;

M.S., Texas A&M University

Chair of Advisory Committee: Dr. K.R. Rajagopal

A thermodynamical framework is presented that describes the solidification of molten polymers to an amorphous as well as to a semicrystalline solid-like state. This framework fits into a general structure developed for materials undergoing a large class of entropy producing processes. The molten polymers are usually isotropic in nature and certain polymers crystallize, with the exception of largely atactic polymers, which solidify to an amorphous solid, to an anisotropic solid. The symmetry of the crystalline structures in the semicrystalline polymers is dependent upon the thermomechanical process to which the polymer is subjected to. The framework presented takes into account that the natural configurations associated with the polymer melt (associated with the breaking and reforming of the polymer network) and the solid evolve in addition to the evolving material symmetry associated with these natural configurations. The functional form of the various primitives such as how the material stores, dissipates energy and produces entropy are prescribed. Entropy may be produced by a variety of mechanisms such as conduction, dissipation, solidification, rearrangement of crystalline structures due to annealing and so forth. The manner in which the natural configurations evolve is dictated by the maximization of the rate of dissipation. Similarly, the crystallization and glass transition kinetics may be obtained by maximization of their corresponding entropy productions. The restrictions

placed by the second law of thermodynamics, frame indifference, material symmetry and incompressibility allows for a class of constitutive equations and the maximization of the rate of entropy production is invoked to select a constitutive equation from an allowable class of constitutive equations. Using such a unified thermodynamic approach, the popular crystallization equations such as Avrami equation and its various modifications such as Nakamura and Hillier and Price equations are obtained. The predictions of the model obtained using this framework are compared with the splot data for amorphous and semicrystalline polymers.

To my parents, Kannan and Subadhra

ACKNOWLEDGMENTS

I am greatly indebted to my teacher, Prof. Rajagopal who has been a great source of inspiration for me. His lectures have always been insightful, interesting and never the same. I learned a lot from him and in the process molded my thoughts. I also thank Prof. Walton, Prof. Humphrey and Prof. Karaman for serving on my committee. Dr. Luoyi Tao has always been my second source of inspiration. His perspicacity of thought and insight into any subject have always helped me. I thank Dr. Joga Rao for the useful discussions I had with him. I am indebted to my parents, uncles and aunts for offering their kind words of encouragement and support. Finally, I would like to thank Dr. Murali Krishnan.

TABLE OF CONTENTS

CHAPTER		Page
I	INTRODUCTION	1
	A. An introduction to structural development of polymers subjected to thermal and mechanical process	1
	B. Typical industrial processes	4
	1. Fiber spinning	4
	2. Other processes	4
	C. Need for modeling	5
	1. Design of a process	5
	2. Design of die set	5
	D. Natural configurations	5
	E. Earlier approaches	6
	1. Attempts based on describing the solidification of a polymer to a glassy state	7
	2. Attempts based on describing the solidification of a polymer to a semicrystalline solid	7
	F. Objectives and proposed methodology	9
II	A THERMOMECHANICAL FRAMEWORK FOR THE GLASS TRANSITION PHENOMENON IN CERTAIN POLYMERS AND ITS APPLICATION TO FIBER SPINNING*	11
	A. Introduction	11
	B. Kinematics	17
	C. Restrictions imposed on constitutive equations	19
	1. The second law of thermodynamics	19
	2. Material frame indifference	20
	D. Material symmetry	22
	E. Incompressibility	23
	F. Other restrictions	23
	G. Modeling the melt	23
	H. Modeling the mixture	27
	I. The fiber spinning problem	34
	1. Melt calculations	36
	2. Mixture calculations	40

CHAPTER	Page
3. Parameters used in the simulation	43
4. Boundary, initiation, and interface conditions	46
5. Results and conclusions	48
 III	
A THERMOMECHANICAL FRAMEWORK FOR THE TRANSITION OF A VISCOELASTIC LIQUID TO A VISCOELASTIC SOLID*	54
A. Introduction	54
B. Kinematics	57
C. Modeling the melt	60
1. An application of the melt model	67
D. Modeling the mixture	74
E. Modeling the solid	80
1. Relationship to the Standard Linear Solid (SLS)	82
2. An application of the model for solid	83
 IV	
FLOW INDUCED CRYSTALLIZATION IN FIBER SPINNING	87
A. Introduction	87
B. Kinematics	91
C. Modeling the melt and the semicrystalline solid	94
1. Modeling the melt	94
2. Modeling the semicrystalline solid	95
D. Fiber spinning	98
1. Melt equations	98
2. Mixture equations	100
3. Boundary, initiation and interface conditions	102
4. Parameters	103
a. Thin-filament approximation	103
b. Radial resolution approximation	109
5. Numerical method	112
E. Results	113
1. Thin-filament approximation	113
a. Effect of mass flow rate	113
b. Effect of quench air speed	117
c. Low speed spinning	119
d. Effect of capillary diameter	122
e. Effect of molecular weight	124
f. Effect of the type of polymer	126

CHAPTER	Page
g. Effect of additives	128
2. Radial resolution approximation	131
F. Summary and conclusions	136
V A THERMODYNAMICAL FRAMEWORK INCORPORATING THE EFFECT OF THE THERMAL HISTORY ON THE SOLIDIFICATION OF MOLTEN POLYMERS	138
A. Introduction	138
B. Kinematics	143
C. Modeling	144
D. Summary and conclusions	152
VI SUMMARY AND CONCLUSIONS	153
REFERENCES	155
VITA	165

LIST OF TABLES

TABLE		Page
I	The list of constants used in the simulation of fiber spinning problem	47
II	Processing conditions for various nylons from Doufas <i>et al.</i> [15] . . .	106
III	Parameters that are fixed in all the simulations	107
IV	Parameters that are dependent on simulation	108
V	The parameters used in the simulation.	109
VI	Take up force of BHS resin at a mass flow rate of 5.069 g/min. . . .	135
VII	Take up force of BHS resin at a mass flow rate of 2.993 g/min. . . .	136

LIST OF FIGURES

FIGURE	Page
1	The figure represents the configurations associated with the amorphous melt. \mathbf{X} is the position occupied by the particle in the reference configuration, κ_R . \mathbf{x} is the current position of the particle. 16
2	This figure represents the configurations associated with the mixture. The configuration associated with the material at the instant of initiation, the glassy state, is denoted by κ_r . \mathbf{F}_{κ_r} maps the infinitesimal material fibers in κ_r to the corresponding material fibers in κ_t 28
3	The above is a sketch of a fiber spinning process. Gravity acts along the length of the spinline. The melt exits the die at 300°C and swells to a diameter d_s ; melt simulations are performed from this point onwards. The length of the spinline, l , is 1.5 m. The mass flow rate of the melt, m , at the capillary exit is $4.167\text{e-}5$ Kg/sec. The diameter of the capillary is 0.25 mm. As the melt is cooled by the cross flow air at a velocity of v_a , the solidification is initiated at some distance along the axis of the fiber. 35
4	This figure is a plot of specific heat of the material calculated using Eq. (2.76) for different values of θ_s 44
5	The theoretical predictions are represented by solid lines, while, the data obtained by George (1982), is denoted by points. The solid crosses represent the point of initiation of the mixture model. Here, d_o is the same as d_s . The average velocity at the maximum swell section, v_e , is used to non-dimensionalize velocity. 49
6	The temperature profiles for three different take-up speeds. 50
7	The figure shows the variation of diameter of the drawn fiber along the spin-line. 51

FIGURE	Page
8	The figure shows the stress along the length of the fiber. After initiation, the predicted stress shows a ‘linear’ response with an increasing slope for increasing take-up speeds. 52
9	The figure represents the configurations associated with the melt. The point \mathbf{X} is the position occupied by the particle in the reference configuration. The point \mathbf{x} is the current position of the particle. 56
10	This figure represents the configurations associated with the mixture. The configuration associated with the solid at the instant of the initiation of the mixture model is denoted by κ_r 56
11	The data was obtained at a constant strain rate of $0.1s^{-1}$ at 150^0C for Linear Low Density Polyethylene (LLDPE). The initial cross sectional area, A_0 , is $17.19mm^2$ (see [40]). The material constants used are $\beta = 0.97$, $\bar{\mu}_1^m = 20000Pa$, $\left\{ \frac{\bar{\mu}_1^m}{(\nu_1^m)^\beta} \right\}^{1/(2\beta-1)} = 1.3717 s^{-1}$, and $\bar{\mu}_2^m = \nu_2^m = \nu_3^m = 0$ 71
12	The plot indicates the measured force at two different strain rates at 250^0C for polyamide. The material constants picked were $\beta = 0.95$, $\bar{\mu}_1^m = 18000Pa$, $\left\{ \frac{\bar{\mu}_1^m}{(\nu_1^m)^\beta} \right\}^{1/(2\beta-1)} = 7.4458 s^{-1}$, and $\bar{\mu}_2^m = \nu_2^m = \nu_3^m = 0$ 72
13	The plot shows the stress at constant strain rate for polystyrene at 170^0C . The material constants are $\beta = 0.8$, $\bar{\mu}_1^m = 400Pa$, $\bar{\mu}_2^m = 1400Pa$, $\left\{ \frac{\bar{\mu}_1^m}{(\nu_1^m)^\beta} \right\}^{1/(2\beta-1)} = 8.8039 \times 10^{-4} s^{-1}$, and $\frac{\nu_1^m}{\nu_2^m} = 4.375$ 72
14	The above figure shows the comparison of the predictions and the data during constant length relaxation of the sample. The initial conditions are $B(t_0) = 2.5465, 4.2075, \text{ and } 5.7865$; the value of $B(t_0)$ ’s obtained at the end of the constant strain rate experiment in the Fig. 13. The material constants are the same as that used to obtain Fig. 13. 73
15	The above figure shows the stress at constant strain after loading and unloading at $253K$ with $t_1 = 12s$. The material constants used in the simulation are $\mu_1^s = 22.77Mpa$, $\mu_2^s = 0.392Gpa$, and $\nu^s = 0.24GPas$. The initial conditions for $T_f = 50$ and $110Mpa$ are 0.9836 and 0.9636 respectively. The data for 170 and $230MPa$ is not shown. 86

FIGURE	Page
16	The figure represents the configurations associated with the melt. The point \mathbf{X} is the position occupied by the particle in the reference configuration. The point \mathbf{x} is the current position of the particle. 93
17	The figure represents the configurations associated with the mixture. 94
18	Legends for the Figs. (b) and (d) indicating appropriate predictions of the model are the same as that of Figs. (a) or (c). These figures show the effect of mass flow rate. 115
19	The effect of quench air speed. 118
20	Low speed spinning. 120
21	The effect of changing capillary diameter. 123
22	The effect of molecular weight. 125
23	Velocity, Filament diameter and crystallinity for different polymers. . 127
24	The effect of additives on homopolymer nylon 129
25	The plots associated with the mass flow rate of nylon 6 (BHS) at 5.069 g/min. 132
26	The plots associated with the mass flow rate of nylon 6 (BHS) at 2.993 g/min. 133
27	The velocity and stress plots associated with the mass flow rate of nylon 6 (BHS) at 5.069 g/min (the top two figures) and 2.993 g/min respectively. 134
28	The above figure represents the configurations associated with the solidifying mixture. 144

CHAPTER I

INTRODUCTION

- A. An introduction to structural development of polymers subjected to thermal and mechanical process

The International Union of Pure and Applied Chemistry (IUPAC) defines polymer (see Metanowski [41]) as *A substance composed of molecules characterized by the multiple repetition of one or more species of atoms or groups of atoms linked to each other in amounts sufficient to provide a set of properties that do vary markedly with the addition or removal of one or a few of the constitutional units.* A constitutional unit is defined as *A species of atom or group of atoms present in a chain of a polymer.*

Depending upon the polymer and the process that it is subjected to, it can exist in an amorphous or a semi-crystalline state. When a polymer melt is cooled sufficiently quickly, it forms an amorphous solid below a certain temperature termed as the glass transition temperature (see Tobolsky and Mark [80]). For most polymers, the transition to the glassy state (amorphous solid with no regular structure) happens over a temperature interval of a few degrees. Above the temperature at which transition starts towards the glassy state, the material has enough mobility to respond to the external conditions almost immediately. On the other hand, below this temperature at which the transition to the glassy state is complete, the intrinsic relaxation time scale involved is extremely large when compared to the experimental time scale. Experimental data of Onaran and Findley [46] suggests that the predominantly glassy polymers behave like a viscoelastic solid. Depending upon the material, there are many routes to the glassy state. The familiar way is by cooling the liquid sufficiently

The journal model is *IEEE Transactions on Automatic Control*.

'fast'. Another way to reach the glassy phase is through chemical reactions. A discussion of diverse routes to glassy phase can be found in Angell [2]. Here, we shall restrict ourselves to glass formation through cooling that is relevant in many polymer processes like fiber spinning and film blowing (see § 2).

The ability of the polymer to form a crystalline structure depends upon the structure of the molecules themselves. Isotactic and syndiotactic polymers (with regular structure) form crystalline solids as opposed to the atactic polymers (with no regular structure) which largely form amorphous solids. Poly ethylene terephthalate (PET) is largely an atactic polymer that often forms a glassy phase below $78^{\circ}C$. Of course, under slow cooling conditions and/or with sufficiently large deformation, even PET solidifies to a semi-crystalline state.

Some polymers like polyethylene, polypropylene, nylon 6, nylon 66 and so forth upon cooling, unlike glassy polymer such as PET, easily solidifies to a semi-crystalline state. The temperature at which the polymer melt begins to crystallize is called the crystallization temperature. Polymers do not have a single crystallization temperature and it depends on the process (thermal and mechanical) to which the polymer is subjected to. Under quiescent conditions (no deformation), under very slow cooling conditions, polymers tend to crystallize at what is called equilibrium crystallization temperature. However, in real processes, the crystallization is triggered at much lower temperature and deformation elevates the temperature at which crystallization is triggered. X-ray diffraction studies can be used to identify the type and the amount of crystals present in the semi-crystalline sample. In one of the studies by Piccarolo *et al.* [54], isotactic polypropylene samples were quenched from a melt-like state under quiescent conditions (no deformation). Cooling rates of the order of few hundred degrees per sec were achieved during the quenching process and differential scanning calorimetry (DSC) was used to achieve cooling rates of the order of a few degrees per minute. It was

observed that the higher the cooling rate, the lesser the amount of monoclinic crystals formed and the larger the amount of mesomorphic crystals (crystals without much order) with the total crystallinity (sum of monoclinic and mesomorphic crystals) decreasing with cooling rate. Thus, the type and the amount of crystals formed during solidification depends on the thermal history suffered by polypropylene. It is well known that the crystallization is enhanced by the deformation (flow-induced crystallization) because the stretching bring the polymer molecules close to each other, which facilitates the crystallization process (see Spruiell and White [75]). On the other hand, 'fast' cooling rates tend to suppress the crystallization process and if the cooling rate is fast enough the polymer may become a glass by totally bypassing the crystallization route. Thus there is a competition between the cooling rate and the extend to which a polymer is deformed. Consider a thermal process in which the polymer melt solidified into a semicrystalline state under 'slow' cooling conditions of the order of a few hundred seconds. There is enough time for the crystals that had formed at some previous time τ (with t being the current time) to grow and perfect itself for a period of $t - \tau$ and this mechanism of crystallization is termed as secondary crystallization. Such a mechanism is not important for much faster processes such as fiber spinning. Differential scanning calorimetry is used to characterize the specific heat capacity and latent energy of the materials. Even in the semicrystalline state, when the polymer is cooled below a certain temperature, the specific heat capacity of the semicrystalline polymer shows a sharp decrease just like the differential scanning thermogram of largely glassy materials such as PET (see Gaur *et al.* [20]). The crystalline phase of the semicrystalline solid does not show any change themselves and hence the entire decrease in the specific heat capacity of the polymer is attributed to the liquid-like amorphous portion in the semi-crystalline polymer converting to a glassy solid (see the 4th objective in §5).

B. Typical industrial processes

In many of the industrial processes, the polymer is deformed and cooled from a melt-like state and solidified either to a glassy or a semi-crystalline state depending on the application. Some typical industrial processes are:

1. Fiber spinning

Fiber spinning involves the following processes. The polymer melt exits the die at about 300°C , and as the melt exits, it swells to a certain diameter (see figure on page 35) denoted by d_s . Further along the spin line, the melt is continuously drawn. Cross flow air cools the melt. When the melt reaches a certain temperature (the glass transition or crystallization temperature), the fiber diameter almost becomes a constant. The solidified fiber is wound at a certain speed, which is called the take-up speed. In such a high speed spinning process (take-up speed of ~ 6000 m/min), the effect of air drag on the lateral surface of the fiber and inertia is usually included.

2. Other processes

Film blowing is a process in which sheets of plastics can be produced. In blow molding, the polymer melt is blown to take the shape of the die and is cooled to produce the solidified product (e.g. plastic bottles). In injection molding, the melt is injected into the die under high pressure so that the melt can flow into all the crevices in the die cavity.

C. Need for modeling

1. Design of a process

By controlling the processing conditions such as the cooling rate, rate of deformation and so forth, one can obtain desired mechanical properties of the final solid because the amount and orientation of the crystals formed directly influence the mechanical properties. Thus, by solving the relevant initial-boundary value problems, one can design the process, without resorting to experiments that are expensive and time consuming, to achieve desired mechanical properties in the semicrystalline solid.

2. Design of die set

Dies are very expensive and design through experiments alone can be prohibitively expensive and time consuming. Therefore, one needs to develop a model that can describe the response of a class of polymer of interest. The die cavity has to be designed such that, subject to the functionality requirements of the product in question, desired mechanical properties are achieved. To this end, the relevant initial-boundary problem is solved repeatedly (using an appropriate model) by altering the cavity geometry so that desired mechanical properties are achieved; an optimization problem. Of course, one cannot entirely eliminate the need for experiments. However, much simpler and fewer experiments could be used to characterize the material.

D. Natural configurations

Many bodies can exist in more than one stress-free configuration. As the material is subjected to a thermomechanical process, the body would attain an intermediate configuration when the external stimuli in the current configuration are removed. Such a configuration is termed as a natural configuration and it evolves during a

thermomechanical process. In this way, we have a family of thermomechanical response from an evolving set of natural configurations (stress-free configurations). The microstructure associated with the evolving natural configuration may be different and hence the material symmetry with respect to these configurations may change. In this way, this framework allows us to incorporate the evolution of symmetry of the body.

In the case of solidification of molten polymers, there are an infinity of natural configurations associated with the melt, related to the breaking and reforming of polymer network, and the solid formed during the process. The melt and the amorphous solid is assumed to be isotropic with respect to each of the natural configurations and the crystalline solid formed at each instant is anisotropic reflecting the crystalline microstructure. For a detailed discussion, the reader is referred to Rajagopal and Srinivasa [63] and [64].

E. Earlier approaches

Many of the earlier attempts to describe the solidification of the polymer melt have been to describe fiber spinning. Most of the synthetic fibers, such as PET, nylon 6, nylon 66, polyethylene, kevlar and so forth are produced by melt spinning, which have a plethora of uses, for example, in textile and structural applications. It accounts for about 15% of the GDP of manufacturing segment (~ 160 Billion dollars). Thus there is a lot of interest in describing solidification of polymer melts. It is also relatively easy to obtain on line experimental data on the velocity, surface temperature of the fiber and degree of crystallinity estimated from X-ray diffraction patterns besides the type of crystals formed. Thus, a plenty of experimental data is available for comparison with the predictions of the theory.

1. Attempts based on describing the solidification of a polymer to a glassy state

Kase and Matsuo (1967) treated the polymer melt as a Newtonian fluid and neglected air drag and inertia. Fisher and Denn [18] modeled the melt as a Maxwell liquid and included heat transfer effects. Later, Gagon and Denn [19] used the Phan-Thien Tanner constitutive equation to model the melt including the effects of air drag, gravity, inertia, and heat transfer. These simulations are terminated at glass transition temperature and an ad hoc constant velocity is prescribed for the solidified region signifying the constant velocity plateau observed in experiments. George [21], modeled the melt as a Newtonian fluid. By choosing an exponential form for the elongational viscosity of the melt and letting it to go to a large value, he was able to capture the plateau in the fiber spinning curves. However, such an effort leads only to a highly viscous Newtonian fluid; transition to a largely energetic solid phase is not achieved. The non-isothermal spinning process compares reasonably well with the experiments. Recently, Ottone and Deiber [47] modeled the melt spinning of PET as having both the characteristic of PTT and a Newtonian fluid. The calculations compares well with the data, but, once again, the transition to a solid is not considered. Further, the model is very specific and lacks a general thermodynamic basis and none of the models discussed above have a general thermodynamic basis and the transition to a solid phase is never considered.

2. Attempts based on describing the solidification of a polymer to a semicrystalline solid

Patel *et al.* [49] used a Newtonian model to fit the fiber spinning data of nylon 6 (solidifies into a semicrystalline solid) obtained by Bheda and Spruiell [4]. To capture the plateau in velocity after significant crystallization, the viscosity was allowed to

increase to a large value. While this method is a good early attempt to model the problem, one does not obtain a solid in the semi-crystalline region and it is difficult to capture the plateau (e.g. Zieminski and Spruiell [89]). Sun *et al.* [77] used a viscoelastic liquid to simulate the problem (a modified PTT model) with the viscosity depending on temperature and crystallinity (2-D simulations) for the semicrystalline regime. Only a part of the data of Bheda and Spruiell [4] was used as the focus was on low-speed simulations. Doufas *et al.* [14] and [15], using the conformation tensor approach, modeled the melt as a viscoelastic liquid (Giesekus fluid) and the semicrystalline phase as a collection of rigid rods that grow, at the expense of the melt, and orient during deformation. Equilibrium melting temperature was used as an initiation criterion for crystallization. The model predictions agree very well with the experimental data, but the effect of thermal history is not accounted for.

Rao and Rajagopal [73] put into place a general thermodynamic framework to describe polymer crystallization. The melt was modeled as a viscoelastic liquid and the semi crystalline solid was modeled as a mixture of elastic solids that are formed continuously over a period of time and the original viscoelastic liquid. The material symmetry of the solid that is formed ('average' orientation of the crystals) at any particular instant, modeled as an orthotropic elastic solid, depends on deformation that the melt has suffered. Thus, the response of the final semicrystalline material depends on the process to which the melt was subjected during the course of crystallization. The initiation of crystallization would depend on the temperature and deformation, the crystallization kinetics, the form of the stress, and so forth are obtained in a systematic manner from thermodynamic considerations. It should be mentioned that the evolving material symmetry is obtained as a part of the solution to the problem of interest. Experiments performed on the polymer in the solid-like state (both glassy and semicrystalline polymers) indicates that it behaves like a viscoelastic solid (see

Onaran and Findley [46]). The models obtained using this framework can explain the stress relaxation of semicrystalline polymer because the amorphous part of the semicrystalline mixture can stress relax. However, unlike crystallization, certain polymer in liquid-like state solidify into a glassy solid (without detectable crystallinity) and it is usually assumed that the entire polymer melt solidifies into a solid. Since a glassy solid behaves like a viscoelastic solid (see Onaran and Findley [46]), one needs a thermodynamical framework that can describe such a transition. Kannan *et al.* [32] used the framework of Rao and Rajagopal [73] to develop a model for glass transition phenomenon by approximating the glassy solid as an elastic solid. Since fiber spinning is a 'fast' process, i.e., a typical processing time of about 20 milliseconds, polymer in the glassy state will have very little time to stress relax and hence, for such processes, modeling the glassy phase as an elastic solid is a good approximation. However, if one wants to develop a model with a wider scope of applicability, i.e., for processes that are slower than fiber spinning such as blow molding, which has a typical cycle time of about 10 seconds, then it would be appropriate to model the glassy state as a viscoelastic solid (see objective 2 in §5).

F. Objectives and proposed methodology

1. Use an existing thermodynamical framework of Rao and Rajagopal (2002) that takes into account the existence of more than one stress-free configuration (natural configurations) to develop a model for glass transition phenomenon by treating the glassy solid as an elastic material. Develop a model and compare the predictions of the model with the fiber spinning data of PET, which is largely forms a glassy solid under 'low' speed spinning conditions.
2. Develop a thermodynamical framework, generalizing the framework of Rao and

Rajagopal [73], that takes into account the evolution of stress free configurations (natural configurations) to model the transition of a viscoelastic liquid to a viscoelastic solid by defining various primitives, i.e., Helmholtz potential and rate of entropy production due to dissipation in the melt and the solid, conduction and phase change, and arrive at a model that is suited for modeling glass transition process (treating the glassy solid as a viscoelastic solid) and compare the predictions of the model in the melt-like and solid-like phase.

3. Using a simplified version of the above framework, i.e., the framework developed for the transition of a viscoelastic liquid to an elastic solid, develop a model for flow induced crystallization with flow induced anisotropy. Compare the predictions of the model with the experimental data available for high speed fiber spinning including the effects due melt viscoelasticity, drag on the fiber, gravity, inertia effects, the cooling of the fiber, the initiation of crystallization (that depends on both the temperature and deformation), flow induced crystallization and the anisotropy of the crystalline phase of the semicrystalline solid.
4. Develop a thermodynamical framework that take into effect the thermal history of the polymer melt, flow-induced crystallization of an amorphous melt (with evolution of symmetry) to a semicrystalline state including the effect due secondary crystallization and transition of amorphous liquid-like polymer in the semicrystalline solid to a glassy solid below the glass transition.

CHAPTER II

A THERMOMECHANICAL FRAMEWORK FOR THE GLASS TRANSITION
PHENOMENON IN CERTAIN POLYMERS AND ITS APPLICATION TO
FIBER SPINNING*

A thermodynamic framework is developed to describe a polymer melt undergoing glass transition that takes into account the fact that during such a process the underlying natural configurations (stress-free states) are continually evolving. Such a framework allows one to take into account changes in the symmetry of the material, if such changes take place. Moreover, the framework allows for a seamless transition of a polymeric melt to a mixture of a melt and an elastic solid to the final purely solid state. The efficacy of the model is tested by studying the fiber spinning problem for polyethylene terephthalate and the predictions agree well with the experimental results.

A. Introduction

Depending upon the polymer and the process that the polymer is subjected to, it can exist in an amorphous or a semi-crystalline state. When a polymer melt is cooled sufficiently quickly, it forms an amorphous solid below a certain temperature termed as the glass transition temperature (see Tobolsky and Mark [80]). For most polymers, the transition to the glassy state happens over a temperature interval of a few degrees. Above the temperature at which transition starts towards the glassy state,

*Reprinted with permission from “A THERMOMECHANICAL FRAMEWORK FOR THE GLASS TRANSITION PHENOMENON IN CERTAIN POLYMERS AND ITS APPLICATION TO FIBER SPINNING” by K. KANNAN and K.R. RAJAGOPAL, 2002. *J. RHEOL.*, VOL. 46, PP. 977-999. 2002 by THE SOCIETY OF RHEOLOGY, INC.

the material has enough mobility to respond to the external conditions almost immediately. On the other hand, below this temperature at which the transition to the glassy state is complete, the intrinsic relaxation time scale involved is extremely large when compared to the experimental time scale. As a result, the material appears to be in a solid state. The ability of the polymer to form a crystalline structure depends upon the structure of the molecules themselves. Isotactic and syndiotactic polymers (with regular structure) form crystalline solids as opposed to the atactic polymers which form amorphous solids. Poly ethylene terephthalate (PET) is largely an atactic polymer that often forms a glassy phase below $78^{\circ}C$. Here we develop a theoretical framework for the transition of a polymer from a melt to an amorphous solid.

Depending upon the material, there are many routes to the glassy state. The familiar way is by cooling the liquid sufficiently 'fast'. Another way to reach the glassy phase is through chemical reactions. A discussion of the diverse routes to the glassy phase can be found in Angell [2]. Here, we shall restrict ourselves to glass formation due to cooling that is relevant in many polymer processes like fiber spinning and film blowing.

When materials such as PET are deformed, sufficiently above the glass transition temperature, in the melt-like state, the change in the elastic part of the internal energy is negligible; most of the work done on the material is dissipated into heat (energy in thermal form). Therefore, we shall assume that the internal energy of the polymer melt to be a function of temperature alone. On the other hand, at a given temperature, the entropy of the material diminishes as the molecules are stretched during deformation, and it usually increases with increase in temperature. When the load is released, the material tends to go to a state of maximum entropy (Mark and Erman [36]) that corresponds to a random configuration of polymer chains that is

usually stress free. Such materials are primarily entropic in nature. From a molecular perspective, as the melt is deformed, the inter-molecular junctions are formed and broken. At any stress-free state, the long chain molecules are randomly arranged. As a result, from the morphology of the melt, it is reasonable to assume that the melt is isotropic with respect to the current stress-free state (natural configuration).

Contrary to the behavior of the melt, sufficiently below the glass transition temperature, as the material is being deformed, the change in entropy of the glassy solid is insignificant (for typical processes like fiber spinning, film blowing and so forth). However, the change in internal energy due to deformation can be significant. Since the solid is formed in an amorphous state, it may be reasonable to assume that the solid that is formed is isotropic. While this assumption is true for materials such as PET, it is not the case for other polymeric materials that are Isotactic or Syndiotactic.

Usually, the transition from liquid-like to a solid-like phase occurs over a $5 - 10^\circ\text{C}$ range. In our study, this transitional region is modeled as a mixture of two phases; both the phases, in this regime are constrained to move together.

The material response over the entire range is described with the help of a unified model that captures the entropic response in the melt-like regime, a mixture of energetic and entropic response in the transition region (typically a few degrees), and finally a solid-like response beyond the transitional interval. We need an initiation criterion that signals the material, from that of a melt to that of a solid, and we shall show later that this criterion arises naturally from thermodynamic considerations.

We develop a phenomenological model based on the fact that the polymer has different natural configurations (stress-free configurations modulo rigid motions) associated with the melt like state and the solid state. Natural configurations associated with the transitional state are determined by knowing the natural configurations of the

melt and the solid. In fact the polymer in its fluid-like and transitional state has an infinity of natural configurations (see Rao and Rajagopal [71] and [72], Rajagopal and Srinivasa [66]). The effectiveness of the model is tested by solving the problem of fiber spinning of PET. At take-up speeds in excess of about 5000 m/min, significant crystallization of PET is possible (see Denn [11]). Also, significant deformation of the fiber in its solid state is also possible. A general theory that can take into account such eventualities has already been put into place and it also allows for a variety of generalization of the theory presented here. The interested reader is referred to Rao and Rajagopal [72] for the details of the general theory.

As the polymer transforms from its state as a melt, through the transitional regime to its final glassy state, the underlying natural configurations evolve, and its response can be described by specifying a class of response functions from these natural configurations. Eckart [17] recognized that many bodies can exist in more than one natural configuration (stress-free state) and developed the kinematics for such bodies. Rajagopal and his co-workers have developed a thermodynamic framework for the bodies that possess multiple natural configurations that takes cognizance of the fact that the symmetry associated with different natural configurations could be different. They have demonstrated the efficacy of such a framework by describing successfully a diverse class of problems: response of multi-network polymers (Rajagopal and Wine-
man [69], Wineman and Rajagopal [85]), twinning (Rajagopal and Srinivasa [61] and [62]), traditional plastic response (Rajagopal and Srinivasa [63] and [64]), solid to solid phase transition (Rajagopal and Srinivasa [65]), viscoelastic response (Rajagopal and Srinivasa [66], Murali krishnan and Rajagopal [42]), anisotropic response of liquids (Rajagopal and Srinivasa [67]), crystallization of polymers (Rao and Rajagopal [73], [71] and [72]), superplastic response (Rajagopal and Chandra [60]), growth and adaptation of biological materials (Humphrey and Rajagopal [30], Rao *et al.* [70]). The

study most relevant to the problem investigated here is that carried out by Rao and Rajagopal [73] to describe the crystallization of polymer melts. However, all the above mentioned studies share in common a general thermodynamic framework.

Here, we use a general thermodynamic framework for materials with multiple natural configurations to study the problem of fiber spinning in polymers such as PET that are amorphous below the glass transition temperature. We begin by proposing a form for the rate of entropy production (times temperature) associated with mechanical working and the Helmholtz potential, defined with respect to these evolving natural configurations. The rate of entropy production associated with mechanical working is chosen such that it automatically satisfies the requirement of non-negativity. As a consequence, using the second law, one can arrive at the functional form for the stress tensor, entropy, and the internal energy measured with respect to these evolving configurations. In addition to specifying these class of response functions, we need an initiation (activation) criterion that determines whether the natural configuration will change or stay the same, and an evolution equation that determines how the natural configurations change. In the case of crystallization and growth, we need to also provide the growth kinetics, i.e., the rate of production of new material or the rate of conversion. For example, in polymer crystallization, the Avrami equation is one such example. A central assumption that is used in our study is the following: amongst all the constitutive relations that are candidates for modeling the process, the one that is picked is that which maximizes the rate of entropy production. The framework provides a clear way to associate the manner in which energy is stored or dissipated, the manner in which entropy is produced, etc.

Previous attempts at solving the fiber spinning problem, where crystallization is minimal and the glass transition is the dominant phenomena, do not consider the transition to a solid and the further deformation of the solid. These investigators

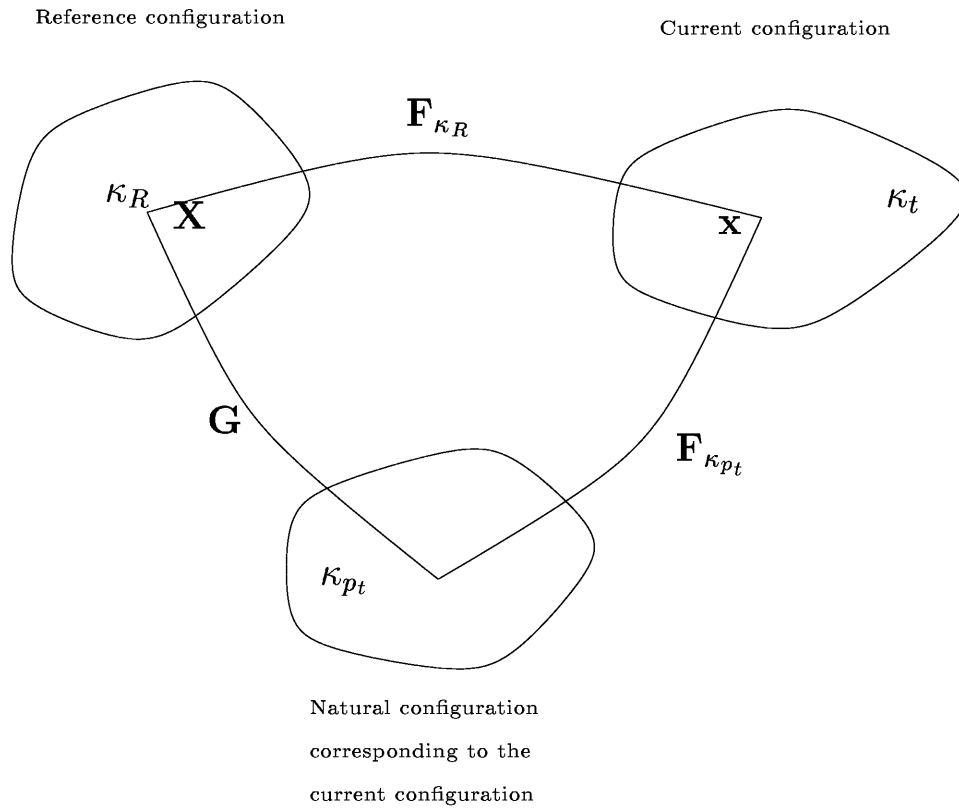


Fig. 1. The figure represents the configurations associated with the amorphous melt. \mathbf{X} is the position occupied by the particle in the reference configuration, κ_R . \mathbf{x} is the current position of the particle.

(Fisher and Denn [18], Gagon and Denn [19], Kase and Matsuo [33], Ottone and Deiber [47]), terminate their simulations at the glass transition temperature; however, we should recognize that some of these studies were carried out over two decades ago and were important contributions to the field at their time. Below the glass transition temperature, the velocity of the spun fiber is taken to be the velocity corresponding to the glass transition temperature. George [21], in his simulation, assumed a transition to a highly viscous Newtonian liquid that captured the plateau observed in the velocity profiles below the transition temperature. Such an approach does have a snag as it only leads to a liquid model with high viscosity and not to a solid model. Some authors (Doufas and McHugh [13]) model the solidification of molten PET as a continuous flow induced crystallization, but with a small final crystallinity as observed in experiments. Their velocity and temperature profiles agree well with the experiments, as do our results. Our approach is based on the phase change (liquid-like to elastic solid) that happens over a narrow range of temperatures. The predictions of our theory also seems to agree well with the experimental results for the velocities as well as the temperature.

B. Kinematics

Let $\kappa_R(B)$ and $\kappa_t(B)$ denote (see Fig. 1) the reference and the current configuration of the body B . We shall, for the sake of convenience, suppress B in the notation $\kappa_R(B)$, etc. By the motion of a body we mean a one to one mapping that assigns to each point $\mathbf{X} \in \kappa_R$, a point $\mathbf{x} \in \kappa_t$, for each t , i.e.,

$$\mathbf{x} = \chi_{\kappa_R}(\mathbf{X}, t). \quad (2.1)$$

We shall assume that the motion is sufficiently smooth to render all the following operations meaningful.

The deformation gradient, \mathbf{F}_{κ_R} , and the left and right Cauchy-Green stretch tensors \mathbf{B}_{κ_R} and \mathbf{C}_{κ_R} are defined through

$$\mathbf{F}_{\kappa_R} = \frac{\partial \chi_{\kappa_R}}{\partial \mathbf{X}}, \quad \mathbf{B}_{\kappa_R} = \mathbf{F}_{\kappa_R} \mathbf{F}_{\kappa_R}^T, \quad \text{and} \quad \mathbf{C}_{\kappa_R} = \mathbf{F}_{\kappa_R}^T \mathbf{F}_{\kappa_R}. \quad (2.2)$$

Let $\kappa_{p(t)}$ be the stress-free state (natural configuration) associated with the current configuration κ_t of the body. For homogeneous deformations $\mathbf{F}_{\kappa_{p(t)}}$ denotes the deformation gradient between these two configurations. In general $\mathbf{F}_{\kappa_{p(t)}}$ may not be the gradient of a mapping (see Rajagopal and Srinivasa [63]).

The mapping \mathbf{G} (see Fig. 1) is defined through

$$\mathbf{G} = \mathbf{F}_{\kappa_R \rightarrow \kappa_{p(t)}} = \mathbf{F}_{\kappa_{p(t)}}^{-1} \mathbf{F}_{\kappa_R}. \quad (2.3)$$

In a manner similar to that used in Eq. (2.2), the left Cauchy-Green stretch tensor associated with the instantaneous response from the natural configuration $\kappa_{p(t)}$ is defined as

$$\mathbf{B}_{\kappa_{p(t)}} = \mathbf{F}_{\kappa_{p(t)}} \mathbf{F}_{\kappa_{p(t)}}^T. \quad (2.4)$$

We introduce the principal invariants of $\mathbf{B}_{\kappa_{p(t)}}$ through

$$I_{\kappa_{p(t)}} = \text{tr}(\mathbf{B}_{\kappa_{p(t)}}), \quad II_{\kappa_{p(t)}} = \frac{1}{2} \left\{ [\text{tr}(\mathbf{B}_{\kappa_{p(t)})}]^2 - \text{tr}(\mathbf{B}_{\kappa_{p(t)}}^2) \right\}, \quad \text{and}, \quad III_{\kappa_{p(t)}} = \det(\mathbf{B}_{\kappa_{p(t)}}). \quad (2.5)$$

The velocity gradients, \mathbf{L} and $\mathbf{L}_{\kappa_{p(t)}}$, are defined through

$$\mathbf{L} = \dot{\mathbf{F}}_{\kappa_R} \mathbf{F}_{\kappa_R}^{-1} \quad \text{and} \quad \mathbf{L}_{\kappa_{p(t)}} = \dot{\mathbf{G}} \mathbf{G}^{-1}, \quad (2.6)$$

where the dot signifies the usual material time derivative. The notation in Eq. (2.6)₂ is somewhat inconsistent with the rest of the notation that has been introduced, but

we shall use it nonetheless in view of its prior use in the literature.

The symmetric parts of \mathbf{L} and $\mathbf{L}_{\kappa_p(t)}$ are given respectively, by the following two equations:

$$\mathbf{D} = \frac{1}{2}(\mathbf{L} + \mathbf{L}^T), \text{ and } \mathbf{D}_{\kappa_p(t)} = \frac{1}{2}(\mathbf{L}_{\kappa_p(t)} + \mathbf{L}_{\kappa_p(t)}^T). \quad (2.7)$$

The upper convected Oldroyd derivative of $\mathbf{B}_{\kappa_p(t)}$, $\overset{\nabla}{\mathbf{B}}_{\kappa_p(t)}$, is given through

$$\overset{\nabla}{\mathbf{B}}_{\kappa_p(t)} = \dot{\mathbf{B}}_{\kappa_p(t)} - \mathbf{L}\mathbf{B}_{\kappa_p(t)} - \mathbf{B}_{\kappa_p(t)}\mathbf{L}^T = -2\mathbf{F}_{\kappa_p(t)}\mathbf{D}_{\kappa_p(t)}\mathbf{F}_{\kappa_p(t)}^T. \quad (2.8)$$

As we shall require the material, both in molten state as well as in its glassy state to be incompressible, we shall require that

$$\det(\mathbf{B}_{\kappa_p(t)}) = 1 \text{ (or } \text{tr}(\mathbf{L}_{\kappa_p(t)}) = 0) \text{ and } \text{tr}(\mathbf{L}) = 0. \quad (2.9)$$

We also introduce the natural configuration κ_r associated with the amorphous solid that is being formed. It is important to recognize that κ_r is not the same as κ_R and a few comments about the configuration κ_r from which the kinematical measurements for the solid in the glassy state are measured are in order. The solid is assumed to be born in a stress-free state, and the configuration in which the solid is formed (κ_r) is the reference configuration of the solid. Thus, as the glass transition proceeds, more and more of the solid is born in different natural configurations.

C. Restrictions imposed on constitutive equations

1. The second law of thermodynamics

The usual practice is to use the dissipation inequality to place restrictions on the constitutive equations and the constitutive equations obtained are both necessary and sufficient as the arbitrariness of the processes are invoked. Dissipation inequality is obtained by proposing an inequality for the entropy (relating the total specific en-

tropy and the entropy supplies, i.e., Clausius-Duhem inequality) and by eliminating the radiation term between the energy balance and the Clausius-Duhem inequality. There are some drawbacks to using the dissipation inequality when applied to some problems involving thermal heating by radiation as one needs to specify a constitutive equation for radiant heating term. The dissipation inequality places no restrictions on the radiant heating term directly although the Clausius-Duhem inequality places restrictions. Second, the constitutive equations holds only for certain processes and hence arbitrariness of processes cannot be invoked to begin with. For a detailed discussion of these issues refer to Rajagopal and Tao [68].

In this dissertation, the second law of thermodynamics introduced by Green and Naghdi [25] is used to place restrictions on the constitutive equations. The mathematical form of the second law is derived by positing an entropy equation relating the rate of entropy supplies, total rate of specific entropy and the rate of entropy production and by eliminating the radiant heating, as before, between the energy balance and the entropy equation. A Legendre transformation is introduced to arrive at the final form of the dissipation equation. For all the problems discussed in this dissertation, the radiant energy exchange between the system and the surrounding is neglected and hence this form of the second law of thermodynamics is used. The constitutive equations obtained are only sufficient conditions to satisfy the second law of thermodynamics, i.e., arbitrariness of processes are not invoked. A similar form of the second law of thermodynamics, under isothermal conditions, is used by Rajagopal and Srinivasa [66] to obtain restrictions on constitutive equations.

2. Material frame indifference

A change of frame is an one-to-one and an onto map between two space-times $\mathbf{X} \times \mathbb{R}$ and $\mathbf{X}^* \times \mathbb{R}^*$ such that the distance between any two points, time intervals and the

sense of time is preserved, i.e., the ordered pairs $\{\mathbf{x}, t\}$ and $\{\mathbf{x}^*, t^*\}$, where the ordered pairs are members of the unstarred and starred space-time, respectively, are related by

$$\mathbf{x}^* = \mathbf{c}(t) + \mathbf{Q}(t)(\mathbf{x} - \mathbf{x}_o), \quad t^* = t - a, \quad (2.10)$$

where a is a constant.

A scalar, vector and a tensor is said to be frame-indifferent if under a change of frame they are related through:

$$\phi^* = \phi, \quad \mathbf{v}^* = \mathbf{Q}\mathbf{v}, \quad \text{and} \quad \mathbf{T}^* = \mathbf{Q}\mathbf{T}\mathbf{Q}^T. \quad (2.11)$$

It follows from Eq. (2.10) and the definition of deformation gradient that

$$\mathbf{F}_{\kappa_R}^* = \mathbf{Q}\mathbf{F}_{\kappa_R}. \quad (2.12)$$

As there is an underlying evolving natural configuration associated with the breaking and reforming of the polymer network (for a detailed discussion see Wine-
man and Rajagopal [85], Rajagopal and Wineman [69], Rajagopal and Srinivasa [63] and [64]), an intermediate configuration or the natural configuration should be introduced as the Cauchy stress is represented with respect to the stress-free natural configuration. Accordingly the following multiplicative decomposition is introduced,

$$\mathbf{F}_{\kappa_R} = \mathbf{F}_{\kappa_p(t)} \mathbf{G} \quad (2.13)$$

Using the Eqs. (2.12) and (2.13) and if we suppose that $\mathbf{F}_{\kappa_p(t)}^* = \mathbf{Q}\mathbf{F}_{\kappa_p(t)}$, then $\mathbf{G}^* = \mathbf{G}$. The various primitives such as the specific Helmholtz potential, rate of dissipation and the various rate of entropy productions should be frame invariant. In

particular,

$$\begin{aligned}
\Psi(\mathbf{F}_{\kappa_p(t)}^*, \mathbf{G}^*, \theta^*) &= \Psi(\mathbf{F}_{\kappa_p(t)}, \mathbf{G}, \theta) = \Psi(\mathbf{Q}\mathbf{F}_{\kappa_p(t)}, \mathbf{G}, \theta) = \Psi(\mathbf{Q}\mathbf{R}_{\kappa_p(t)} \mathbf{U}_{\kappa_p(t)}, \mathbf{G}, \theta) \\
\xi(\mathbf{F}_{\kappa_p(t)}^*, \mathbf{G}^*, \mathbf{L}_{\kappa_p(t)}^*, \mathbf{L}^*, \theta) &= \xi(\mathbf{Q}\mathbf{F}_{\kappa_p(t)}, \mathbf{G}, \mathbf{L}_{\kappa_p(t)}, \boldsymbol{\Omega} + \mathbf{Q}\mathbf{L}\mathbf{Q}^T, \theta) \\
&= \xi(\mathbf{F}_{\kappa_p(t)}, \mathbf{G}, \mathbf{L}_{\kappa_p(t)}, \mathbf{L}, \theta) \\
\Rightarrow \hat{\Psi}(\mathbf{C}_{\kappa_p(t)}, \mathbf{G}, \theta) &\text{ and } \hat{\xi}(\mathbf{C}_{\kappa_p(t)}, \mathbf{G}, \mathbf{L}_{\kappa_p(t)}, \text{tr}\mathbf{D}, \text{tr}\mathbf{D}^2, \text{tr}\mathbf{D}^3, \theta), \tag{2.14}
\end{aligned}$$

where $\boldsymbol{\Omega}$ is an arbitrary skew symmetric tensor. The last result of the above equation is obtained by picking $\mathbf{Q} = \mathbf{R}_{\kappa_p(t)}^T$ and $\boldsymbol{\Omega} = -\mathbf{R}_{\kappa_p(t)}^T \mathbf{W}\mathbf{R}_{\kappa_p(t)}$, where $\mathbf{W} = \text{skw}(\mathbf{L})$ and using the fact that the eigen values of \mathbf{D} is the same as that of $\mathbf{R}_{\kappa_p(t)}^T \mathbf{D}\mathbf{R}_{\kappa_p(t)}$.

For the issue regarding the use of the less restrictive Galilean invariance, refer to Rajagopal and Tao [68] and Rajagopal [59].

D. Material symmetry

In the reference configuration κ_R , the material point \mathbf{X}_{κ_R} is subjected to an orthogonal transformation and then subjected to a motion such that it occupies the same position \mathbf{x} as in Eq. (2.1) (see Atkin and Fox [3]), i.e.,

$$\mathbf{x} = \boldsymbol{\chi}_{\kappa_R}(\bar{\mathbf{X}}_{\kappa_R}, t), \tag{2.15}$$

where $\bar{\mathbf{X}}_{\kappa_R} = \mathbf{H}\mathbf{X}_{\kappa_R}$ and \mathbf{H} is a constant orthogonal tensor. It is easy to see that $\mathbf{F}_{\kappa_R} \mathbf{H}^T = \bar{\mathbf{F}}_{\kappa_R}$ and if we suppose that $\mathbf{F}_{\kappa_p(t)} \mathbf{H}_p^T(t) = \bar{\mathbf{F}}_{\kappa_p(t)}$, then $\bar{\mathbf{G}} = \mathbf{H}_p(t) \mathbf{G} \mathbf{H}^T$.

Based on the microstructure of the material, certain orthogonal transformations (members of the symmetry group) of the natural configurations would leave the mechanical response of the material unchanged when subjected to the same deformation

for each member of the symmetry group. Accordingly, we require

$$\begin{aligned}
\hat{\Psi}(\bar{\mathbf{C}}_{\kappa_p(t)}, \bar{\mathbf{G}}, \bar{\theta}) &= \hat{\Psi}(\mathbf{H}_p \mathbf{C}_{\kappa_p(t)} \mathbf{H}_p^T, \mathbf{H}_p \mathbf{G} \mathbf{H}_p^T, \theta) = \hat{\Psi}(\mathbf{C}_{\kappa_p(t)}, \mathbf{G}, \theta) \\
\hat{\xi}(\bar{\mathbf{C}}_{\kappa_p(t)}, \bar{\mathbf{G}}, \bar{\theta}, \bar{\mathbf{L}}_{\kappa_p(t)}, \text{tr} \bar{\mathbf{D}}, \text{tr} \bar{\mathbf{D}}^2, \text{tr} \bar{\mathbf{D}}^3, \bar{\theta}) &= \hat{\xi}(\mathbf{C}_{\kappa_p(t)}, \mathbf{G}, \mathbf{L}_{\kappa_p(t)}, \text{tr} \mathbf{D}, \text{tr} \mathbf{D}^2, \text{tr} \mathbf{D}^3, \theta) \\
&= \hat{\xi}(\mathbf{H}_p \mathbf{C}_{\kappa_p(t)} \mathbf{H}_p^T, \mathbf{H}_p \mathbf{G} \mathbf{H}_p^T, \mathbf{\Omega} + \mathbf{H}_p \mathbf{L}_{\kappa_p(t)} \mathbf{H}_p^T, \text{tr} \mathbf{D}, \text{tr} \mathbf{D}^2, \text{tr} \mathbf{D}^3, \theta). \tag{2.16}
\end{aligned}$$

For the isotropic case, dropping argument \mathbf{G} , using standard arguments $\hat{\Psi}(\mathbf{C}_{\kappa_p(t)}, \theta) = \bar{\Psi}(\text{tr}(\mathbf{C}_{\kappa_p(t)}), \text{tr}(\mathbf{C}_{\kappa_p(t)}^2), \text{tr}(\mathbf{C}_{\kappa_p(t)}^3), \theta)$ and $\hat{\xi}(\text{tr}(\mathbf{C}_{\kappa_p(t)}), \text{tr}(\mathbf{C}_{\kappa_p(t)}^2), \text{tr}(\mathbf{C}_{\kappa_p(t)}^3), \text{tr}(\mathbf{D}_{\kappa_p(t)}))$, $\text{tr}(\mathbf{D}_{\kappa_p(t)}^2), \text{tr}(\mathbf{D}_{\kappa_p(t)}^3), \text{tr} \mathbf{D}, \text{tr} \mathbf{D}^2, \text{tr} \mathbf{D}^3)$.

E. Incompressibility

Polymer in any state is approximated as being incompressible, i.e.,

$$\text{tr} \mathbf{L} = \text{tr} \mathbf{L}_{\kappa_p(t)} = 0. \tag{2.17}$$

F. Other restrictions

The balance of angular momentum, in the absence of body couples, leads to a symmetric Cauchy stress tensor, i.e., $\mathbf{T} = \mathbf{T}^T$. The stress that is derived from the specific Helmholtz potential should be symmetric. Further, one would not expect any dissipation when $\mathbf{D} = \mathbf{D}_{\kappa_p(t)} = \mathbf{0}$.

G. Modeling the melt

In view of the discussion in the introduction, the Helmholtz potential per unit mass of the melt, Ψ_a , is assumed to be a function of absolute temperature, θ , and $\mathbf{B}_{\kappa_p(t)}$. As the amorphous melt is assumed to be isotropic, we shall choose the following form

for Ψ_a :

$$\Psi_a = C_a(\theta - \theta_a - \theta \ln \frac{\theta}{\theta_a}) + \frac{\mu_a(\theta_a)\theta}{2\rho\theta_a}(I_{\kappa_p(t)} - 3), \quad (2.18)$$

where θ_a is the reference temperature, C_a , μ_a are material constants, and the density ρ , is assumed to be a constant. Notice that this implies that the elastic response in an isothermal process, from the evolving natural configurations, is that for a neo-Hookean solid.

The rate of entropy production (times temperature) due to mechanical working, per unit volume of the amorphous melt, is assumed to have the following form

$$\xi_a(\theta, \mathbf{B}_{\kappa_p(t)}, \mathbf{D}, \mathbf{D}_{\kappa_p(t)}) = 2\nu^a(\theta, \mathbf{B}_{\kappa_p(t)})\mathbf{D}_{\kappa_p(t)} \cdot \mathbf{B}_{\kappa_p(t)}\mathbf{D}_{\kappa_p(t)} + 2\nu_1^a(\theta, \mathbf{B}_{\kappa_p(t)})\mathbf{D} \cdot \mathbf{D}, \quad (2.19)$$

where ν^a and ν_1^a are material functions, and ξ_a defined through Eq. (2.19) is non-negative. Moreover, the above form satisfies the requirement that if $\mathbf{D}_{\kappa_p(t)} = \mathbf{D} = \mathbf{0}$, then ξ_a is identically zero, i.e.,

$$\xi_a(\theta, \mathbf{B}_{\kappa_p(t)}, \mathbf{0}, \mathbf{0}) = 0. \quad (2.20)$$

We shall express the second law of thermodynamics in the form (see Green and Naghdi [25])

$$\mathbf{T}_a \cdot \mathbf{D} - \rho\dot{\Psi}_a - \rho\eta_a\dot{\theta} - \frac{\mathbf{q} \cdot \text{grad}(\theta)}{\theta} = \rho\theta\zeta_a = \hat{\xi}, \hat{\xi} \geq 0, \quad (2.21)$$

where ζ_a is rate of entropy production per unit mass of the melt.

The term $-\frac{\mathbf{q} \cdot \text{grad}(\theta)}{\theta^2}$ in Eq. (2.21) is the rate of entropy production due to conduction; it is a non-negative quantity which is positive when a temperature gradient exists and is zero when there is no temperature gradient. Furthermore, we shall assume $\hat{\xi}$ to be additive, i.e., we shall express

$$\hat{\xi} = \xi_c + \xi_a, \quad \xi_c, \xi_a \geq 0. \quad (2.22)$$

Here $\frac{\xi_c}{\theta}$ and $\frac{\xi_a}{\theta}$ are rate of entropy production per unit volume associated with conduction and mechanical working respectively. We shall further require each of the entropy production mechanisms to be non-negative.

Using Eq. (2.22) in Eq. (2.21), we arrive at the following two equations

$$\xi_c = -\frac{\mathbf{q} \cdot \text{grad}(\theta)}{\theta}, \text{ and } \mathbf{T}_a \cdot \mathbf{D} - \rho \dot{\Psi}_a - \rho \eta_a \dot{\theta} = \xi_a. \quad (2.23)$$

Substituting Eqs. (2.18) and (2.19) into Eq. (2.23) and collecting terms involving $\mathbf{D}_{\kappa_{p(t)}}$, and using Eq. (2.8) results in

$$\begin{aligned} & \left[\mathbf{T}_a - 2\rho \mathbf{B}_{\kappa_{p(t)}} \frac{\partial \Psi_a}{\partial I_{\kappa_{p(t)}}} - 2\nu_1^a \mathbf{D} \right] \cdot \mathbf{D} + \left[2\rho \mathbf{B}_{\kappa_{p(t)}} \frac{\partial \Psi_a}{\partial I_{\kappa_{p(t)}}} \right] \cdot \mathbf{D}_{\kappa_{p(t)}} \\ & - \rho \left[\frac{\partial \Psi_a}{\partial \theta} + \eta_a \right] \dot{\theta} = 2\nu^a \mathbf{D}_{\kappa_{p(t)}} \cdot \mathbf{B}_{\kappa_{p(t)}} \mathbf{D}_{\kappa_{p(t)}}. \end{aligned} \quad (2.24)$$

One way to satisfy the above equation is to assume that the following three equations hold

$$\mathbf{T}_a = -p\mathbf{I} + 2\rho \mathbf{B}_{\kappa_{p(t)}} \frac{\partial \Psi_a}{\partial I_{\kappa_{p(t)}}} + 2\nu_1^a \mathbf{D} = -p\mathbf{I} + \frac{\mu_a(\theta_a)\theta}{\theta_a} \mathbf{B}_{\kappa_{p(t)}} + 2\nu_1^a \mathbf{D}, \quad (2.25)$$

where p is a Lagrange multiplier that is a consequence of the constraint of incompressibility.

We also suppose that

$$\eta_a = -\frac{\partial \Psi_a}{\partial \theta} = C_a \ln \left(\frac{\theta}{\theta_a} \right) - \frac{\mu_a(\theta_a)}{2\rho\theta_a} (I_{\kappa_{p(t)}} - 3), \quad (2.26)$$

and

$$\begin{aligned} & \left[2\rho \mathbf{B}_{\kappa_p(t)} \frac{\partial \Psi_a}{\partial I_{\kappa_p(t)}} \right] \cdot \mathbf{D}_{\kappa_p(t)} = \frac{\mu_a(\theta_a)\theta}{\theta_a} \mathbf{B}_{\kappa_p(t)} \cdot \mathbf{D}_{\kappa_p(t)} \\ & = [\mathbf{T}_a - 2\nu_1^a \mathbf{D}] \cdot \mathbf{D}_{\kappa_p(t)} = 2\nu^a \mathbf{D}_{\kappa_p(t)} \cdot \mathbf{B}_{\kappa_p(t)} \mathbf{D}_{\kappa_p(t)}. \end{aligned} \quad (2.27)$$

The Helmholtz potential is defined in the terms of the internal energy, entropy, and temperature through

$$\Psi_a = \epsilon_a - \eta_a \theta, \quad (2.28)$$

where ϵ_a and η_a are the internal energy and the entropy per unit mass of the polymer melt, respectively. On using the definition for the Helmholtz potential Eq. (2.28), the internal energy of the melt is given by

$$\epsilon_a = C_a(\theta - \theta_a). \quad (2.29)$$

As the polymer melt is incompressible, we need to satisfy the constraints

$$\text{tr}(\mathbf{D}_{\kappa_p(t)}) = 0 \text{ and } \text{tr}(\mathbf{D}) = 0. \quad (2.30)$$

At this juncture, we do not know how the natural configurations evolve. Following Rajagopal and Srinivasa [66], we further assume that, for a fixed $\mathbf{B}_{\kappa_p(t)}$, θ , and \mathbf{D} , $\mathbf{D}_{\kappa_p(t)}$ should be such that it maximizes the rate of entropy production due to mechanical working and is given by Eq. (2.19). We could also keep $\mathbf{B}_{\kappa_p(t)}$ and θ fixed and vary \mathbf{D} and $\mathbf{D}_{\kappa_p(t)}$, they lead to the same results.

We maximize ξ_a , subject to Eqs. (2.27) and (2.30) as constraints (see Rao and Rajagopal [73])

$$\Phi = \xi_a + \hat{\lambda}_1 \left[2\nu^a \mathbf{D}_{\kappa_p(t)} \cdot \mathbf{B}_{\kappa_p(t)} \mathbf{D}_{\kappa_p(t)} - (\mathbf{T}_a - 2\nu_1^a \mathbf{D}) \cdot \mathbf{D}_{\kappa_p(t)} \right] + \hat{\lambda}_2 \text{tr}(\mathbf{D}_{\kappa_p(t)}), \quad (2.31)$$

where $\hat{\lambda}_1$ and $\hat{\lambda}_2$ are Lagrange multipliers due to the constraints (Eqs. (2.27) and (2.30)).

This leads to the evolution equation

$$\mathbf{B}_{\kappa_p(t)}^{\nabla} = \frac{\mu_a(\theta_a)\theta}{\theta_a\nu^a} \left[\frac{3}{\text{tr}(\mathbf{B}_{\kappa_p(t)}^{-1})} \mathbf{I} - \mathbf{B}_{\kappa_p(t)} \right]. \quad (2.32)$$

H. Modeling the mixture

Sufficiently below the glass transition temperature, the material behaves like a solid. The transitional stage is modeled as a mixture of a neo-Hookean solid and a model whose stress response is given by Eqs. (2.25) and (2.32). The solid phase is an amorphous state and hence expected to behave isotropically. Sufficiently below the glass transition temperature, the mixture exhibits a purely elastic response. The reference configuration of the solid is picked to be κ_r because the solid is assumed to be born in a stress-free state in the configuration $\kappa_{t=t_i}$, where t_i is the time at which activation criterion is satisfied.

Recalling that the solid behaves energetically, the Helmholtz potential of the solid per unit mass of the material is defined as

$$\Psi_s = C_s \left(\theta - \theta_s - \theta \ln \frac{\theta}{\theta_s} \right) + \frac{\mu_s}{2\rho} (I_{\kappa_r} - 3), \quad (2.33)$$

where μ_s is assumed to be a constant, θ_s , C_s , and I_{κ_r} are the reference temperature, specific heat capacity and trace of the left Cauchy-Green stretch tensor measured with respect to the reference configuration (see Fig. 2) κ_r of the solid respectively.

The DSC thermogram usually indicates a small transitional interval ($5 - 10^\circ C$) compared to the processing temperature range (typically a few hundred degrees). The temperature is assumed to control the transition from a liquid-like to a solid-like state. In order to incorporate this observation, the Helmholtz potential, per unit mass of

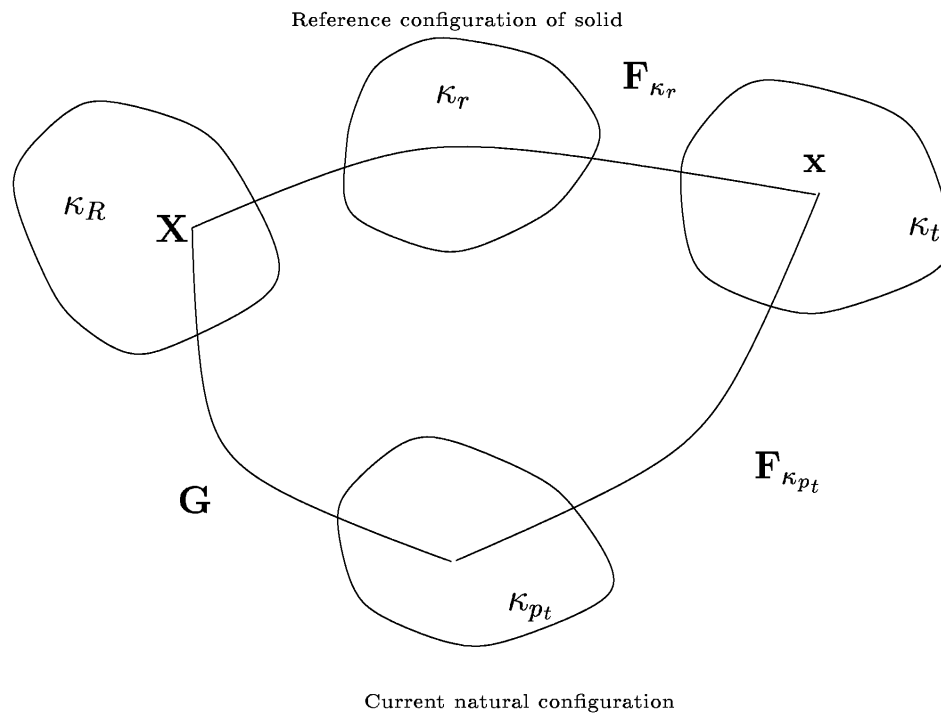


Fig. 2. This figure represents the configurations associated with the mixture. The configuration associated with the material at the instant of initiation, the glassy state, is denoted by κ_r . \mathbf{F}_{κ_r} maps the infinitesimal material fibers in κ_r to the corresponding material fibers in κ_t .

the material is defined as

$$\Psi = \frac{H(\theta - (\theta_g - \delta))}{1 + \exp(-s(\theta - \theta_g))} \Psi_a(\theta, I_{\kappa_p(t)}) + \frac{1}{1 + \exp(s(\theta - \theta_g))} \Psi_s(\theta, I_{\kappa_r}), \quad (2.34)$$

where s is a constant and θ_g is the glass transition temperature. The larger the value of the parameter s , the shorter is the interval for transition. The particular value for the material under consideration can be obtained by fitting the DSC data for a particular material. H is a Heavyside function and δ is a constant representing the 'half-width' of the transitional interval. Thus, for any temperature below $\theta_g - \delta$, $H(\theta - (\theta_g - \delta)) = 0$ and one recovers the Helmholtz potential for the solid. Notice that for $\theta_g + \delta \leq \theta < \theta_g - \delta$ the sum of the co-efficients multiplying Ψ_a and Ψ_s is unity. Physically, these co-efficients may be interpreted as representing the mass fraction of the melt and the solid respectively. For $\theta < \theta_g - \delta$ the fraction of the solid asymptotically approaches unity; the constant s is chosen in such a way that at $\theta = \theta_g - \delta$ the fraction of the solid is almost unity.

A single natural configuration is used for the solid that is formed continuously during the transition. Since the transition takes place over a narrow range compared to the polymer processing range, one could approximate the solid that is formed as having a single reference configuration during transition. Further, one can determine the fraction of the solid (or melt) using the second law of thermodynamics by prescribing a functional form for the entropy production associated with the phase change (for details, see Rao and Rajagopal [73]). Such a procedure furnishes an additional differential equation for the growth kinetics of the solid phase. By choosing a specific form for these fractions a priori, one can do away with the additional differential equation and hence it leads to a simpler model.

Now, let us examine the properties of Ψ introduced through Eq. (2.34). Above the glass transition temperature (few degrees above the glass transition temperature),

the material exists predominantly in a liquid-like state. The second term of Eq. (2.34) becomes very small and Ψ tends to Ψ_a . Similarly, below glass transition temperature at $\theta_g - \delta$, Ψ exactly equals Ψ_s . Since s is a constant, the 'width' of the transitional region is fixed. However, we shall show later in this section that the initiation of the mixture model is affected by both by deformation and the temperature. Thus, the transitional region can shift due to the temperature and the deformation. Here, θ_g is assumed to be simply the mid-point of the transitional regime.

The rate of entropy production (times temperature) due to mechanical working, $\hat{\xi}_a$, in the mixture, is assumed to be

$$\hat{\xi}_a = \frac{H(\theta - (\theta_g - \delta))}{1 + \exp(-s(\theta - \theta_g))} [2\nu^m(\theta, \mathbf{B}_{\kappa_p(t)}) \mathbf{D}_{\kappa_p(t)} \cdot \mathbf{B}_{\kappa_p(t)} \mathbf{D}_{\kappa_p(t)} + 2\nu_1^m(\theta, \mathbf{B}_{\kappa_p(t)}) \mathbf{D} \cdot \mathbf{D}], \quad (2.35)$$

where ν^m and ν_1^m are material functions corresponding to the viscoelastic component of the mixture. Viscosity functions are defined in such a way that they tend to appropriate limits, i.e., $\nu^m \rightarrow \nu^a$ and $\nu_1^m \rightarrow \nu_1^a$ as one approaches the initiation point and $\nu^m \rightarrow \nu^s$ and $\nu_1^m \rightarrow \nu_1^s$ as one nears the pure elastic solid regime. Recalling that below the glass transition temperature at $\theta_g - \delta$, the mixture behaves like an elastic solid. Here, $\nu^s (\gg \nu^a)$ and $\nu_1^s (\gg \nu_1^a)$ are viscosity functions sufficiently below glass transition temperature. The rate of entropy production due to mechanical working in the mixture should also become zero as one approaches the elastic regime. The above form of the dissipation complies with this requirement.

Further, on assuming $\hat{\xi}$ to be additive, and the rate of entropy production due to each mechanism to be non-negative, we have

$$\hat{\xi} = \xi_c + \hat{\xi}_a + \xi_p; \quad \xi_p, \hat{\xi}_a, \xi_c \geq 0. \quad (2.36)$$

Here, ξ_c is defined through Eq. (2.23), and $\frac{\xi_p}{\theta}$ is the rate of entropy production per

unit volume associated with phase change.

As a result of Eqs. (2.21) and (2.36), we arrive at the reduced dissipation equation

$$\mathbf{T} \cdot \mathbf{D} - \rho \dot{\Psi} - \rho \eta \dot{\theta} = \hat{\xi}_a + \xi_p; \quad \Psi = \epsilon - \eta \theta. \quad (2.37)$$

It can be shown that

$$\overline{\text{tr}(\mathbf{B}_{\kappa_r})} = 2\mathbf{B}_{\kappa_r} \cdot \mathbf{D}. \quad (2.38)$$

Substituting Eq. (2.34) into reduced dissipation equation [Eq. (2.37)], recognizing the derivative and the value of the Heavyside function is defined everywhere except at $\theta = \theta_g - \delta$, and using Eqs. (2.8) and (2.38), we obtain

$$\begin{aligned} & \left[\mathbf{T} - \frac{H(\theta - (\theta_g - \delta))2\rho\mathbf{B}_{\kappa_p(t)}}{1 + \exp(-s(\theta - \theta_g))} \frac{\partial\Psi_a}{\partial I_{\kappa_p(t)}} - \frac{2\rho\mathbf{B}_{\kappa_r}}{1 + \exp(s(\theta - \theta_g))} \frac{\partial\Psi_s}{\partial I_{\kappa_r}} \right] \cdot \mathbf{D} \\ & + \left[\frac{H(\theta - (\theta_g - \delta))2\rho\mathbf{B}_{\kappa_p(t)}}{1 + \exp(-s(\theta - \theta_g))} \frac{\partial\Psi_a}{\partial I_{\kappa_p(t)}} \right] \cdot \mathbf{D}_{\kappa_p(t)} \\ & - \rho \left[\frac{H(\theta - (\theta_g - \delta))}{1 + \exp(-s(\theta - \theta_g))} \frac{\partial\Psi_a}{\partial\theta} + \frac{1}{1 + \exp(s(\theta - \theta_g))} \frac{\partial\Psi_s}{\partial\theta} + \eta \right] \dot{\theta} \\ & - \rho \left\{ \frac{s}{\left[\exp\left(\frac{s}{2}(\theta - \theta_g)\right) + \exp\left(-\frac{s}{2}(\theta - \theta_g)\right) \right]^2} [H(\theta - (\theta_g - \delta))\Psi_a - \Psi_s] \right\} \dot{\theta} \\ & = \hat{\xi}_a + \xi_p. \end{aligned} \quad (2.39)$$

We recognize the last term on the left hand side of Eq. (2.39) to be the rate of entropy production (times temperature) per unit volume due to phase change because it is non-negative for $\Psi_a \geq \Psi_s$ and $\dot{\theta} \leq 0$ and is only significant in the transitional regime. One way to satisfy the above equation is to let the stress tensor, entropy, and rate of entropy production due to phase change and the dissipative processes to be given by the equations Eqs. (2.40) through (2.44) that are documented below:

$$\mathbf{T} = -p\mathbf{I} + \frac{H(\theta - (\theta_g - \delta))}{1 + \exp(-s(\theta - \theta_g))} \mathbf{T}_a + \frac{1}{1 + \exp(s(\theta - \theta_g))} \mathbf{T}_s, \quad (2.40)$$

where p is a Lagrange multiplier introduced due to the constraint of incompressibility.

Here, \mathbf{T}_a and \mathbf{T}_s are defined through

$$\mathbf{T}_a = \frac{\mu_a(\theta_a)\theta}{\theta_a} \mathbf{B}_{\kappa_p(t)} + 2\nu_1^m \mathbf{D} \text{ and } \mathbf{T}_s = \mu_s \mathbf{B}_{\kappa_r}. \quad (2.41)$$

The stress tensor is a mixture of a generalized Oldroyd fluid and a neo-Hookean solid weighted by a term that depends on the temperature. At one end of the transitional interval ($\theta = \theta_g + \delta$), Eq. (2.40) tends to a generalization of the Oldroyd liquid defined by Eqs. (2.25) and (2.32). The exact condition for switching from the fluid-like to a solid model needs to be discussed carefully, but before we do so, we recognize that the models are such that there are no jumps in the components of the stress tensor. At the other end of the transitional interval the mixture model yields a pure neo-Hookean response as expected.

The entropy of the mixture is given by

$$\eta = \frac{H(\theta - (\theta_g - \delta))}{1 + \exp(-s(\theta - \theta_g))} \left(\frac{-\partial\Psi_a}{\partial\theta} \right) + \frac{1}{1 + \exp(s(\theta - \theta_g))} \left(\frac{-\partial\Psi_s}{\partial\theta} \right), \quad (2.42)$$

where $\frac{-\partial\Psi_a}{\partial\theta}$ is given by Eq. (2.26). Like the stress tensor, the entropy of the mixture tends to the appropriate limits. There is no discontinuity in entropy as the models are switched from one phase to the other.

DSC studies on the transition from the melt to the solid state indicate that the specific heats of the pure liquid-like and solid-like phases change a little in the transitional regime (Richardson and Savill [74]). Thus, the rate effects are significant only in the mixture regime. The change in specific heat of the material gives us some idea of the microstructural rearrangement in the material in a gross sense. The experiments were conducted without deforming the material and as a result there is no entropy production due to mechanical working.

The entropy production associated with the transition is given through

$$-\rho \left\{ \frac{s}{\left[\exp\left(\frac{s}{2}(\theta - \theta_g)\right) + \exp\left(-\frac{s}{2}(\theta - \theta_g)\right) \right]^2} [H(\theta - (\theta_g - \delta))\Psi_a - \Psi_s] \right\} \dot{\theta} = \xi_p, \dot{\theta} < 0, \quad (2.43)$$

and

$$(\mathbf{T}_a - 2\nu_1^m \mathbf{D}) \cdot \mathbf{D}_{\kappa_p(t)} = 2\nu^m \mathbf{D}_{\kappa_p(t)} \cdot \mathbf{B}_{\kappa_p(t)} \mathbf{D}_{\kappa_p(t)}. \quad (2.44)$$

The constants θ_a and θ_s may be determined from calorimetry depending upon the rate of cooling.

On using equation Eq. (2.33), we find that the entropy of the solid component of the mixture, η_s , is given by,

$$\eta_s = \frac{-\partial \Psi_s}{\partial \theta} = C_s \ln \left(\frac{\theta}{\theta_s} \right). \quad (2.45)$$

The entropy of the solid is only a function of temperature. Using the definition of Helmholtz potential, Eq. (2.37), and Eq. (2.42), and the specific forms of the Helmholtz potentials, Eqs. (2.18) and (2.33), we obtain the internal energy of the mixture as

$$\epsilon = \frac{H(\theta - (\theta_g - \delta))}{1 + \exp(-s(\theta - \theta_g))} (\epsilon_a) + \frac{1}{1 + \exp(s(\theta - \theta_g))} \left[C_s(\theta - \theta_s) + \frac{\mu_s}{2\rho} (I_{\kappa_r} - 3) \right]. \quad (2.46)$$

The above equation, in the limit for an elastic solid, along with Eq. (2.45) at any arbitrary fixed temperature, reflects the energetic behavior of the material. The structure of equation Eq. (2.43) is such that it vanishes in the region where only a single phase is present. In other words, it is only non-zero during transition.

The Gibbs potential of all the coexisting phases at equilibrium (see Callen [7]) is the same. At the instant when the solid is formed (few degrees above θ_g), the

Helmholtz potential of both the phases are assumed to be the same, i.e.,

$$\Psi_a - \Psi_s \Big|_{\mathbf{B}_{\kappa_r} = \mathbf{I}} = \phi(\theta, \mathbf{B}_{\kappa_p(t)}) = 0. \quad (2.47)$$

On using Eqs. (2.18) and (2.33) in Eq. (2.47), the initiation surface is defined through the following equation:

$$C_a(\theta - \theta_a - \theta \ln \frac{\theta}{\theta_a}) + \frac{\mu_a(\theta_a)\theta}{2\rho\theta_a} \left(I_{\kappa_p(t)} - 3 \right) - C_s(\theta - \theta_s - \theta \ln \frac{\theta}{\theta_s}) = 0. \quad (2.48)$$

Eq. (2.47) provides the initiation criterion for the mixture model. In the absence of any deformation ($\mathbf{B}_{\kappa_p(t)} = \mathbf{I}$), the classical initiation condition is recovered. The initiation surface is similar to the yield surface in plasticity. Once the mixture model is initiated, the potential of the solid is less than that of the melt. After initiation, one has to make sure that $\Psi_a > \Psi_s$ in the transitional regime because Eq. (2.43) has to be met.

Once again we extremize $\hat{\xi}_a$, subject to the constraints Eqs. (2.44) and (2.30),

$$\Phi = \hat{\xi}_a + \hat{\lambda}_1 \left[2\nu^m \mathbf{D}_{\kappa_p(t)} \cdot \mathbf{B}_{\kappa_p(t)} \mathbf{D}_{\kappa_p(t)} - (\mathbf{T}_a - 2\nu_1^m \mathbf{D}) \cdot \mathbf{D}_{\kappa_p(t)} \right] + \hat{\lambda}_2 \text{tr}(\mathbf{D}_{\kappa_p(t)}), \quad (2.49)$$

where $\hat{\lambda}_1$ and $\hat{\lambda}_2$ are Lagrange multipliers due to the constraints.

The extremization procedure results in the following evolution equation for $\mathbf{B}_{\kappa_p(t)}$:

$$\overset{\nabla}{\mathbf{B}}_{\kappa_p(t)} = H(\theta - (\theta_g - \delta)) \frac{\mu_a(\theta_a)\theta}{\theta_a \nu^m} \left[\frac{3}{\text{tr}(\mathbf{B}_{\kappa_p(t)}^{-1})} \mathbf{I} - \mathbf{B}_{\kappa_p(t)} \right]. \quad (2.50)$$

In the limit $\nu^m \rightarrow \nu^a$, the Eq. (2.50) tends to the Eq. (2.32).

I. The fiber spinning problem

Fiber spinning consists of the following sub-processes. The polymer melt exits the die at 300°C . As the melt exits it swells to a certain diameter (see Fig. 3) denoted by d_s .

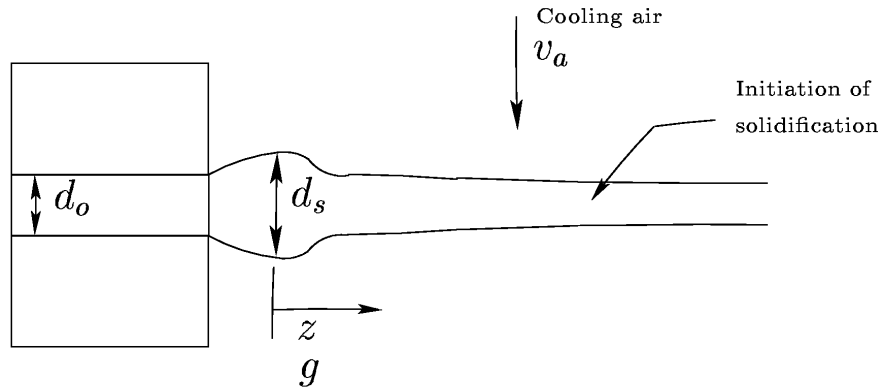


Fig. 3. The above is a sketch of a fiber spinning process. Gravity acts along the length of the spinline. The melt exits the die at 300°C and swells to a diameter d_s ; melt simulations are performed from this point onwards. The length of the spinline, l , is 1.5 m. The mass flow rate of the melt, m , at the capillary exit is $4.167\text{e-}5$ Kg/sec. The diameter of the capillary is 0.25 mm. As the melt is cooled by the cross flow air at a velocity of v_a , the solidification is initiated at some distance along the axis of the fiber.

Further along the spin line, the melt is continuously drawn. Cross flow air cools the melt. When the melt reaches a certain temperature (the glass transition), the fiber diameter almost becomes a constant. The solidified fiber is wound at a certain speed. In such a high speed spinning process, the effect of air drag on the lateral surface of the fiber and inertia is usually included. To achieve this, one has to solve for both the flow of the fluid and the deformation of the fiber in tandem. Instead, we choose to adopt a combined correlation provided by Denn [12] and Kase and Matsuo [33] for the air drag and the heat flux lost to the ambient air. For a detailed description of the fiber spinning process, the reader is referred to Ziabicki [88].

The fiber spinning process was first simulated by Kase and Matsuo [33]. They treated the polymer melt as a Newtonian fluid and neglected air drag and inertia.

Fisher and Denn [18] modeled the melt as a Maxwell liquid and included heat transfer effects. Later, Gagon and Denn [19] used the Phan-Thien Tanner constitutive equation to model the melt including the effects of air drag, gravity, inertia, and heat transfer. These simulations compare favorably with the experiments. George [21], modeled the melt as a Newtonian fluid. By choosing an exponential form for the elongational viscosity of the melt and by letting it attain a large value he was able to capture the plateau in the fiber spinning curves. However, such an effort leads only to a highly viscous Newtonian fluid; transition to a largely energetic solid phase is not achieved. The non-isothermal spinning process compares reasonably well with the experiments. Recently, Ottone and Deiber [47] modeled the melt spinning of PET as having both the characteristic of PTT and a Newtonian fluid. The calculations compares well with the data, but once again, the transition to a solid is not considered. Further, the model lacks a general thermodynamic basis. We find that none of the models discussed above have a general thermodynamic basis that naturally provides the initiation condition and the growth kinetics for the solid (see Rao and Rajagopal [73]), nor do such models consider the transition to a truly solid phase.

1. Melt calculations

We shall be interested in applying our theory to the problem of fiber spinning. In fiber spinning process, transverse temperature gradient exists, no matter how slender the fiber (see Matsuo and Kase [38], Vassilatos *et al.* [82], Chung and Iyer [9], Henson *et al.* [28]). However, for simplicity, we shall proceed with the thin-filament approximation of the fiber spinning problem.

The approximations leading to the mass, momentum and energy balance equations for the fiber spinning problem are well known and we shall not duplicate them here

(see chapter 15 in [51]).

Incorporating the drag into the balance of linear momentum along the z direction, neglecting surface tension effects, and under steady state conditions, we obtain

$$\frac{1}{A} \frac{d(AT_{zz})}{dz} + \rho g = \rho v_z \frac{dv_z}{dz} + \alpha, \quad (2.51)$$

where A is the cross sectional area of the fiber, v_z is the average velocity in the z direction, and α is the drag/unit surface area/unit length of the fiber and is given by (see Gagon and Denn [19])

$$\alpha = \frac{2}{d(z)} \rho_a v^2(z) C_f. \quad (2.52)$$

Here, ρ_a is the density of air, d is the current diameter of the fiber, and C_f , the air-drag coefficient is given by (see Denn [12]).

$$C_f = 2\beta \left(\frac{\nu_a}{\rho_a v(z) d(z)} \right)^{0.61}, \quad (2.53)$$

where β is a constant and ν_a is the viscosity of air.

The balance of mass, averaged across the cross section of the fiber, results in

$$d(z) = \sqrt{\left(\frac{4m}{\rho \pi v(z)} \right)}, \quad (2.54)$$

where m is the mass flow rate of the melt.

The components of the velocity gradient tensor in cylindrical-polar co-ordinates are

$$[\mathbf{L}] = \text{diag} \left(\frac{-1}{2} \frac{dv_z}{dz}, \frac{-1}{2} \frac{dv_z}{dz}, \frac{dv_z}{dz} \right). \quad (2.55)$$

The above equation satisfies the constraint of incompressibility ($\text{tr} \mathbf{D} = 0$).

For an elongational flow of an incompressible material, let us assume that the com-

ponents of $\mathbf{B}_{\kappa_p(t)}$ in the spatial form are

$$[\mathbf{B}_{\kappa_p(t)}] = \text{diag} \left(\frac{1}{\sqrt{B_{zz}(z)}}, \frac{1}{\sqrt{B_{zz}(z)}}, B_{zz}(z) \right). \quad (2.56)$$

As a result of the averaging process outlined in Pearson [51], recalling that the surface tension effects have been neglected, we have

$$T_{rr}(z) \simeq T_{\theta\theta}(z) \simeq 0. \quad (2.57)$$

On using the constitutive equation (2.25) and the Eqs. (2.55) and (2.56), we find that the two components of the stress tensor, i.e., T_{rr} and $T_{\theta\theta}$, are the same and is consistent with the above equation. By using Eqs. (2.57) and (2.25), we find that the Lagrange multiplier p is given by

$$p = \frac{\mu_a(\theta_a)\theta}{\theta_a} \left(\frac{1}{\sqrt{B_{zz}}} \right) - \nu_1^a(\theta) \frac{dv_z}{dz}. \quad (2.58)$$

Substituting the above equation into Eq. (2.25), we get

$$T_{zz} = \frac{\mu_a(\theta_a)\theta}{\theta_a} \left(\frac{B_{zz}^{\frac{3}{2}} - 1}{\sqrt{B_{zz}}} \right) + 3\nu_1^a(\theta) \frac{dv_z}{dz} = t_{zz} - t_{rr}, \quad (2.59)$$

where t_{zz} and t_{rr} are the extra stress components. The material function ν_1^a is assumed to have the following form:

$$\nu_1^a(\theta) = \nu_1^o(\theta_r) \exp \left[C_1 \left(\frac{1}{\theta} - \frac{1}{\theta_r} \right) \right], \quad (2.60)$$

where ν_1^o , θ_r , and C_1 are material constants.

Substituting Eq. (2.59) into Eq. (2.51), the balance of momentum in the z direction

reduces to

$$\begin{aligned} & \frac{\mu_a(\theta_a)}{\theta_a} \left[\theta \frac{dB_{zz}}{dz} \left(1 + \frac{1}{2B_{zz}^{3/2}} \right) + \frac{B_{zz}^{3/2} - 1}{\sqrt{B_{zz}}} \left(\frac{d\theta}{dz} \right) \right] \\ & + 3 \left[\frac{d\nu_1^a(\theta)}{dz} \frac{dv_z}{dz} + \nu_1^a(\theta) \frac{d^2v_z}{dz^2} \right] + \frac{T_{zz}}{A} \frac{dA}{dz} + \rho g = \rho v_z \frac{dv_z}{dz} + \alpha . \end{aligned} \quad (2.61)$$

The evolution equation, Eq. (2.50), in the spatial representation for a steady process, in cylindrical-polar coordinates, turns out to be

$$\frac{dB_{zz}}{dz} = \frac{2B_{zz}}{v_z} \frac{dv_z}{dz} + \frac{1}{v_z} \frac{\mu_a(\theta_a)\theta}{\theta_a \nu^a(\theta)} \left(\frac{3B_{zz}}{2B_{zz}^{3/2} + 1} - B_{zz} \right) . \quad (2.62)$$

The three surviving components of the evolution equation, Eq. (2.50), result in the same differential equation as Eq. (2.62). Here, $\nu^a(\theta)$ is defined as follows

$$\nu^a(\theta) = \nu^o(\theta_r) \exp \left[C \left(\frac{1}{\theta} - \frac{1}{\theta_r} \right) \right] , \quad (2.63)$$

where ν^o , θ_r , and C are material constants.

The energy balance equation, neglecting radiation, is

$$\rho \dot{\epsilon}_a = \mathbf{T} \cdot \mathbf{D} - \text{div}(\mathbf{q}) , \quad (2.64)$$

where $\dot{\epsilon}_a$ is the time rate of internal energy per unit mass of the melt. The last term of the above equation is related to the heat conduction.

The above equation, within the context of the approximation, on using Eqs. (2.29), (2.57), and (2.55), reduces to

$$\rho C_a \frac{d\theta}{dz} v_z = T_{zz} \frac{dv_z}{dz} - \frac{4}{d} h(\theta - \theta_\infty) , \quad (2.65)$$

where h , is the convection heat transfer coefficient given by (see Denn [12]):

$$h = \frac{k_a}{d} \beta Pr^{1/3} Re^{0.39} \left[1 + 64 \left(\frac{v_a}{v_z} \right)^2 \right]^{0.166}, \quad (2.66)$$

where k_a is the thermal conductivity of air, Pr is the Prandtl number of air, Re is the Reynolds number of air based on the diameter of the fiber as the characteristic dimension, and v_a is the cross flow cooling air velocity. In the Eq. (2.65), the effects of radiation and axial conduction were ignored.

2. Mixture calculations

We know that

$$\dot{\mathbf{B}}_{\kappa_r} = \mathbf{L}\mathbf{B}_{\kappa_r} + \mathbf{B}_{\kappa_r}\mathbf{L}^T, \quad (2.67)$$

where κ_r is the reference configuration for the solid that is formed. Eqs. (2.55) and (2.56) are also valid in the mixture region. Using Eq. (2.55), we can express any one of the three components in the spatial form. In the case of the equation along z -direction, we obtain

$$\frac{dB_{zz}}{dz}v_z = 2\frac{dv_z}{dz}B_{zz}. \quad (2.68)$$

As a result of the Eqs. (2.40), (2.57) and (2.68) and the incompressibility constraint, it immediately follows that the components of \mathbf{B}_{κ_r} in the spatial form are

$$[\mathbf{B}_{\kappa_r}] = \text{diag} \left(\frac{v_z(z_o)}{v_z(z)}, \frac{v_z(z_o)}{v_z(z)}, \frac{v_z^2(z)}{v_z^2(z_o)} \right). \quad (2.69)$$

where $v_z(z_o)$ is the velocity of the fiber at the instant of initiation.

The arguments advanced in the previous sub-section for simplifying the balance equations can be applied here (after initiation) as well.

By following a procedure similar to that described in the previous sub-section,

the Lagrange multiplier is determined to be

$$p = \frac{H(\theta - (\theta_g - \delta))}{1 + \exp(-s(\theta - \theta_g))} \left[\frac{\mu_a(\theta_a)\theta}{\theta_a} \left(\frac{1}{\sqrt{B_{zz}}} \right) - \nu_1^m(\theta) \frac{dv_z}{dz} \right] + \frac{\mu_s}{1 + \exp(s(\theta - \theta_g))} \left[\frac{v_z(z_o)}{v_z(z)} \right]. \quad (2.70)$$

The functional form for ν_1^m is taken to be

$$\nu_1^m(\theta) = \frac{\nu_1^a(\theta)}{1 + \exp(-s(\theta - \theta_g))} + \frac{\nu_1^s}{1 + \exp(s(\theta - \theta_g))}, \quad (2.71)$$

where $\nu_1^a(\theta)$ is given by Eqs. (2.60) and ν_1^s is a constant. The Eq. (2.71) tends to appropriate limits; there is no jump in the viscosity function defined over the entire range.

The component of the stress tensor in Eq. (2.40), in the z-direction, on using the above equation, is

$$T_{zz} = \frac{H(\theta - (\theta_g - \delta))}{1 + \exp(-s(\theta - \theta_g))} \left[\frac{\mu_a(\theta_a)\theta}{\theta_a} \left(\frac{B_{zz}^{\frac{3}{2}} - 1}{\sqrt{B_{zz}}} \right) + 3\nu_1^m(\theta) \frac{dv_z}{dz} \right] + \frac{\mu_s}{1 + \exp(s(\theta - \theta_g))} \left[\frac{v_z^2(z)}{v_z^2(z_o)} - \frac{v_z(z_o)}{v_z(z)} \right]. \quad (2.72)$$

The balance of linear momentum, Eq. (2.51), in the z direction becomes

$$\begin{aligned}
& \frac{H(\theta - (\theta_g - \delta))}{1 + \exp(-s(\theta - \theta_g))} \left\{ \frac{\mu_a(\theta_a)}{\theta_a} \left[\theta \frac{dB_{zz}}{dz} \left(1 + \frac{1}{2B_{zz}^{3/2}} \right) + \frac{B_{zz}^{\frac{3}{2}} - 1}{\sqrt{B_{zz}}} \left(\frac{d\theta}{dz} \right) \right] \right. \\
& \left. + 3 \left[\frac{d\nu_1^m(\theta)}{dz} \frac{dv_z}{dz} + \nu_1^m(\theta) \frac{d^2v_z}{dz^2} \right] \right\} \\
& + \frac{\mu_s}{1 + \exp(s(\theta - \theta_g))} \left[\frac{2v_z(z)}{v_z^2(z_o)} + \frac{v_z(z_o)}{v_z^2(z)} \right] \frac{dv_z}{dz} + \\
& \frac{s}{\left[2 \cosh \left(\frac{s}{2}(\theta - \theta_g) \right) \right]^2} \frac{d\theta}{dz} \left\{ \left[\frac{\mu_a(\theta_a)\theta}{\theta_a} \left(\frac{B_{zz}^{\frac{3}{2}} - 1}{\sqrt{B_{zz}}} \right) + 3\nu_1^m(\theta) \frac{dv_z}{dz} \right] H(\theta - (\theta_g - \delta)) \right. \\
& \left. - \mu_s \left[\frac{v_z^2(z)}{v_z^2(z_o)} - \frac{v_z(z_o)}{v_z(z)} \right] \right\} + \frac{T_{zz}}{A} \frac{dA}{dz} + \rho g = \rho v_z \frac{dv_z}{dz} + \alpha .
\end{aligned} \tag{2.73}$$

The evolution equation is the same as Eq. (2.62) with $\nu^a(\theta)$ replaced by $\nu^m(\theta)$, with ν^m being defined as follows:

$$\nu^m(\theta) = \frac{\nu^a(\theta)}{1 + \exp(-s(\theta - \theta_g))} + \frac{\nu^s}{1 + \exp(s(\theta - \theta_g))}, \tag{2.74}$$

where $\nu^a(\theta)$ is given by the Eq. (2.63) with ν^s being a constant. This form guarantees a large increase in viscosity during the transition. The balance of energy in the spatial form is

$$\begin{aligned}
& \rho \left\{ \frac{H(\theta - (\theta_g - \delta))}{1 + \exp(-s(\theta - \theta_g))} \left(C_a \frac{d\theta}{dz} v_z \right) + \right. \\
& \frac{1}{1 + \exp(s(\theta - \theta_g))} \left[C_s \frac{d\theta}{dz} v_z + \frac{\mu_s}{\rho} \left(\frac{v_z^2(z)}{v_z^2(z_o)} - \frac{v_z(z_o)}{v_z(z)} \right) \frac{dv_z}{dz} \right] + \\
& \frac{s}{\left[2 \cosh \left(\frac{s}{2}(\theta - \theta_g) \right) \right]^2} \frac{d\theta}{dz} v_z \left[H(\theta - (\theta_g - \delta)) C_a(\theta - \theta_a) - C_s(\theta - \theta_s) \right. \\
& \left. \left. - \frac{\mu_s}{2\rho} \left(\frac{2v_z(z_o)}{v_z(z)} + \frac{v_z^2(z)}{v_z^2(z_o)} - 3 \right) \right] \right\} = T_{zz} \frac{dv_z}{dz} - \frac{4}{d} h(\theta - \theta_\infty),
\end{aligned} \tag{2.75}$$

where ϵ is given by Eq. (2.46), and T_{zz} is given by Eq. (2.72). The three equations, Eqs. (2.73), (2.62), and (2.75), are those that need to be solved.

3. Parameters used in the simulation

In the absence of deformation, on using Eq. (2.46), the rate of change of internal energy is

$$\dot{\epsilon} = \left\{ \frac{H(\theta - (\theta_g - \delta))}{1 + \exp(-s(\theta - \theta_g))} C_a + \frac{1}{1 + \exp(s(\theta - \theta_g))} C_s + \frac{s}{\left[2 \cosh\left(\frac{s}{2}(\theta - \theta_g)\right)\right]^2} [H(\theta - (\theta_g - \delta)) C_a (\theta - \theta_a) - C_s (\theta - \theta_s)] \right\} \dot{\theta} \quad (2.76)$$

From the first law of thermodynamics, the rate of removal of heat from the sample is the rate at which the internal energy of the given mass of substance is decreasing. Therefore, $\frac{\dot{\epsilon}}{\dot{\theta}}$ is known. The rate effects are significant only in the transitional regime. The Fig. 4 is plotted for different values of θ_s using Eq. (2.76). Referring to the Fig. 4, the dotted curve is similar to the one obtained experimentally for 'slow' cooling rates while the solid curve is typical of 'fast' cooling rates. The fiber spinning process involves high cooling rates. Thus, it is reasonable to assume that the specific heat response of PET to be the continuous curve. We picked the specific heat for the melt to be 2000 J/KgK, namely that for the molten PET at 270°C (see Brandrup and Immergut [5]) and the specific heat for the PET in the solid phase to be 1250 J/KgK which corresponds to the specific heat at 55°C (see Brandrup and Immergut [5]). The values of θ_a and θ_s are obtained using specific heat response curves and the initiation condition, namely, Eq. (2.48). The 'width' of the transition region is assumed to be 10°C. The parameter s is chosen such that the complete transition from a liquid-like melt to an elastic solid is effected in the transitional region. The glass transition temperature, θ_g , is assumed to be $\theta(z_o) + \delta$ (mid-point of the transitional regime),

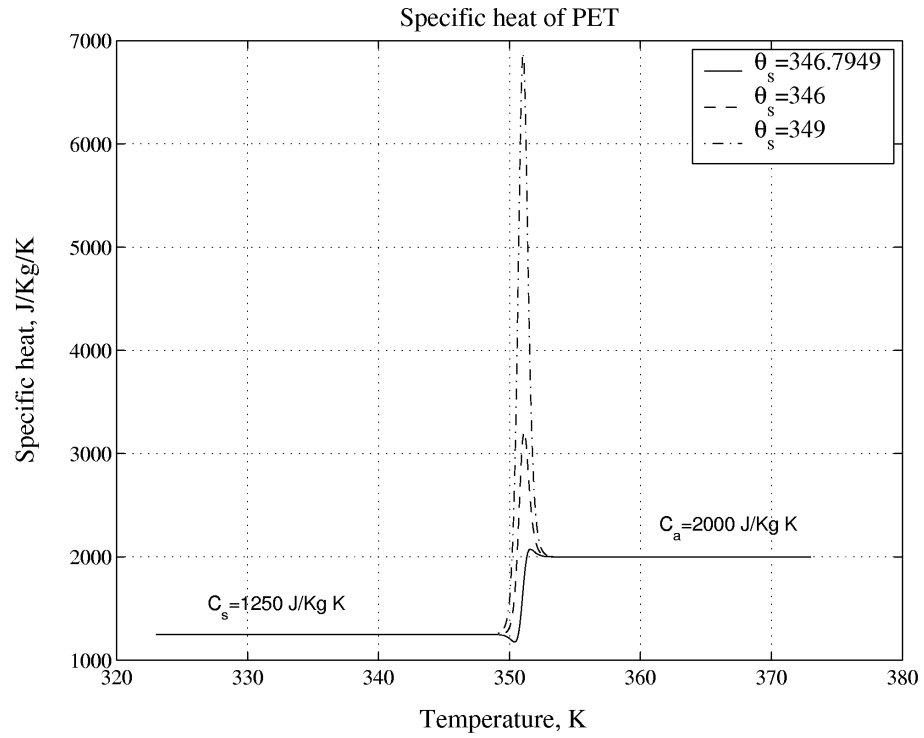


Fig. 4. This figure is a plot of specific heat of the material calculated using Eq. (2.76) for different values of θ_s .

where z_o is the distance at which the mixture model is initiated. The half-'width' of the transitional region, δ , is taken to be $5^\circ C$. The parameters listed in Table (I) below, namely, l , θ_o , m , θ_∞ , and V_a are the parameters used in the experiments performed by George [21]. The diameter of the maximum swell section (which occurs close to the die exit), d_s , is calculated using the correlation provided by George [21]. This correlation does not include the effects of the take-up speed on the diameter of the maximum swell section; experimental measurements of the diameter of the spun fiber in the fiber spinning process (see Ziabicki [88]) show that the effects of the take-up speed on the diameter is minimal provided it is measured very close to the die exit (few die-diameters). The density of PET is calculated using the correlation used by Ottone and Deiber [47] at $300^\circ C$. Material constants used in the heat transfer and air-drag correlations (related to the properties of air), i.e., ρ_a , ν_a , K_a , and Pr are the same values used by Ottone and Deiber [47]. The parameters μ_a , ν^o , ν_1^o , ν^s , ν_1^s , C , C_1 , and μ_s are not known a priori and must be determined after fitting the model to suitable experiments. Since there are not enough experiments that will enable the determination of all the new material constants uniquely, we are left with no option but to make judicious choices them. All other material parameters are either known from earlier experiments or can be determined from existing experiments.

Doufas and McHugh [13] have carried out extensive sensitivity analysis for their model. Here, we do not carry out a similar detailed analysis. However, for the range of take-up speeds considered, we found that our model is quite robust, in that the results are not greatly altered by minor changes in the parameters. The temperature profiles are sensitive to the values taken by β as noted by Denn [12]. The values of β ranging from 0.135 to 0.5 have been reported in the literature (see Denn [12]). In fact, by picking different different values of β for the melt and the solid, to agree with the value suggested by Denn [12] for the melt ($\beta \approx 0.3$), and the value suggested

by Matsui [37] for the solid ($\beta = 0.185$), we can even get better agreement with the experimental data for the temperature profile. We choose not to do so. The solutions are quite robust to perturbations in the other parameters.

Table (Table (I)) lists the constants used in the simulation.

4. Boundary, initiation, and interface conditions

As the melt exits the die, it swells to a diameter d_s . Using the correlation provided by George [21], the maximum swell diameter for the PET melt is calculated to be 0.44mm for a capillary diameter of the die of 0.25 mm. From the mass flow rate, one can calculate the average velocity, v_e , at the maximum swell section. Further, at this section, the gradient of velocity is zero ($\left. \frac{dv_z}{dz} \right|_{z=0} = 0$). The temperature at the exit, θ_o , is $300^\circ C$. The take-up velocity, v_t , is also known. Summarizing, the boundary conditions are

$$v_z(0) = v_e, \left. \frac{dv_z}{dz} \right|_{z=0} = 0, \theta(0) = \theta_o, \text{ and } v_z(l) = v_t, \quad (2.77)$$

where l is the length of the spin-line.

The mixture model, using Eqs. (2.47), (2.18) and (2.33), will be initiated when the following condition is satisfied

$$C_a(\theta - \theta_a - \theta \ln \frac{\theta}{\theta_a}) + \frac{\mu_a(\theta_a)\theta}{2\rho\theta_a} \left(\frac{2 + B_{zz}^{\frac{3}{2}}}{\sqrt{B_{zz}}} - 3 \right) - C_s(\theta - \theta_s - \theta \ln \frac{\theta}{\theta_s}) = 0. \quad (2.78)$$

The interface conditions are

$$v_z(z_o^-) = v_z(z_o^+), \left. \frac{dv_z}{dz} \right|_{z=z_o^-} = \left. \frac{dv_z}{dz} \right|_{z=z_o^+}, \theta(z_o^-) = \theta(z_o^+), \text{ and } B_{zz}(z_o^-) = B_{zz}(z_o^+), \quad (2.79)$$

Table I. The list of constants used in the simulation of fiber spinning problem

Material parameter/others	Numerical value
Length of spinline, l	1.5 m
Diameter of maximum swell section, d_s	0.44 mm
Exit temperature of melt, θ_o	300° C
Mass flow rate of the melt, m	4.167x10 ⁻⁵ Kg/sec
Density of the melt and air, ρ and ρ_a	1206 Kg/m ³ , 1.2 Kg/m ³
Reference temperature of melt, θ_a	347.1218° K
Reference temperature of solid, θ_s	344.7950° K
Reference temperature for viscosity of melt, θ_r	568° K
Modulus of melt, μ_a	3700 Pa
Viscosity of the melt at θ_r , ν^o ,	31 Pa Sec
Viscosity of the melt at θ_r , ν_1^o ,	200 Pa Sec
Viscosity of the melt below glass transition, ν^s and ν_1^s	1x10 ⁶ Pa Sec, 4x10 ⁵ Pa Sec
Specific heat capacity of the melt and the solid, C_a and C_s	2000J/KgK, 1250J/KgK
Exponential constant of Eq. (2.63), C	4800 K
Exponential constant of Eq. (2.60), C_1	6500 K
Modulus characterizing the solid, μ_s	8x10 ⁷ Pa
Material constant, s	5 K ⁻¹
Ambient temperature, θ_∞	30° C
Viscosity of air, ν_a	1.8x10 ⁻⁵ Pa sec
Thermal conductivity of air, K_a	0.03 W/m K
Cross-flow cooling air velocity, V_a	0.2 m/sec
Prandtl number of air, Pr	0.684
Drag constant, β	0.31

where z_o is the distance at which Eq. (2.78) is satisfied.

The conditions when the temperature hits $\theta_g - \delta$ are

$$v_z(z_1^-) = v_z(z_1^+) \text{ and } \theta(z_1^-) = \theta(z_1^+) , \quad (2.80)$$

where z_1 is the distance along the spin-line at which the temperature is $\theta_g - \delta$.

5. Results and conclusions

The system of equations governing the flow of the melt are solved as an initial value problem using Matlab until the initiation surface, [refer to Eq. (2.78)] is reached. On reaching the initiation surface, the system of equations corresponding to the mixture is activated with the values of v_z , B_{zz} , θ , and $\frac{dv_z}{dz}$ at the instant of initiation as initial conditions. The system of equations for the mixture are solved until the temperature reaches $\theta_g - \delta$. The velocity and the temperature obtained at $z = z_1$ is taken as the initial conditions for the system of equations corresponding to the pure solid, Eqs. (2.73) and (2.75), without the terms that are multiplied by the Heavyside function. The value of B_{zz} at $z = 0$ is unknown. Its value is guessed and the both the system of equations are solved consecutively. The value of the take-up velocity achieved is compared with the fourth boundary condition of Eq. (2.77) and B_{zz} at $z = 0$ is fine tuned until the required value for the take-up is reached. The system of equations corresponding to the mixture are stiff and hence it requires a stiff-equation solver. The figures [Figs. 5, 6, 7, and 8] represent the results obtained. In Fig. 7 the diameter of the fiber varies along the spin-line. The diameter was calculated using the predicted velocity and Eq. (2.54). The bold crosses represent the initiation of mixture model. Notice that as the melt solidifies, the diameter of the fiber becomes constant. Fig. 8 represents the predicted stress response. After initiation, the stress increases almost linearly in the solidified part of the fiber where air drag effects are important.

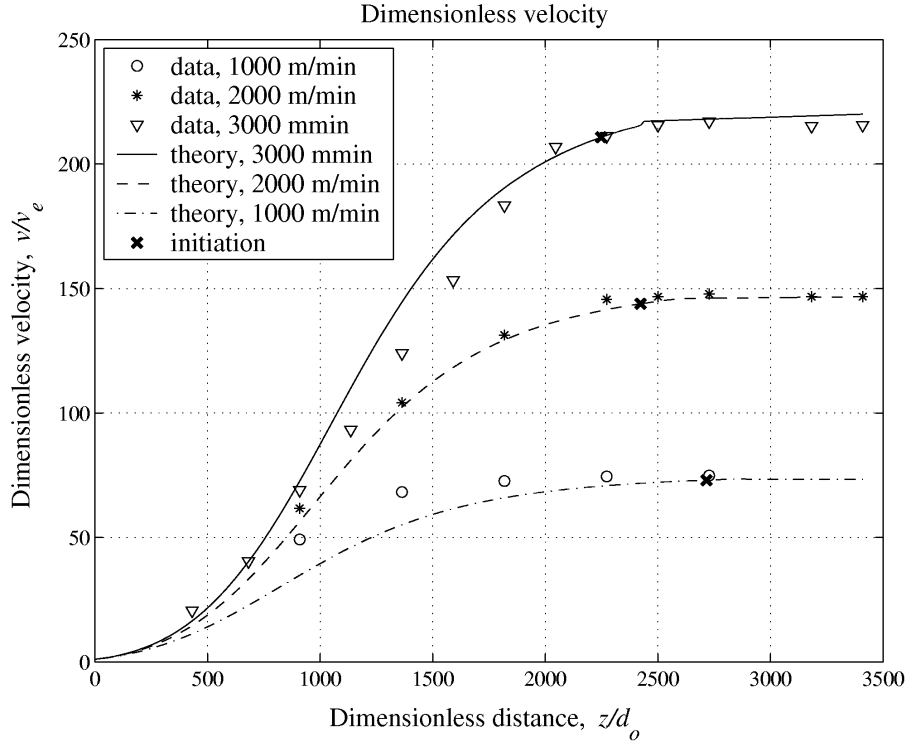


Fig. 5. The theoretical predictions are represented by solid lines, while, the data obtained by George (1982), is denoted by points. The solid crosses represent the point of initiation of the mixture model. Here, d_o is the same as d_s . The average velocity at the maximum swell section, v_e , is used to non-dimensionalize velocity.

Further, the solutions exhibit increasing slope for increasing take-up speeds. Experiments conducted on a six meter spinline for PET (see pg. 186 Ziabicki [88]) supports the fact that the stress increases linearly in the solidified portion of the fiber.

We notice that the solutions for the dimensionless velocity compare well with experiments. In fact, when the velocity and temperature plots are made in the same scales adopted by Ottone and Deiber [47], we find that the plot of the non-dimensionalized velocity with the non-dimensionalized distance agrees better with the experiment

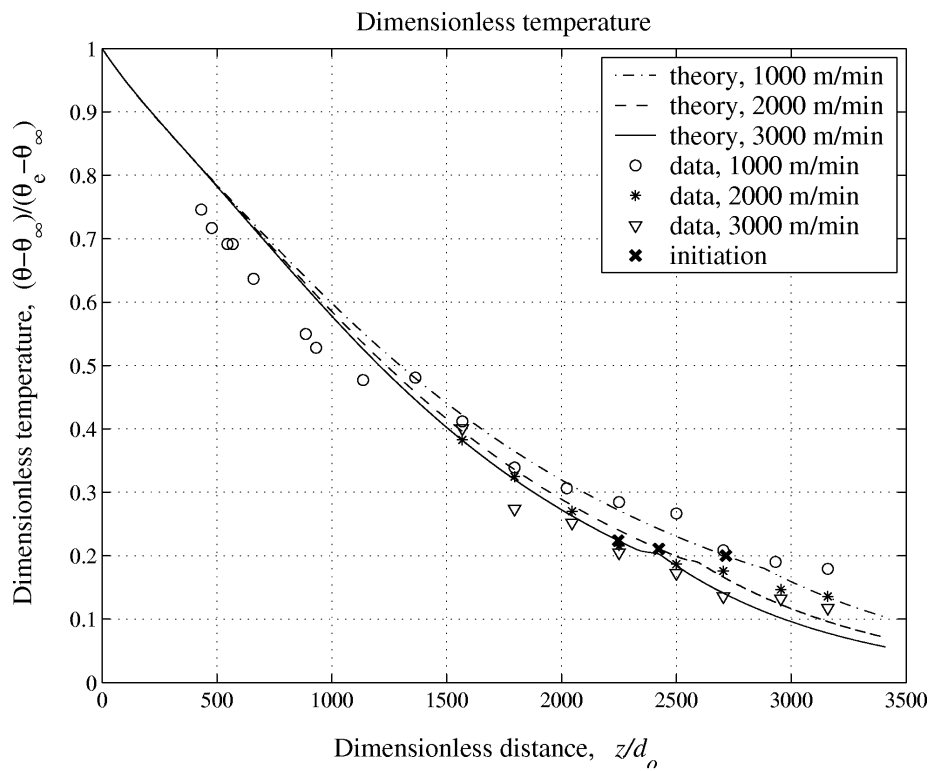


Fig. 6. The temperature profiles for three different take-up speeds.

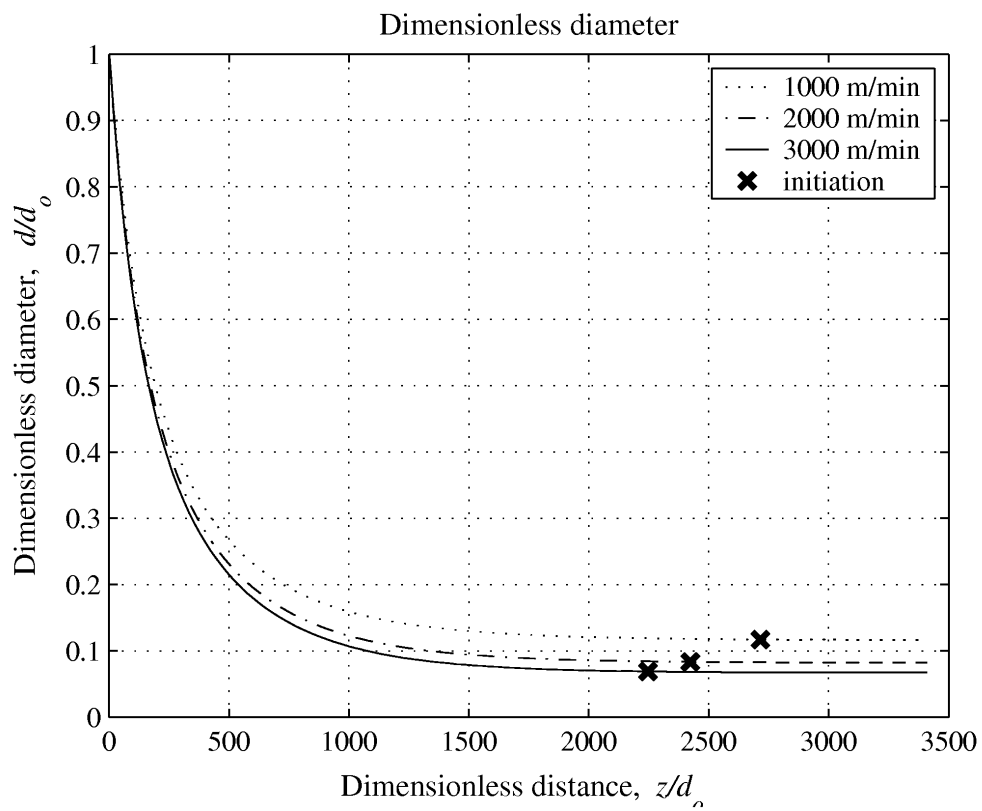


Fig. 7. The figure shows the variation of diameter of the drawn fiber along the spin-line.

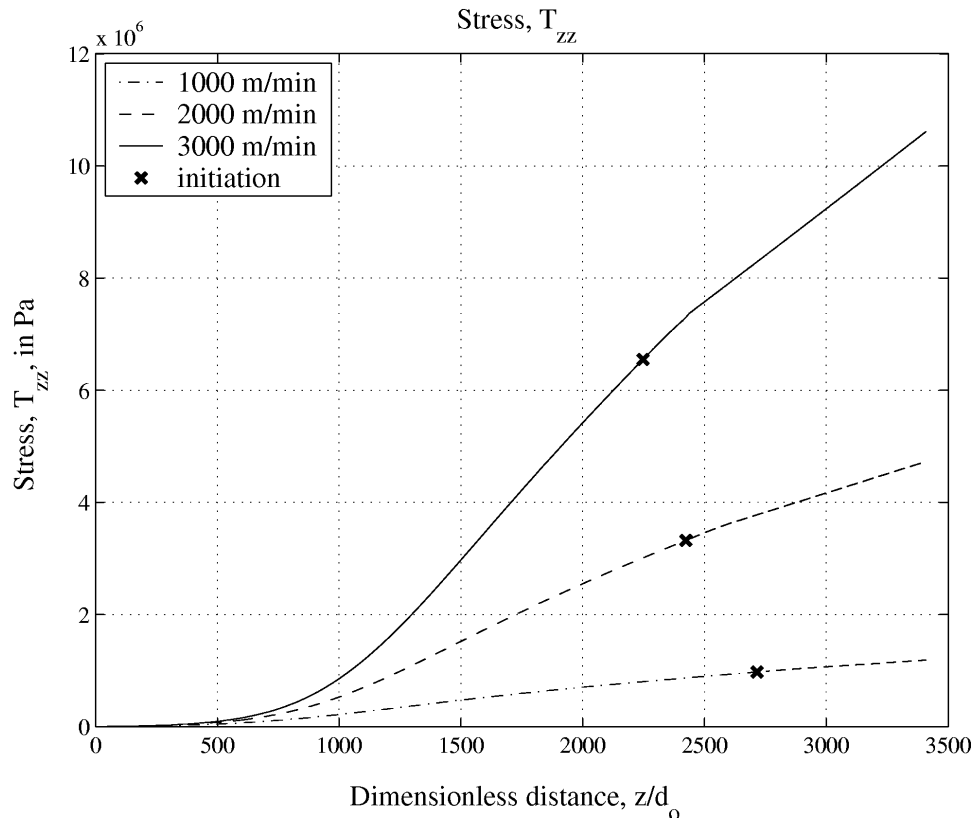


Fig. 8. The figure shows the stress along the length of the fiber. After initiation, the predicted stress shows a ‘linear’ response with an increasing slope for increasing take-up speeds.

than the results of Ottone and Deiber [47]. However, this has been achieved within a framework that switches through the glass transition in a continuous manner. On the other hand, in the studies by Ottone and Deiber [47], Fisher and Denn [18] and elsewhere, on reaching glass transition, an adhoc determination is made to draw a horizontal line signifying that the non-dimensionalized velocity is a constant. If this adhoc determination is not made, the velocity would not plateau but continue to increase. Here, on the other hand, we have a theory that switches appropriately from a model for the melt through glass transition to an elastic solid (the previous models also merely assume a fluid with sufficiently large viscosity). We also note that the predictions of the current theory for the variation of the temperature of the fiber with distance agrees well with the experimental results (see Fig. 6). We should also mention that the results of Doufas and McHugh [13] also fit the results very well, and in some ranges of length along the spin line and take-up speeds agrees better than our predictions while for some other ranges our results agree slightly better with the experimental results. But on the whole the theories of Doufas and McHugh [13] as well as ours agree well with respect to the temperature profile.

CHAPTER III

A THERMOMECHANICAL FRAMEWORK FOR THE TRANSITION OF A
VISCOELASTIC LIQUID TO A VISCOELASTIC SOLID*

We present a thermomechanical framework to describe the transition from a viscoelastic fluid to a viscoelastic solid, in which the kinetics associated with the transition and the change of response characteristics prior to, during, and after the transition are modeled within a unified setting. The procedures fit within the general thermodynamic framework that has been developed to describe the response of materials that can exist stress free in multiple configurations. The current study is a generalization of the studies by Rao and Rajagopal [73] and Kannan *et al.* [32] that addresses the solidification of a polymeric melt into an elastic solid.

A. Introduction

Recently, a general thermodynamic framework was put into place to study the problem of the crystallization (and solidification to an amorphous solid) of polymer melts. Within this framework, the crystallization kinetics and the change in the response characteristics of the material as it crystallizes are a consequence of certain thermodynamic requirements. Here, we shall not get into a detailed discussion of the framework, but refer the reader to Rao and Rajagopal [73] for the same. The main features of the framework are that bodies can exist in more than one natural configuration, say a stress-free state, and in general thermodynamic processes these configurations evolve. If $\kappa_t(B)$ denotes the current configuration of the body, then $\kappa_{p_m(t)}(B)$ denotes

*Reprinted with permission from “A THERMOMECHANICAL FRAMEWORK FOR THE TRANSITION OF A VISCOELASTIC LIQUID TO A VISCOELASTIC SOLID” by K. KANNAN and K.R. RAJAGOPAL, 2002. *MATH. MECH. SOLIDS*, VOL. 9, PP. 37-59. 2004 by SAGE PUBLICATIONS.

a stress-free state corresponding to $\kappa_t(B)$ (see Fig. 9). It is possible to reach different stress-free states depending on the class of process under consideration. A detailed discussion of the notion of natural configurations can be found in Rajagopal [58]. The evolution of these natural configurations is determined by requiring that amongst all processes that are possible for a material in a given state, the one that is chosen is that which maximizes the entropy production. The response of many viscoelastic polymers (those that have instantaneous elasticity) can then be described through a class of elastic response functions from these evolving natural configurations. The general framework is not restricted to materials that have instantaneous elastic response. The classical Navier-Stokes fluid and power-law fluids that do not have instantaneous elasticity, as well as viscoelastic bodies that do not possess instantaneous elasticity can and have been described within the framework. Here, we use the framework to describe the transition from a viscoelastic polymeric melt to a viscoelastic solid. The earlier studies by Rao and Rajagopal [73] and Kannan *et al.* [32] was restricted to a transition of a polymeric melt to an elastic solid. However, since the polymer melt solidifies into a viscoelastic solid rather than an elastic solid, to model the transition of a polymeric melt accurately, it is necessary to mathematically model this transition to a viscoelastic solid.

At sufficiently high temperatures (above its melting point), a polymer exists in a melt-like state. As the polymer cools, it transitions to a pure solid within a span of a few degrees. Typically, for many polymers, the transitional region is of the order of a few degrees, while that of the polymer processing regime is usually a few hundred degrees.

We shall model the polymer melt as a rate-type viscoelastic liquid and the viscoelastic solid as a non-linear three parameter viscoelastic solid. The transitional regime is assumed to be characterized by a mixture of a viscoelastic solid and the viscoelastic

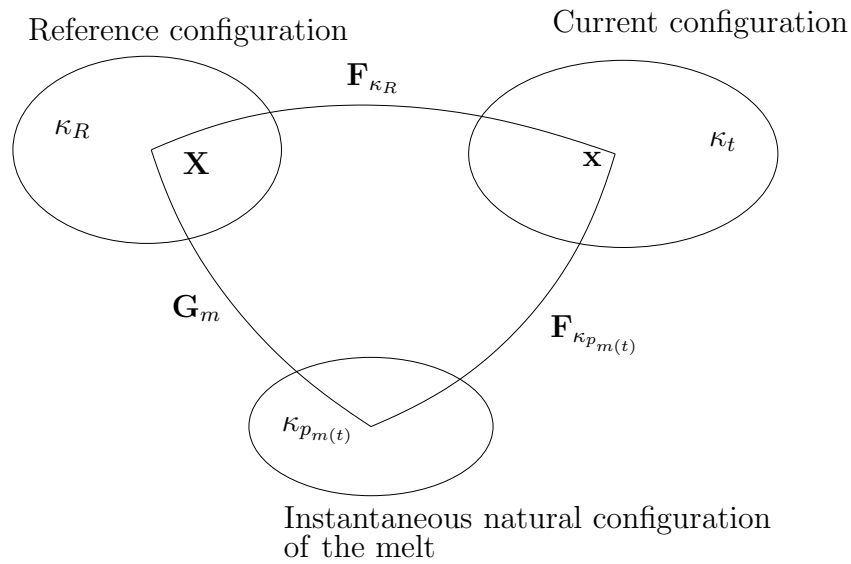


Fig. 9. The figure represents the configurations associated with the melt. The point \mathbf{X} is the position occupied by the particle in the reference configuration. The point \mathbf{x} is the current position of the particle.

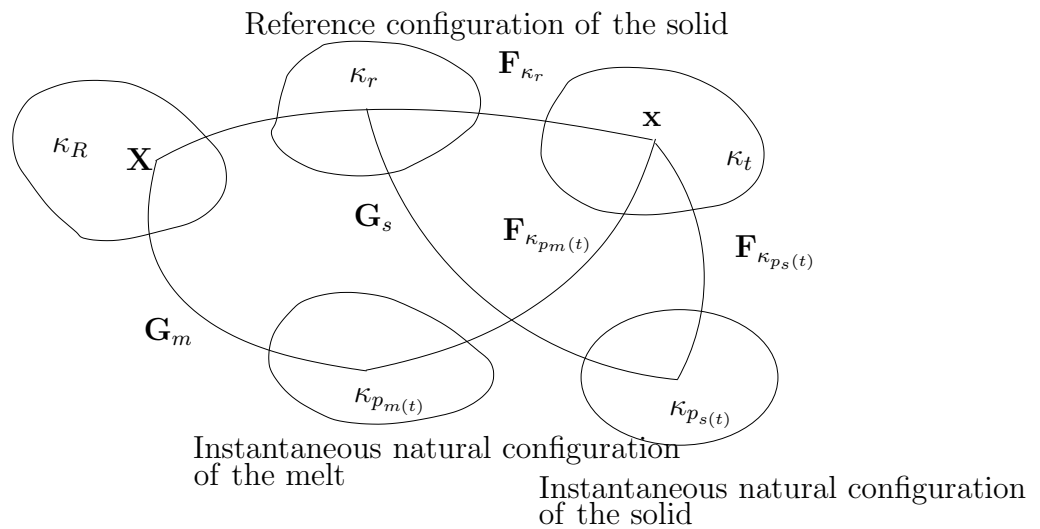


Fig. 10. This figure represents the configurations associated with the mixture. The configuration associated with the solid at the instant of the initiation of the mixture model is denoted by κ_r .

polymer, i.e., melt. The viscoelastic solid is assumed to be born in an amorphous state $\kappa_r(B)$ (see Fig. 10). Since it is amorphous, we shall assume that the solid is isotropic with respect to the fixed configuration $\kappa_r(B)$ at which it is formed, and an evolving configuration $\kappa_{p_s(t)}(B)$ is introduced to capture the evolving natural configuration from which the body responds elastically (see §5 for details). Since the solid is formed continuously in the transitional region, one should use an infinite sequence of configurations to describe the response of the solid (see Rao and Rajagopal [73]). However, as the transitional regime is only a few degrees, we can use a single configuration, i.e., $\kappa_r(B)$ (see [32]) to denote an 'average configuration' in which the melt solidifies and an evolving configuration $\kappa_{p_s(t)}(B)$ as the viscoelastic solid deforms, to approximate the response of the solid.

B. Kinematics

Let $\kappa_R(B)$ and $\kappa_t(B)$ denote the reference and the current configuration of the body B at time t respectively. By the motion of a body we mean a one to one mapping that assigns to each point $\mathbf{X} \in \kappa_R(B)$, a point $\mathbf{x} \in \kappa_t(B)$, for each t ,

$$\mathbf{x} = \chi_{\kappa_R}(\mathbf{X}_{\kappa_R}, t). \quad (3.1)$$

Let $\kappa_r(B)$ denote the 'average configuration' during which the melt solidifies. Then, we have

$$\mathbf{X}_{\kappa_r} = \chi_{\kappa_R}(\mathbf{X}_{\kappa_R}, t_i), \quad \mathbf{X}_{\kappa_r} \in \kappa_r(B) \text{ (or } \kappa_{t_i}(B)). \quad (3.2)$$

One can also represent the motion of the body for time $t \geq t_i$ (t_i denotes the time when solidification is initiated) through

$$\mathbf{x} = \chi_{\kappa_r}(\mathbf{X}_{\kappa_r}, t). \quad (3.3)$$

We shall also assume that this motion is sufficiently smooth and invertible. The velocity of a particle in the reference state $\kappa_R(B)$ is defined as

$$\mathbf{v} = \frac{\partial \boldsymbol{\chi}_{\kappa_R}}{\partial t}. \quad (3.4)$$

As a result of the Eqs. (4.1), (4.2) and (4.3), for $t \geq t_i$, the velocity of the same particle, which occupied the position \mathbf{X}_{κ_r} is

$$\mathbf{v} = \frac{\partial \boldsymbol{\chi}_{\kappa_R}}{\partial t} = \frac{\partial \boldsymbol{\chi}_{\kappa_r}}{\partial t}. \quad (3.5)$$

The deformation gradients, \mathbf{F}_l , and the left and right Cauchy-Green stretch tensors \mathbf{B}_l and \mathbf{C}_l for $l = \kappa_R, \kappa_r$ are defined through

$$\mathbf{F}_l = \frac{\partial \boldsymbol{\chi}_l}{\partial \mathbf{X}_l}, \quad \mathbf{B}_l = \mathbf{F}_l \mathbf{F}_l^T, \quad \text{and} \quad \mathbf{C}_l = \mathbf{F}_l^T \mathbf{F}_l, \quad l = \kappa_R, \kappa_r. \quad (3.6)$$

The principal invariants of \mathbf{B}_l are

$$I_l = \text{tr}(\mathbf{B}_l), \quad II_l = \frac{1}{2} \left\{ [\text{tr}(\mathbf{B}_l)]^2 - \text{tr}(\mathbf{B}_l^2) \right\}, \quad \text{and} \quad III_l = \det(\mathbf{B}_l), \quad l = \kappa_R, \kappa_r. \quad (3.7)$$

We shall, for the sake of convenience, suppress B in the notation $\kappa_R(B)$, etc. Let $\kappa_{p_l(t)}$, $l = m, s$ be the stress-free states (natural configurations) associated with the current configuration κ_t of the body. The natural configurations $\kappa_{p_m(t)}$ and $\kappa_{p_s(t)}$ refer to the natural states associated with the melt and the solid respectively. For homogeneous deformations, $\mathbf{F}_{\kappa_{p_l(t)}}$, $l = m, s$ denote the deformation gradients between their respective natural configurations and the current configuration (see Figs. (9) and (10)).

In a manner similar to that of the Eq. (4.7), one can define the left and the right Cauchy-Green stretch tensors associated with the instantaneous response of the melt and the solid, from their natural configurations, respectively. The invariants of the

left Cauchy-Green stretch tensors are introduced through

$$\mathbf{I}_{\kappa_{p_l(t)}} = \text{tr}(\mathbf{B}_{\kappa_{p_l(t)}}), \quad \mathbf{II}_{\kappa_{p_l(t)}} = \text{tr}(\mathbf{B}_{\kappa_{p_l(t)}}^2), \quad \text{and} \quad \mathbf{III}_{\kappa_{p_l(t)}} = \text{tr}(\mathbf{B}_{\kappa_{p_l(t)}}^3), \quad l = m, s. \quad (3.8)$$

The mappings \mathbf{G}_m and \mathbf{G}_s are defined through

$$\mathbf{G}_m = \mathbf{F}_{\kappa_R \rightarrow \kappa_{p_m(t)}} = \mathbf{F}_{\kappa_{p_m(t)}}^{-1} \mathbf{F}_{\kappa_R} \quad \text{and} \quad \mathbf{G}_s = \mathbf{F}_{\kappa_r \rightarrow \kappa_{p_s(t)}} = \mathbf{F}_{\kappa_{p_s(t)}}^{-1} \mathbf{F}_{\kappa_r}, \quad (3.9)$$

where the mapping \mathbf{G}_s is defined for $t \geq t_i$.

The velocity gradients, \mathbf{L} and $\mathbf{L}_{\kappa_{p_l(t)}}$, $l = m, s$ are defined through

$$\begin{aligned} \mathbf{L} &:= \dot{\mathbf{F}}_{\kappa_R} \Big|_{\mathbf{X}_{\kappa_R} = \text{const.}} \mathbf{F}_{\kappa_R}^{-1} \quad \text{and} \\ \mathbf{L}_{\kappa_{p_l(t)}} &= \dot{\mathbf{G}}_l \mathbf{G}_l^{-1}, \quad l = m, s. \end{aligned} \quad (3.10)$$

It follows from the equation (4.11)₁ that

$$\mathbf{L} = \dot{\mathbf{F}}_{\kappa_r} \Big|_{\mathbf{X}_{\kappa_r} = \text{const.}} \mathbf{F}_{\kappa_r}^{-1}, \quad (3.11)$$

where the dot signifies the material time derivative.

The symmetric parts of \mathbf{L} and $\mathbf{L}_{\kappa_{p_l(t)}}$, $l = m, s$ are defined through

$$\mathbf{D} = \frac{1}{2}(\mathbf{L} + \mathbf{L}^T) \quad \text{and} \quad \mathbf{D}_{\kappa_{p_l(t)}} = \frac{1}{2}(\mathbf{L}_{\kappa_{p_l(t)}} + \mathbf{L}_{\kappa_{p_l(t)}}^T), \quad l = m, s. \quad (3.12)$$

It is also true that

$$\dot{\mathbf{B}}_{\kappa_r} - \mathbf{L} \mathbf{B}_{\kappa_r} - \mathbf{B}_{\kappa_r} \mathbf{L}^T = \mathbf{0}. \quad (3.13)$$

The upper convected Oldroyd derivative of $\mathbf{B}_{\kappa_{p_l(t)}}$, $l = m, s$, i.e., $\overset{\nabla}{\mathbf{B}}_{\kappa_{p_l(t)}}$, $l = m, s$, is defined through (see [58])

$$\overset{\nabla}{\mathbf{B}}_{\kappa_{p_l(t)}} = \dot{\mathbf{B}}_{\kappa_{p_l(t)}} - \mathbf{L} \mathbf{B}_{\kappa_{p_l(t)}} - \mathbf{B}_{\kappa_{p_l(t)}} \mathbf{L}^T = -2\mathbf{F}_{\kappa_{p_l(t)}} \mathbf{D}_{\kappa_{p_l(t)}} \mathbf{F}_{\kappa_{p_l(t)}}^T, \quad l = m, s. \quad (3.14)$$

As we shall require that the material, both in the molten state and solid state to be incompressible, we shall require that

$$\det(\mathbf{B}_{\kappa_{p_l(t)}}) = 1 \quad (\text{or } \text{tr}(\mathbf{L}_{\kappa_{p_l(t)}}) = 0) \quad \text{and } \text{tr}(\mathbf{L}) = 0, \quad l = m, s. \quad (3.15)$$

C. Modeling the melt

The melt is assumed to be isotropic with respect to the evolving configuration $\kappa_{p_m(t)}$ (see Fig. 9). We shall assume that the Helmholtz potential per unit mass is defined through:

$$\begin{aligned} \Psi_m(\theta, I_{\kappa_{p_m(t)}}, II_{\kappa_{p_m(t)}}) &= A^m + (B^m + c_2^m)(\theta - \theta_m) - c_1^m \frac{(\theta - \theta_m)^2}{2} \\ &- c_2^m \theta \ln \left(\frac{\theta}{\theta_m} \right) + \frac{\mu_1^m \theta}{2\rho\theta_m} (I_{\kappa_{p_m(t)}} - 3) + \frac{\mu_2^m \theta}{2\rho\theta_m} (II_{\kappa_{p_m(t)}} - 3), \end{aligned} \quad (3.16)$$

where θ_m , A^m , B^m , c_1^m , c_2^m , μ_1^m , and μ_2^m are the reference temperature and the material constants, respectively. Here, the material constants $\mu_1^m, \mu_2^m \geq 0$ with both constants not being equal to zero simultaneously. The density ρ , is assumed to be a constant. The specific Helmholtz potential, at constant temperature, is the same as that for a Mooney-Rivlin material, i.e., the melt's instantaneous elastic response is the same as that of a Mooney-Rivlin material.

The rate of entropy production (times temperature) due to mechanical working, per unit volume of the amorphous melt, is assumed to have the following form

$$\begin{aligned} \xi_m(\theta, \mathbf{B}_{\kappa_{p_m(t)}}, \mathbf{D}, \mathbf{D}_{\kappa_{p_m(t)}}) &= \{ 2\nu_1^m(\theta, \mathbf{B}_{\kappa_{p_m(t)}}) \mathbf{D}_{\kappa_{p_m(t)}} \cdot \mathbf{B}_{\kappa_{p_m(t)}} \mathbf{D}_{\kappa_{p_m(t)}} \\ &+ 2\nu_2^m(\theta, \mathbf{B}_{\kappa_{p_m(t)}}) \mathbf{D}_{\kappa_{p_m(t)}} \cdot \mathbf{B}_{\kappa_{p_m(t)}}^2 \mathbf{D}_{\kappa_{p_m(t)}} \}^\beta + 2\nu_3^m(\theta, \mathbf{B}_{\kappa_{p_m(t)}}) \mathbf{D} \cdot \mathbf{D} \\ &= \{ 2\nu_1^m(\theta, \mathbf{B}_{\kappa_{p_m(t)}}) \|\mathbf{D}_{\kappa_{p_m(t)}} \mathbf{V}_{\kappa_{p_m(t)}}\|^2 \\ &+ 2\nu_2^m(\theta, \mathbf{B}_{\kappa_{p_m(t)}}) \|\mathbf{D}_{\kappa_{p_m(t)}} \mathbf{B}_{\kappa_{p_m(t)}}\|^2 \}^\beta + 2\nu_3^m(\theta, \mathbf{B}_{\kappa_{p_m(t)}}) \|\mathbf{D}\|^2, \end{aligned} \quad (3.17)$$

where $\nu_l^m(\theta, \mathbf{B}_{\kappa_{pm}(t)})$, $l = 1, 2, 3$ are scalar and non-negative. The functions ν_l^m , $l = 1, 2, 3$ are material functions. Since each of the scalars multiplying the norms are non-negative, $\xi_m \geq 0$.

We introduce the second law of thermodynamics in the following form:

$$\mathbf{T}_m \cdot \mathbf{D} - \rho \dot{\Psi}_m - \rho \eta_m \dot{\theta} - \frac{\mathbf{q} \cdot \text{grad}(\theta)}{\theta} = \rho \theta \zeta_m = \hat{\xi}, \quad \hat{\xi} \geq 0, \quad (3.18)$$

where, ζ_m is the rate of entropy production per unit mass of the melt. The term $-\frac{\mathbf{q} \cdot \text{grad}(\theta)}{\theta^2}$ in the Eq. (4.18) is the rate of entropy production due to conduction; it is a non-negative quantity, which is positive when a temperature gradient exists and is zero when there is no temperature gradient. Furthermore, we shall assume $\hat{\xi}$ to be additive, i.e., we shall express

$$\hat{\xi} = \xi_c + \xi_m, \quad \xi_c, \xi_m \geq 0. \quad (3.19)$$

Here $\frac{\xi_c}{\theta}$ and $\frac{\xi_m}{\theta}$ are the rate of entropy production per unit volume associated with conduction and mechanical working respectively. We shall further require each of the entropy production mechanisms to be non-negative.

From (4.18) and (4.19), we arrive at the following two equations, namely,

$$\xi_c = -\frac{\mathbf{q} \cdot \text{grad}(\theta)}{\theta}, \quad (3.20)$$

and

$$\mathbf{T}_m \cdot \mathbf{D} - \rho \dot{\Psi}_m - \rho \eta_m \dot{\theta} = \xi_m. \quad (3.21)$$

Substituting the Eq. (4.16) into the reduced dissipation equation, i.e., the equation (4.17), and collecting like terms, we arrive at

$$\begin{aligned}
& \left[\mathbf{T}_m - \frac{\mu_1^m \theta}{\theta_m} \mathbf{B}_{\kappa_{pm}(t)} - \frac{2\mu_2^m \theta}{\theta_m} \mathbf{B}_{\kappa_{pm}(t)}^2 - 2\nu_3^m \mathbf{D} \right] \cdot \mathbf{D} \\
& - \rho \left[\frac{\partial \Psi_m}{\partial \theta} + \eta_m \right] \dot{\theta} + \left[\frac{\mu_1^m \theta}{\theta_m} \mathbf{B}_{\kappa_{pm}(t)} + \frac{2\mu_2^m \theta}{\theta_m} \mathbf{B}_{\kappa_{pm}(t)}^2 \right] \cdot \mathbf{D}_{\kappa_{pm}(t)} \\
& = \xi_m - 2\nu_3^m \mathbf{D} \cdot \mathbf{D}.
\end{aligned} \tag{3.22}$$

One way to satisfy the above equation, is to assume that the equations (4.23) and (4.24) hold:

$$\mathbf{T}_m = -p\mathbf{I} + \frac{\mu_1^m \theta}{\theta_m} \mathbf{B}_{\kappa_{pm}(t)} + \frac{2\mu_2^m \theta}{\theta_m} \mathbf{B}_{\kappa_{pm}(t)}^2 + 2\nu_3^m \mathbf{D}, \tag{3.23}$$

where p is the Lagrange multiplier, due to the constraint of incompressibility. We mentioned earlier that Ψ_m corresponds to the stored energy of a Mooney-Rivlin material. However, Eq. (4.23) is not the constitutive equation for a Mooney-Rivlin material unless ν_3^m is zero. The reason for this stems from our assumption that the viscoelastic body is a mixture of an elastic solid and a viscous fluid, and this is reflected in assumption for the Helmholtz potential and the rate of dissipation function. We have supposed that at each point of the body we have a mixture of a viscoelastic fluid capable of instantaneous elasticity and a dissipative linearly viscous fluid. Though the material stores energy like a Mooney-Rivlin material, the stress is not that of a Mooney-Rivlin material. As it is a mixture of an elastic solid and a viscous fluid, the stress also has a contribution from the viscous fluid component. We note that on setting $\mu_2^m = \nu_3^m = 0$, the instantaneous elastic response is found to be that of a neo-Hookean material with the shear modulus being proportional to the absolute temperature (Gaussian network, see Treloar [81]).

We also suppose that

$$\begin{aligned} \eta_m &= -\frac{\partial \Psi_m}{\partial \theta} = -B^m + c_1^m(\theta - \theta_m) + c_2^m \ln\left(\frac{\theta}{\theta_m}\right) \\ &\quad - \frac{\mu_1^m}{2\rho\theta_m}(I_{\kappa_{pm}(t)} - 3) - \frac{\mu_2^m}{2\rho\theta_m}(II_{\kappa_{pm}(t)} - 3). \end{aligned} \quad (3.24)$$

The entropy of the material is assumed to diminish as the material is deformed as the molecules of the polymer align themselves along the direction of deformation. As a result of Eqs. (4.23) and (4.24), Eq. (4.22) becomes

$$\begin{aligned} &\left[\frac{\mu_1^m \theta}{\theta_m} \mathbf{B}_{\kappa_{pm}(t)} + \frac{2\mu_2^m \theta}{\theta_m} \mathbf{B}_{\kappa_{pm}(t)}^2 \right] \cdot \mathbf{D}_{\kappa_{pm}(t)} = \xi_m - 2\nu_3^m \mathbf{D} \cdot \mathbf{D} \\ &= \left\{ 2\nu_1^m \mathbf{D}_{\kappa_{pm}(t)} \cdot \mathbf{B}_{\kappa_{pm}(t)} \mathbf{D}_{\kappa_{pm}(t)} + 2\nu_2^m \mathbf{D}_{\kappa_{pm}(t)} \cdot \mathbf{B}_{\kappa_{pm}(t)}^2 \mathbf{D}_{\kappa_{pm}(t)} \right\}^\beta. \end{aligned} \quad (3.25)$$

The Helmholtz potential is defined through

$$\Psi_m = \epsilon_m - \eta_m \theta, \quad (3.26)$$

where ϵ_m and η_m are the internal energy and the entropy per unit mass of the material. On using Eqs. (4.24) and (4.26), we find that the internal energy of the material is given by

$$\epsilon_m = A^m - B^m \theta_m + \frac{c_1^m}{2}(\theta^2 - \theta_m^2) + c_2^m(\theta - \theta_m). \quad (3.27)$$

We notice that the above equation is only a function of the temperature, which is consistent with the melt being entropic in nature. Further, the internal energy function is strictly convex if $c_1^m > 0$.

The specific heat of the melt, C^m , is defined as

$$C^m = \frac{\partial \epsilon_m}{\partial \theta} = -\theta \frac{\partial^2 \Psi_m}{\partial \theta^2} = c_1^m \theta + c_2^m > 0, \quad \forall \theta \text{ until } \phi = 0, \quad (3.28)$$

where ϕ is given by the Eq. (3.61); the model for the melt is valid until $\phi = 0$. For a given mass of the material, one would expect the internal energy of the material to increase when the energy is supplied in the thermal form. Therefore, we require C^m to be positive; this restriction on the constants ensures that the convex function ϵ_m is restricted to the region of positive slope only. If $c_1^m < 0$, whatever the value of c_2^m , a sufficiently high temperature (where the material exists in a melt-like state) can be found, which violates the above inequality. Thus c_1^m has to be non-negative; both c_1^m and c_2^m are not zero simultaneously. The specific heat of the material is linear in θ as indicated by the differential scanning calorimetry (DSC) studies of several polymers (see Brandrup and Immergut [5]).

Since the melt is assumed to be incompressible, we require that

$$\text{tr} \mathbf{D} \kappa_{pm(t)} = 0. \quad (3.29)$$

To obtain the evolution equation, let us proceed with the maximization of ξ_m subject to the constraints, i.e., Eqs. (4.25) and (4.29). Using the method of Lagrange multipliers, the augmented rate of entropy production (due to mechanical working) function Φ_m is defined through

$$\Phi_m = \xi_m + \lambda_1^m \left[\xi_m - 2\nu_3^m \mathbf{D} \cdot \mathbf{D} - \left(\mathbf{T}_m - 2\nu_3^m \mathbf{D} \right) \cdot \mathbf{D} \kappa_{pm(t)} \right] + \lambda_2^m \text{tr} \mathbf{D} \kappa_{pm(t)}, \quad (3.30)$$

where λ_1^m and λ_2^m are the Lagrange multipliers. It follows that

$$\begin{aligned}
\frac{\partial \Phi_m}{\partial \mathbf{D}_{\kappa_{pm}(t)}} &= 0 \Rightarrow \\
\left(\frac{1 + \lambda_1^m}{\lambda_1^m} \right) \beta &\left\{ 2\nu_1^m \mathbf{D}_{\kappa_{pm}(t)} \cdot \mathbf{B}_{\kappa_{pm}(t)} \mathbf{D}_{\kappa_{pm}(t)} + 2\nu_2^m \mathbf{D}_{\kappa_{pm}(t)} \cdot \mathbf{B}_{\kappa_{pm}(t)}^2 \mathbf{D}_{\kappa_{pm}(t)} \right\}^{\beta-1} \\
&\left[2\nu_1^m \left(\mathbf{B}_{\kappa_{pm}(t)} \mathbf{D}_{\kappa_{pm}(t)} + \mathbf{D}_{\kappa_{pm}(t)} \mathbf{B}_{\kappa_{pm}(t)} \right) + 2\nu_2^m \left(\mathbf{B}_{\kappa_{pm}(t)}^2 \mathbf{D}_{\kappa_{pm}(t)} + \mathbf{D}_{\kappa_{pm}(t)} \mathbf{B}_{\kappa_{pm}(t)}^2 \right) \right] \\
&= - \left(p + \frac{\lambda_2^m}{\lambda_1^m} \right) \mathbf{I} + \frac{\mu_1^m \theta}{\theta_m} \mathbf{B}_{\kappa_{pm}(t)} + \frac{2\mu_2^m \theta}{\theta_m} \mathbf{B}_{\kappa_{pm}(t)}^2. \tag{3.31}
\end{aligned}$$

We can show that the eigen vectors of the tensors $\mathbf{B}_{\kappa_{pm}(t)}$ and $\mathbf{D}_{\kappa_{pm}(t)}$ are the same and hence they commute. Taking the inner product of the above equation with $\mathbf{D}_{\kappa_{pm}(t)}$ and using the fact that the tensors $\mathbf{B}_{\kappa_{pm}(t)}$ and $\mathbf{D}_{\kappa_{pm}(t)}$ commute, and the Eqs. (4.25) and (4.29), $\frac{1 + \lambda_1^m}{\lambda_1^m}$ is determined to be $\frac{1}{2\beta}$. Substituting $\frac{1 + \lambda_1^m}{\lambda_1^m} = \frac{1}{2\beta}$ in the Eq. (3.31), rewriting this equation after taking advantage of commutativity of the tensors, and premultiplying by $\mathbf{B}_{\kappa_{pm}(t)}^{-1}$, one arrives at

$$\begin{aligned}
&\left\{ 2\nu_1^m \mathbf{D}_{\kappa_{pm}(t)} \cdot \mathbf{B}_{\kappa_{pm}(t)} \mathbf{D}_{\kappa_{pm}(t)} + 2\nu_2^m \mathbf{D}_{\kappa_{pm}(t)} \cdot \mathbf{B}_{\kappa_{pm}(t)}^2 \mathbf{D}_{\kappa_{pm}(t)} \right\}^{\beta-1} \left(2\nu_1^m \mathbf{D}_{\kappa_{pm}(t)} + \right. \\
&\left. 2\nu_2^m \mathbf{B}_{\kappa_{pm}(t)} \mathbf{D}_{\kappa_{pm}(t)} \right) = - \left(p + \frac{\lambda_2^m}{\lambda_1^m} \right) \mathbf{B}_{\kappa_{pm}(t)}^{-1} + \frac{\mu_1^m \theta}{\theta_m} \mathbf{I} + \frac{2\mu_2^m \theta}{\theta_m} \mathbf{B}_{\kappa_{pm}(t)}. \tag{3.32}
\end{aligned}$$

Using the trace operator on both the sides of the Eq. (3.32) and using the Eqs. (4.14) and (4.29) results in

$$\begin{aligned}
\left(p + \frac{\lambda_2^m}{\lambda_1^m} \right) \text{tr} \mathbf{B}_{\kappa_{pm}(t)}^{-1} &= \nu_2^m \text{tr} \overset{\nabla}{\mathbf{B}}_{\kappa_{pm}(t)} \left\{ 2\nu_1^m \mathbf{D}_{\kappa_{pm}(t)} \cdot \mathbf{B}_{\kappa_{pm}(t)} \mathbf{D}_{\kappa_{pm}(t)} \right. \\
&\left. + 2\nu_2^m \mathbf{D}_{\kappa_{pm}(t)} \cdot \mathbf{B}_{\kappa_{pm}(t)}^2 \mathbf{D}_{\kappa_{pm}(t)} \right\}^{\beta-1} + \frac{3\mu_1^m \theta}{\theta_m} + \frac{2\mu_2^m \theta}{\theta_m} \text{tr} \mathbf{B}_{\kappa_{pm}(t)}. \tag{3.33}
\end{aligned}$$

Then, on using the Eq. (4.25), we have

$$\begin{aligned}
& 2\nu_1^m \mathbf{D}_{\kappa_{pm}(t)} \cdot \mathbf{B}_{\kappa_{pm}(t)} \mathbf{D}_{\kappa_{pm}(t)} + 2\nu_2^m \mathbf{D}_{\kappa_{pm}(t)} \cdot \mathbf{B}_{\kappa_{pm}(t)}^2 \mathbf{D}_{\kappa_{pm}(t)} \\
&= \left\{ \frac{\mu_1^m \theta}{\theta_m} \mathbf{B}_{\kappa_{pm}(t)} \cdot \mathbf{D}_{\kappa_{pm}(t)} + \frac{2\mu_2^m \theta}{\theta_m} \mathbf{B}_{\kappa_{pm}(t)}^2 \cdot \mathbf{D}_{\kappa_{pm}(t)} \right\}^{1/\beta}. \tag{3.34}
\end{aligned}$$

Using the trace operator on either side of Eq. (4.14) and pre (or post) multiplying by the tensor $\mathbf{B}_{\kappa_{pm}(t)}$ on both sides of the same equation as necessary, followed by taking the inner product with the identity tensor, one arrives at the following two results:

$$\text{tr } \overset{\nabla}{\mathbf{B}}_{\kappa_{pm}(t)} = -2\text{tr}(\mathbf{B}_{\kappa_{pm}(t)} \mathbf{D}_{\kappa_{pm}(t)}) \text{ and } \text{tr}(\mathbf{B}_{\kappa_{pm}(t)} \overset{\nabla}{\mathbf{B}}_{\kappa_{pm}(t)}) = -2\text{tr}(\mathbf{B}_{\kappa_{pm}(t)}^2 \mathbf{D}_{\kappa_{pm}(t)}). \tag{3.35}$$

Premultiplying Eq. (3.31) by $\mathbf{V}_{\kappa_{pm}(t)}^{-1}$ and postmultiplying it by $\mathbf{V}_{\kappa_{pm}(t)}$, using the Eq. (4.14) with $\mathbf{F}_{\kappa_{pm}(t)} = \mathbf{V}_{\kappa_{pm}(t)}$ (suitably rotated $\kappa_{pm}(t)$), substituting the value for Lagrange multipliers, i.e., $\frac{1 + \lambda_1^m}{\lambda_1^m} = \frac{1}{2\beta}$ and $p + \frac{\lambda_2^m}{\lambda_1^m}$ from the Eq. (3.33), using Eqs. (3.34) and (3.35) in the Eq. (3.31), and the fact that the tensors $\mathbf{B}_{\kappa_{pm}(t)}$ and $\mathbf{D}_{\kappa_{pm}(t)}$ commute, Eq. (3.31) reduces to

$$\begin{aligned}
& \left\{ \frac{\mu_1^m \theta}{2\theta_m} \text{tr}(-\overset{\nabla}{\mathbf{B}}_{\kappa_{pm}(t)}) + \frac{\mu_2^m \theta}{\theta_m} \text{tr}(-\mathbf{B}_{\kappa_{pm}(t)} \overset{\nabla}{\mathbf{B}}_{\kappa_{pm}(t)}) \right\}^{(\beta-1)/\beta} \left\{ \nu_2^m \frac{\text{tr } \overset{\nabla}{\mathbf{B}}_{\kappa_{pm}(t)}}{\text{tr } \mathbf{B}_{\kappa_{pm}(t)}^{-1}} \mathbf{I} \right. \\
& \left. - (\nu_1^m \mathbf{I} + \nu_2^m \mathbf{B}_{\kappa_{pm}(t)}) \overset{\nabla}{\mathbf{B}}_{\kappa_{pm}(t)} \right\} = \frac{\mu_1^m \theta}{\theta_m} \left(\mathbf{B}_{\kappa_{pm}(t)} - \frac{3}{\text{tr } \mathbf{B}_{\kappa_{pm}(t)}^{-1}} \mathbf{I} \right) \\
& + \frac{2\mu_2^m \theta}{\theta_m} \left(\mathbf{B}_{\kappa_{pm}(t)}^2 - \frac{\text{tr } \mathbf{B}}{\text{tr } \mathbf{B}_{\kappa_{pm}(t)}^{-1}} \mathbf{I} \right), \tag{3.36}
\end{aligned}$$

which is the evolution equation for the natural configuration.

The above equation is an implicit differential equation of the form $\mathbf{f}(\overset{\nabla}{\mathbf{B}}_{\kappa_{pm}(t)}, \mathbf{B}_{\kappa_{pm}(t)}) = \mathbf{0}$ and may be solved by converting it into a differential algebraic system of the following form: $\overset{\nabla}{\mathbf{B}}_{\kappa_{pm}(t)} = \mathbf{A}$ and $\mathbf{f}(\mathbf{A}, \mathbf{B}_{\kappa_{pm}(t)}) = \mathbf{0}$. The last equation of the system, i.e., $\mathbf{f}(\mathbf{A}, \mathbf{B}_{\kappa_{pm}(t)}) = \mathbf{0}$ is a tensor valued non-linear equation, for a fixed $\mathbf{B}_{\kappa_{pm}(t)}$, and may have several roots, which are related to the extrema $\mathbf{D}_{\kappa_{pm}(t)}^0$ of the function

ξ^m subject to the constraints (4.25) and (4.29). If one invokes the maximization of dissipation assumption, the tensor $\mathbf{D}_{\kappa_{pm}(t)}^0$, among all local maxima (if there are more than one), the one with the highest rate of dissipation is chosen by inspection. On setting $\beta = 1$, $\nu_2^m = \nu_3^m = 0$, and $\mu_2^m = 0$ in the Eq. (3.36), we recover the evolution equation for the natural configuration for the generalized Maxwell model (see Rajagopal and Srinivasa [58]). Here, the shear modulus is proportional to the absolute temperature and is similar to that of Gaussian statistical theory (see Treloar [81]); if $\nu_3^m \neq 0$, we recover the generalized Oldroyd model. The assumption $\nu_2^m = \nu_3^m = 0$, and $\mu_2^m = 0$ with $\alpha := (2\nu_1^m)^\beta$ and $n := (\beta - 1)/(1 - 2\beta)$ leads to a power law model (see Srinivasa [76]). Further, if $\beta = 1$ and $\nu_3^m = 0$, we obtain a model with an instantaneous response like that of a Mooney material with the evolution equation that is explicit. Thus, the power law model represented through the Eqs. (4.23) and (3.36) can be viewed as a generalization of all the special models mentioned above.

1. An application of the melt model

To test the efficacy of the model developed for the polymeric melt, we shall use the model for the melt to describe the flow of a polymeric melt in an extensional rheometer. The flow in such an apparatus can be described in the following manner. Let us consider a rectangular sample of about $60 \times 7 \times 2$ mm³ that is carefully prepared by compression molding. Suppose that each end of the sample is wedged in between two pairs of metal belt rollers with the tips of each pair (separated by 50 mm) acting as grips. Further suppose that the temperature inside the elongational rheometer housing can be controlled to within $\pm 0.2^\circ C$, maximum temperature being about $350^\circ C$. Before the sample is inserted into the rheometer housing, a grid pattern of SiC powder is laid on the top of the sample. The sagging of the sample, at high temperature, is prevented by a cushion of inert gas blowing from the system

supporting the sample located below the sample. A constant 'strain' rate ($0.001 - 1s^{-1}$) can be obtained by rotating the metal belts at a constant speed in an opposing manner between the two pairs. The force needed to achieve constant strain rate can also be measured. A video camera is used to record the grid pattern that is used to determine the true 'strain' rate. The homogeneity of the deformation can be checked by observing the grid patterns as a function of time. We shall consider the situation when the strain rate is a constant and homogeneous throughout the deformation process (for more details regarding the rheometer, the reader is referred to Meissner and Hostetler [40]).

By rotating the metal belts at a constant speed, a constant strain rate data can be ensured. The force is measured using a suitable transducer. One can also perform a constant strain rate test followed by a stress relaxation measurement. This experiment can be performed by stopping the metal belt rollers, which act as grips by firmly holding the sample, and measuring the force as the sample relaxes (see Meissner [39]).

In case of a homogeneous uniaxial elongation, the motion in rectangular co-ordinates is given by

$$x = \lambda(t)X, \quad y = \frac{1}{\sqrt{\lambda(t)}}Y, \quad z = \frac{1}{\sqrt{\lambda(t)}}Z. \quad (3.37)$$

The components of velocity gradient tensor are

$$[\mathbf{L}] = [\mathbf{D}] = [\dot{\mathbf{F}}_{\kappa_R} \mathbf{F}_{\kappa_R}^{-1}] = \text{diag} \left\{ \frac{\dot{\lambda}(t)}{\lambda(t)}, -\frac{\dot{\lambda}(t)}{2\lambda(t)}, -\frac{\dot{\lambda}(t)}{2\lambda(t)} \right\}. \quad (3.38)$$

We shall assume that the components of the tensor $\mathbf{B}_{\kappa_{pm}(t)}$ have the following form:

$$[\mathbf{B}_{\kappa_{pm}(t)}] = \text{diag} \left\{ B(t), \frac{1}{\sqrt{B(t)}}, \frac{1}{\sqrt{B(t)}} \right\}, \quad (3.39)$$

which is tantamount to assuming the stress-free state via a deformation of the form of the equation (3.37). Since the lateral surfaces are traction free, using Eq. (4.23), the stress component along x -direction is

$$[\mathbf{T}_m]_{xx} = T_{11} = \bar{\mu}_1^m \left(\frac{B^{3/2}(t) - 1}{\sqrt{B(t)}} \right) + 2\bar{\mu}_2^m \left(\frac{B^3(t) - 1}{B(t)} \right) + 3\nu_3^m \dot{\epsilon}_0(t), \quad (3.40)$$

where $\dot{\epsilon}_0(t) = \dot{\lambda}(t)/\lambda(t)$.

Substituting Eqs. (3.38) and (3.39) in the Eq. (3.36), using the Eq. (4.14), and suppressing the argument t , the evolution equation becomes

$$2\dot{\epsilon}_0 B - \dot{B} = 2B \left\{ \frac{\left\{ \bar{\mu}_1^m \left(\frac{B^{3/2} - 1}{\sqrt{B}} \right) + 2\bar{\mu}_2^m \left(\frac{B^3 - 1}{B} \right) \right\} 2^\beta}{\left\{ 2(2\nu_1^m B + 2\nu_2^m B^2) + \frac{2\nu_1^m}{\sqrt{B}} + \frac{2\nu_2^m}{B} \right\}^\beta} \right\}^{1/(2\beta-1)}. \quad (3.41)$$

For the choice of the components of $\mathbf{B}_{\kappa_{pm}(t)}$ given by the Eq. (3.39), the components of the tensor $\mathbf{D}_{\kappa_{pm}(t)}$, using Eq. (4.14) with $\mathbf{F}_{\kappa_{pm}(t)} = \mathbf{V}_{\kappa_{pm}(t)}$, are

$$[\mathbf{D}_{\kappa_{pm}(t)}^0] = \text{diag} \left\{ \frac{2\dot{\epsilon}_0 B - \dot{B}}{2B}, -\frac{(2\dot{\epsilon}_0 B - \dot{B})}{4B}, -\frac{(2\dot{\epsilon}_0 B - \dot{B})}{4B} \right\}, \quad (3.42)$$

where $\mathbf{D}_{\kappa_{pm}(t)}^0$ is the extremum and $2\dot{\epsilon}_0 B - \dot{B}$ is given by the Eq. (3.41). Now, we shall determine the nature of the extremum. Since the tensor $\mathbf{D}_{\kappa_{pm}(t)}$ can always be diagonalized, on using the Eqs. (3.38) and (3.39), Eq. (4.17) becomes

$$\bar{\xi}_m = \left\{ (2\nu_1^m B + 2\nu_2^m B^2) d_1^2 + \left(\frac{2\nu_1^m}{\sqrt{B}} + \frac{2\nu_2^m}{B} \right) [d_2^2 + (d_1 + d_2)^2] \right\}^\beta + 3\nu_3^m (\dot{\epsilon}_0)^2, \quad (3.43)$$

where the components of tensor $\mathbf{D}_{\kappa_{pm}(t)}$ are $\text{diag}\{d_1, d_2, -(d_1 + d_2)\}$ (automatically satisfies incompressibility constraint). The constraint (4.25) becomes

$$g = \left\{ \bar{\mu}_1^m \left(\frac{B^{3/2}(t) - 1}{\sqrt{B(t)}} \right) + 2\bar{\mu}_2^m \left(\frac{B^3(t) - 1}{B(t)} \right) \right\} d_1 - \bar{\xi}_m = 0. \quad (3.44)$$

The augmented function is $\hat{\phi}(d_1, d_2, \lambda) = \bar{\xi}_m + \lambda g$, where λ is the Lagrange multiplier. By using the method of Lagrange multipliers, as expected, the extremum $\{d_1^0, d_2^0\}$ is given by the first two components of the Eq. (3.42) and $\frac{\lambda - 1}{\lambda} = \frac{1}{2\beta}$. For a strong local maximum, the following condition needs to be satisfied (see pp. 220-223 of [48])

$$\left\{ - \left(\frac{\partial g}{\partial d_2} \right)^2 \frac{\partial^2 \hat{\phi}}{\partial d_1^2} + 2 \left(\frac{\partial g}{\partial d_1} \right) \left(\frac{\partial g}{\partial d_2} \right) \frac{\partial^2 \hat{\phi}}{\partial d_1 \partial d_2} - \left(\frac{\partial g}{\partial d_1} \right)^2 \frac{\partial^2 \hat{\phi}}{\partial d_2^2} \right\}_{\{d_1^0, d_2^0, \lambda\}} > 0. \quad (3.45)$$

Since ν_1^m and ν_2^m are non-negative (both are not zero simultaneously) and $B > 0$, for arbitrarily fixed B, the above condition is satisfied as long as $\beta > 0.5$ or $\beta < 0$. If $\beta < 0$, then from Eq. (3.43) it is clear that the rate of dissipation will decrease with increasing d_1 and d_2 , which is in contradiction to what one would expect. Thus, we shall require that $\beta > 0.5$. Further, for a sufficiently smooth function $\bar{\xi}_m$, the function $\bar{\xi}_m$ loses its convexity (in \mathbb{R}^2) if $\beta < 0.5$ (see pp. 45-47 and 173 of Panik [48]). Further, $\{d_1^0, d_2^0\}$ is the only non-trivial extremum. Thus, the maximum rate of dissipation criterion is satisfied.

In the Figs. 11-13, the experiments were conducted at a constant strain rate ($\dot{\epsilon}_0$), at some fixed temperature, and the force required is measured. In the Fig. 13, the stress is calculated, neglecting inertial effects, by dividing the force by the current area ($A_0 \exp(-\dot{\epsilon}_0 t)$, where A_0 is initial area). Strain rate tests were performed at three different rates until the Hencky strain ($\ln(\lambda)$, where λ is the stretch) of one unit is achieved for polystyrene at $170^\circ C$. Fig. 14 indicates the relaxation data after the cessation of the constant rate experiments depicted in Fig. 13. In all the figures the predictions of the theory and the experiment have been plotted.

The evolution equation (3.41) was solved numerically using a 4th order Runge-Kutta scheme using Matlab, with the initial condition $B = 1$. For the simulation of the relaxation response, the value of B obtained at the instant of cessation is used as the initial condition. Further, since there is no deformation during the relaxation process,

the components of the tensor \mathbf{L} are zero; the area remains constant and is equal to the area at the end of the constant strain rate test. The stress is calculated using the Eq. (3.40) and the force is computed as $T_{11}A_0 \exp(-\dot{\epsilon}_0 t)$.

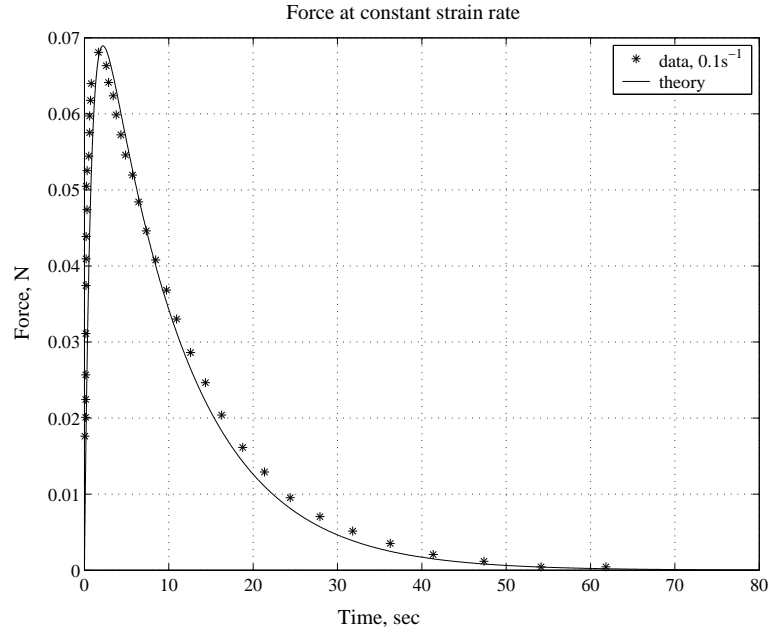


Fig. 11. The data was obtained at a constant strain rate of $0.1s^{-1}$ at $150^{\circ}C$ for Linear Low Density Polyethylene (LLDPE). The initial cross sectional area, A_0 , is $17.19mm^2$ (see [40]). The material constants used are $\beta = 0.97$, $\bar{\mu}_1^m = 20000Pa$, $\left\{ \frac{\bar{\mu}_1^m}{(\nu_1^m)^\beta} \right\}^{1/(2\beta-1)} = 1.3717 s^{-1}$, and $\bar{\mu}_2^m = \nu_2^m = \nu_3^m = 0$.

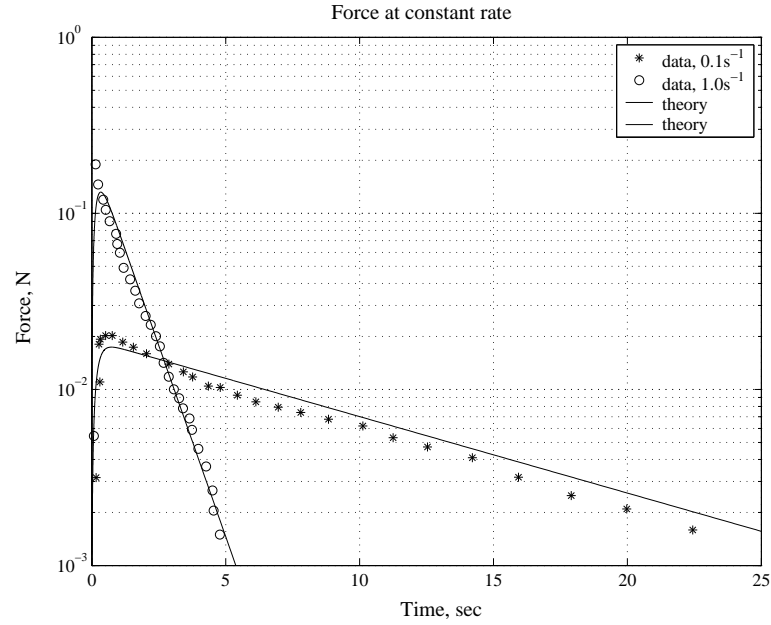


Fig. 12. The plot indicates the measured force at two different strain rates at $250^{\circ}C$ for polyamide. The material constants picked were $\beta = 0.95$, $\bar{\mu}_1^m = 18000\text{Pa}$, $\left\{ \frac{\bar{\mu}_1^m}{(\nu_1^m)^\beta} \right\}^{1/(2\beta-1)} = 7.4458 \text{ s}^{-1}$, and $\bar{\mu}_2^m = \nu_2^m = \nu_3^m = 0$.

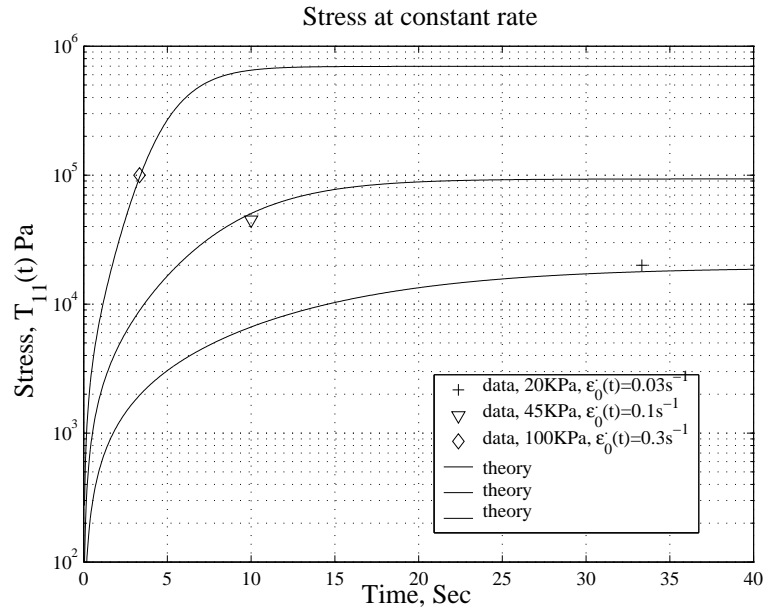


Fig. 13. The plot shows the stress at constant strain rate for polystyrene at $170^{\circ}C$. The material constants are $\beta = 0.8$, $\bar{\mu}_1^m = 400\text{Pa}$, $\bar{\mu}_2^m = 1400\text{Pa}$, $\left\{ \frac{\bar{\mu}_1^m}{(\nu_1^m)^\beta} \right\}^{1/(2\beta-1)} = 8.8039 \times 10^{-4} \text{ s}^{-1}$, and $\frac{\nu_1^m}{\nu_2^m} = 4.375$.

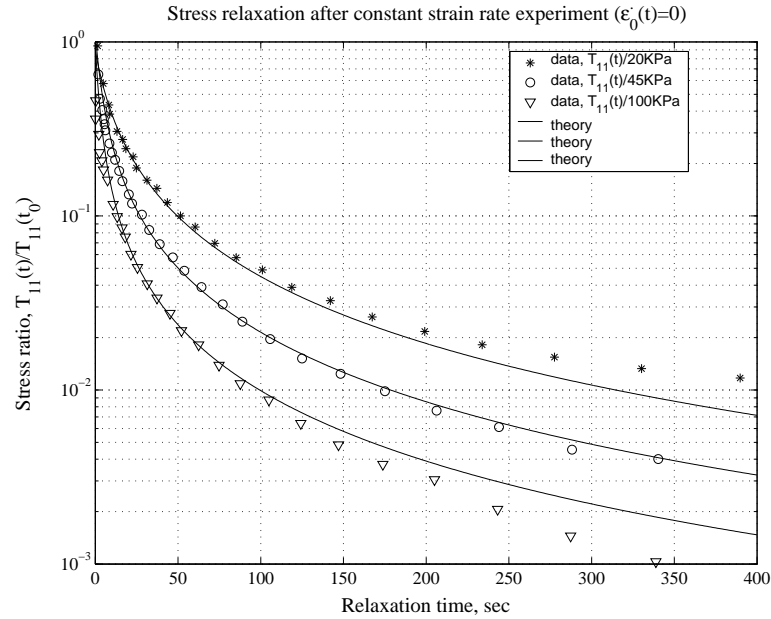


Fig. 14. The above figure shows the comparison of the predictions and the data during constant length relaxation of the sample. The initial conditions are $B(t_0) = 2.5465, 4.2075, \text{ and } 5.7865$; the value of $B(t_0)$'s obtained at the end of the constant strain rate experiment in the Fig. 13. The material constants are the same as that used to obtain Fig. 13.

The numerical results compare very favorably with the experiments. In the Figs. 11 and 12 good agreement was achieved using the power law type of model discussed in Srinivasa [76]. It is of course necessary to further compare the predictions of the model with these values of the material constants, under other experimental conditions to ascertain the appropriateness of the model as well as the values for the material moduli that have been used.

D. Modeling the mixture

The Helmholtz potential per unit mass of the mixture is defined as

$$\Psi(\theta, I_{\kappa_{pm}(t)}, II_{\kappa_{pm}(t)}, I_{\kappa_{ps}(t)}, I_{\kappa_r}, \alpha) = \alpha \Psi_m(\theta, I_{\kappa_{pm}(t)}, II_{\kappa_{pm}(t)}) + (1 - \alpha) \Psi_s(\theta, I_{\kappa_{ps}(t)}, I_{\kappa_r}), \quad (3.46)$$

where α is the mass fraction of the melt.

The Helmholtz potential associated with the solid is defined through

$$\begin{aligned} \Psi_s(\theta, I_{\kappa_{ps}(t)}, I_{\kappa_r}) &= A^s + (B^s + c_2^s)(\theta - \theta_s) - c_1^s \frac{(\theta - \theta_s)^2}{2} \\ &- c_2^s \theta \ln \left(\frac{\theta}{\theta_s} \right) + \frac{\mu_1^s}{2\rho} (I_{\kappa_{ps}(t)} - 3) + \frac{\mu_2^s}{2\rho} (I_{\kappa_r} - 3), \end{aligned} \quad (3.47)$$

where θ_s denotes the reference temperature and A^s , B^s , c_1^s , c_2^s , μ_1^s , and μ_2^s are material constants, the last two constants representing the shear modulus is assumed to be non-negative. In the above equation, $\kappa_r(B)$ is the configuration at which the melt starts to solidify (see Fig. 10) and $\kappa_{ps}(t)$ denotes the evolving natural configuration associated with the viscoelastic solid that has been formed. The material is assumed to be isotropic with respect to these configurations. For any fixed configuration, the contribution of the last term in the Eq. (3.47) is fixed, while that of the penultimate term will be given by a rate equation similar to that for the melt and hence may change with time.

The rate of entropy production due to mechanical (times temperature) working per unit volume of the mixture is defined through

$$\xi(\theta, \mathbf{B}_{\kappa_{pm}(t)}, \mathbf{D}_{\kappa_{pm}(t)}, \mathbf{D}, \mathbf{B}_{\kappa_{ps}(t)}, \mathbf{D}_{\kappa_{ps}(t)}, \alpha) = \alpha \xi_m + (1 - \alpha) \xi_s, \quad (3.48)$$

where ξ_s , the rate of entropy production (times temperature) due to mechanical working of the solid, which is defined through

$$\xi_s(\theta, \mathbf{B}_{\kappa_{ps}(t)}, \mathbf{D}_{\kappa_{ps}(t)}) = 2\nu^s(\theta, \mathbf{B}_{\kappa_{ps}(t)})\mathbf{D}_{\kappa_{ps}(t)} \cdot \mathbf{B}_{\kappa_{ps}(t)} \mathbf{D}_{\kappa_{ps}(t)}. \quad (3.49)$$

In the above equation, the rate of dissipation is weighted by the mass fraction. The other entropy producing mechanisms in the mixture are due to conduction and phase change. The total entropy production is assumed to be additive, i.e., $\hat{\xi} = \xi_c + \xi + \xi_p$, where $\frac{\xi_p}{\theta}$ is the rate of entropy production per unit volume of the mixture. Further, each of the entropy producing mechanisms are assumed to be non-negative. The reduced dissipation equation, for the mixture, reads as

$$\mathbf{T} \cdot \mathbf{D} - \rho\dot{\Psi} - \rho\eta\dot{\theta} = \xi + \xi_p, \quad \xi, \xi_p \geq 0. \quad (3.50)$$

Substituting the Eqs. (3.46) and (3.48) in the Eq. (3.50), one arrives at

$$\begin{aligned} & \left[\mathbf{T} - \alpha \left(\frac{\mu_1^m \theta}{\theta_m} \mathbf{B}_{\kappa_{pm}(t)} + \frac{2\mu_2^m \theta}{\theta_m} \mathbf{B}_{\kappa_{pm}(t)}^2 + 2\nu_3^m \mathbf{D} \right) \right. \\ & \left. - (1 - \alpha) \left(\mu_1^s \mathbf{B}_{\kappa_{ps}(t)} + \mu_2^s \mathbf{B}_{\kappa_r} \right) \right] \cdot \mathbf{D} - \rho \left[-\alpha\eta_m - (1 - \alpha)\eta_s + \eta \right] \dot{\theta} \\ & + \alpha \left[\frac{\mu_1^m \theta}{\theta_m} \mathbf{B}_{\kappa_{pm}(t)} + \frac{2\mu_2^m \theta}{\theta_m} \mathbf{B}_{\kappa_{pm}(t)}^2 \right] \cdot \mathbf{D}_{\kappa_{pm}(t)} + (1 - \alpha) \mu_1^s \mathbf{B}_{\kappa_{ps}(t)} \cdot \mathbf{D}_{\kappa_{ps}(t)} \\ & - \rho(\Psi_m - \Psi_s) \dot{\alpha} = \alpha \left[\xi_m - 2\nu_3^m \mathbf{D} \cdot \mathbf{D} \right] + (1 - \alpha)\xi_s + \xi_p, \end{aligned} \quad (3.51)$$

where the entropy of the solid constituent of the mixture, i.e., η_s is

$$\eta_s = -B^s + c_1^s(\theta - \theta_s) + c_2^s \ln \left(\frac{\theta}{\theta_s} \right), \quad (3.52)$$

and

$$\begin{aligned} \xi_p(\alpha, \dot{\alpha}) = & -\{A(1 - \alpha^m) + B(1 - \alpha^n)\}\dot{\alpha}, \quad 0 < m < 1 \text{ (or } 0 < n < 1) \text{ and} \\ & n \geq 0 \text{ (or } m \geq 0), \end{aligned} \quad (3.53)$$

where A and B are positive constants. We shall require that only those processes with $\dot{\alpha} \leq 0$ are allowed. In other words, the solid is not allowed to re convert into the melt phase. Since the constants A , B , m , and n are non-negative and $\alpha \in [0, 1]$, ξ_p is non-negative. The form of the function ξ_p also satisfies $\xi_p(\alpha, 0) = 0$. One would also expect that $\xi_p \rightarrow 0$ at the beginning and the end of the transitional regime; as $\alpha \rightarrow 1$, $\xi_p \rightarrow 0$. We will show in this section that $\dot{\alpha} \rightarrow 0$ as $\alpha \rightarrow 0$ thereby satisfying this supposition. The functional form of the function ξ_p is at this stage largely a matter of guess work and the effectiveness should be evaluated by solving specific problems. We are looking only for sufficient conditions to satisfy the Eq. (3.51), and one way to satisfy this equation is to assume the stress tensor of the mixture to be

$$\begin{aligned} \mathbf{T} = & -\hat{p}\mathbf{I} + \alpha \left(\frac{\mu_1^m \theta}{\theta_m} \mathbf{B}_{\kappa_{pm}(t)} + \frac{2\mu_2^m \theta}{\theta_m} \mathbf{B}_{\kappa_{pm}(t)}^2 + 2\nu_3^m \mathbf{D} \right) \\ & + (1 - \alpha) \left(\mu_1^s \mathbf{B}_{\kappa_{ps}(t)} + \mu_2^s \mathbf{B}_{\kappa_r} \right) = -\hat{p}\mathbf{I} + \alpha \mathbf{T}_m + (1 - \alpha) \mathbf{T}_s, \end{aligned} \quad (3.54)$$

and the entropy of the mixture to be

$$\eta = \alpha \eta_m + (1 - \alpha) \eta_s, \quad (3.55)$$

guided by Eq. (4.25). Recognizing that the rate of dissipation is additive in the two components of the mixture weighted by the mass fraction, we suppose that

$$\left[\frac{\mu_1^m \theta}{\theta_m} \mathbf{B}_{\kappa_{pm}(t)} + \frac{2\mu_2^m \theta}{\theta_m} \mathbf{B}_{\kappa_{pm}(t)}^2 \right] \cdot \mathbf{D}_{\kappa_{pm}(t)} = \left(\xi_m - 2\nu_3^m \mathbf{D} \cdot \mathbf{D} \right), \quad (3.56)$$

and the material conversion kinetics to be

$$\begin{aligned} \rho(\Psi_m - \Psi_s)\dot{\alpha} &= \{A(1 - \alpha^m) + B(1 - \alpha^n)\}\dot{\alpha} \Rightarrow \rho(\Psi_m - \Psi_s) \\ &= A(1 - \alpha^m) + B(1 - \alpha^n) \text{ or } \dot{\alpha} = 0, \end{aligned} \quad (3.57)$$

If $\dot{\alpha} = 0$, Eq. (3.57) would imply that the fraction of the melt is always a constant. In other words, there is no phase change. Therefore, one needs to pick the other equation.

Using the Eqs. (3.54), (3.55), (3.56) and (3.57) in Eq. (3.51), one arrives at

$$\mu_1^s \mathbf{B}_{\kappa_{ps}(t)} \cdot \mathbf{D}_{\kappa_{ps}(t)} = \xi_s. \quad (3.58)$$

The internal energy of the mixture per unit mass, ϵ , using the relation $\epsilon = \Psi + \eta\theta$, is

$$\epsilon = \alpha\epsilon_m + (1 - \alpha)\epsilon_s, \quad (3.59)$$

where ϵ_s is the internal energy of the solid and is defined through

$$\begin{aligned} \epsilon_s &= \Psi_s + \eta_s\theta = A^s - B^s\theta_s + \frac{c_1^s}{2}(\theta^2 - \theta_s^2) + c_2^s(\theta - \theta_s) \\ &+ \frac{\mu_1^s}{2\rho}(I_{\kappa_{ps}(t)} - 3) + \frac{\mu_2^s}{2\rho}(I_{\kappa_r} - 3). \end{aligned} \quad (3.60)$$

When the polymer exists in a pure melt-like or in a pure solid-like state, the entropy production due to phase change is zero because there is no conversion of the material in progress. We suppose that the rate of entropy production due to phase change is zero at the beginning and at the end of the transition. Such an assumption would also ensure that the ξ_p is continuous throughout the polymer processing range. As $\alpha \rightarrow 1$, the right hand side of the Eq. (3.57)₂ tends to zero and the only way to satisfy the left hand side of the same equation is to let $\Psi_m \rightarrow \Psi_s$; it serves as an initiation criterion (see Eq. (3.61)) for the mixture model. By differentiating the

Eq. (3.57)₂ with respect to time (material derivative) and letting $\alpha \rightarrow 1$ reveals that $\dot{\alpha} \neq 0$ provided that $\overline{\Psi_m - \Psi_s} \neq 0$. Since one expects that $\xi_p \rightarrow 0$ at the end of the transitional regime ($\alpha \rightarrow 0$), differentiating Eq. (3.57)₂ with respect to time reveals that $\dot{\alpha} \rightarrow 0$ as $\alpha \rightarrow 0$. It is also true that $\dot{\alpha} \leq 0$ if $\overline{\Psi_m - \Psi_s} \geq 0$ (for arbitrary α), i.e., $\Psi_m - \Psi_s$ is monotonic with time.

If one assumes that the solid is born in a stress free state, then

$$\Psi_m - \Psi_s \Big|_{\mathbf{B}_{\kappa_r} = \mathbf{B}_{\kappa_{ps}(t)} = \mathbf{I}} = \phi(\theta, \mathbf{B}_{\kappa_{pm}(t)}). \quad (3.61)$$

The above equation serves as an initiation criterion for the mixture model. Since $\Psi_m = \Psi_s$ at the initiation point of the mixture model and the monotonicity implies that $\Psi_m - \Psi_s$ is always positive and non-decreasing with time.

We shall exploit the monotonicity of the function $\Psi_m - \Psi_s$ to arrive at some restrictions on some of the material constants appearing in it. In the absence of any deformation $I_{\kappa_{pm}(t)} = II_{\kappa_{pm}(t)} = I_{\kappa_{ps}(t)} = I_{\kappa_r} = 3$ and the monotonicity condition reduces to

$$\left[B^m - c_1^m(\theta - \theta_m) - c_2^m \ln\left(\frac{\theta}{\theta_m}\right) - B^s + c_1^s(\theta - \theta_s) + c_2^s \ln\left(\frac{\theta}{\theta_s}\right) \right] \dot{\theta} \geq 0. \quad (3.62)$$

The above inequality is valid for all θ in the mixture regime. The rate of change of the absolute temperature cannot be positive because it implies that increasing the temperature would cause the material to solidify. This is contrary to observations. Thus, $\dot{\theta} \leq 0$. This and the above inequality imply that

$$B^m - c_1^m(\theta - \theta_m) - c_2^m \ln\left(\frac{\theta}{\theta_m}\right) - B^s + c_1^s(\theta - \theta_s) + c_2^s \ln\left(\frac{\theta}{\theta_s}\right) \leq 0. \quad (3.63)$$

We shall require that the above inequality be respected even in the presence of deformation. If $c_1^m\theta + c_2^m > c_1^s\theta + c_2^s$, in the absence of mechanical deformation, the function $\Psi_m - \Psi_s$ is strictly concave (second derivative of $\Psi_m - \Psi_s$ with respect to temperature is negative); the inequality (3.63) restricts $\Psi_m - \Psi_s$ to the region of negative slope in

$\theta - f(\theta)$ space.

To obtain the evolution equation for the configurations $\kappa_{p_m(t)}$ and $\kappa_{p_s(t)}$, we adopt the maximization of entropy production assumption similar to that discussed in the previous section. Here, we maximize the rate of entropy production associated with mechanical working of the mixture with respect to $\mathbf{D}_{\kappa_{p_m(t)}}$ and $\mathbf{D}_{\kappa_{p_s(t)}}$ with the equations $\text{tr}\mathbf{D}_{\kappa_{p_m(t)}} = 0$, $\text{tr}\mathbf{D}_{\kappa_{p_s(t)}} = 0$, (3.56) and (3.58) as constraints. The augmented function, Φ , is

$$\begin{aligned} \Phi = & \alpha \xi_m + (1 - \alpha) \xi_s + \lambda_1 \alpha \left\{ \xi_m - 2\nu_3^m \mathbf{D} \cdot \mathbf{D} - (\mathbf{T}_m - 2\nu_3^m \mathbf{D}) \cdot \mathbf{D}_{\kappa_{p_m(t)}} \right\} \\ & + \lambda_2 (1 - \alpha) \left\{ \xi_s - (\mathbf{T}_s - \mu_2^s \mathbf{B}_{\kappa_r}) \cdot \mathbf{D}_{\kappa_{p_s(t)}} \right\} + \lambda_3 \text{tr}\mathbf{D}_{\kappa_{p_m(t)}} + \lambda_4 \text{tr}\mathbf{D}_{\kappa_{p_s(t)}}, \end{aligned} \quad (3.64)$$

where λ_1 , λ_2 , λ_3 and λ_4 are Lagrange multipliers.

By setting the derivatives of Φ to zero results in the following two equations:

$$\begin{aligned} \frac{\partial \Phi}{\partial \mathbf{D}_{\kappa_{p_m(t)}}} = \mathbf{0} & \Rightarrow \alpha \left(\frac{1 + \lambda_1}{\lambda_1} \right) \frac{\partial \xi_m}{\partial \mathbf{D}_{\kappa_{p_m(t)}}} - \alpha (\mathbf{T}_m - 2\nu_3^m \mathbf{D}) + \frac{\lambda_3}{\lambda_1} \mathbf{I} = \mathbf{0}, \\ \text{and} \\ \frac{\partial \Phi}{\partial \mathbf{D}_{\kappa_{p_s(t)}}} = \mathbf{0} & \Rightarrow (1 - \alpha) \left(\frac{1 + \lambda_2}{\lambda_2} \right) \frac{\partial \xi_s}{\partial \mathbf{D}_{\kappa_{p_s(t)}}} - (1 - \alpha) (\mathbf{T}_s - \mu_2^s \mathbf{B}_{\kappa_r}) \\ & + \frac{\lambda_4}{\lambda_2} \mathbf{I} = \mathbf{0}. \end{aligned} \quad (3.65)$$

Starting from the above two equations, it is possible to show that the tensor pairs $\mathbf{B}_{\kappa_{p_m(t)}}$, $\mathbf{D}_{\kappa_{p_m(t)}}$ and $\mathbf{B}_{\kappa_{p_s(t)}}$, $\mathbf{D}_{\kappa_{p_s(t)}}$ commute (multiplicatively). Using this property and taking the inner products of the Eq. (3.65)₁ with $\mathbf{D}_{\kappa_{p_m(t)}}$ and the Eq. (3.65)₂ with $\mathbf{D}_{\kappa_{p_s(t)}}$, and comparing with the Eqs. (3.56) and (3.58), the Lagrange multipliers $\frac{1 + \lambda_1}{\lambda_1}$ and $\frac{1 + \lambda_2}{\lambda_2}$ are determined to be $\frac{1}{2\beta}$ and $\frac{1}{2}$ respectively. By premultiplying the Eq. (3.65)₁ by $\mathbf{B}_{\kappa_{p_m(t)}}^{-1}$ and operating with the trace operator, we find that, $\frac{\lambda_3}{\lambda_1}$ is $\alpha \left(p + \frac{\lambda_2^m}{\lambda_1^m} \right)$. Similarly, $\frac{\lambda_4}{\lambda_1}$ is $(1 - \alpha) \frac{3\mu_1^s}{\text{tr}\mathbf{B}_{\kappa_{p_s(t)}}^{-1}}$. The evolution equations for the mixture

consists in prescribing how the configurations, namely, $\kappa_{p_m(t)}$ and $\kappa_{p_s(t)}$ evolve; the procedure for obtaining such equations is the same as that used in §4. The evolution equation for $\kappa_{p_m(t)}$ is the same as the Eq. (3.36), while that of the configuration $\kappa_{p_s(t)}$ is

$$\overset{\nabla}{\mathbf{B}}_{\kappa_{p_s(t)}} = \frac{\mu_1^s}{\nu^s} \left(\frac{3}{\text{tr} \mathbf{B}_{\kappa_{p_s(t)}}^{-1}} \mathbf{I} - \mathbf{B}_{\kappa_{p_s(t)}} \right). \quad (3.66)$$

By following a similar procedure discussed in the previous section, the extremum with maximum rate of dissipation is chosen by inspection.

E. Modeling the solid

Many amorphous polymers such as polymethylmethacrylate (PMMA), polycarbonate, polystyrene, and so forth, behave like a viscoelastic solid sufficiently below glass transition temperature. For example, stress relaxation of polycarbonate (whose glass transition temperature $\theta_g \approx 140^\circ\text{C}$) at 50°C indicates that the stress asymptotically decreases to some fixed value (Malkin *et al.* [35]). Creep data of polyvinyl chloride (PVC) at 24°C ($\theta_g \approx 65^\circ\text{C}$) indicates that, after sufficient time, the strain approaches some fixed value. Further loading, given sufficient time, the sample reverts to its original length (see Onaran and Findley [46]). PMMA ($\theta_g = 123^\circ\text{C}$) behaves like a viscoelastic solid in that the stress asymptotically approaches some fixed value during an 'anti-stress relaxation' experiment, which is described below (see Quinson *et al.* [56]). These data indicate that, sufficiently below glass transition temperature, such polymers exhibit solid-like character.

In the glassy state, aging plays an important role. There is experimental evidence indicating that the mechanical response of the aged sample can differ considerably when compared to the unaged specimen. The model for the solid presented here does not address this issue and the model should only be applied to such thermo-

mechanical processes that are 'fast' enough where aging effects are not significant. When a polymer in the solid state is sufficiently deformed, permanent deformation sets in. The model presented here only deals with deformation below the 'yield' limit. Another issue of interest is the anisotropy in the solid; the solid forms in a deformed state (at κ_r). In fiber spinning, the solid fiber is often transversely isotropic. Again, we emphasize that the thermomechanical framework presented here is general and all the above mentioned phenomena can be included under this umbrella. Particularly, the issue of anisotropy induced during the crystallization of polymers is discussed at length by Rao and Rajagopal (see [73]).

Using the definition of the functions Ψ_s and ξ_s given through the Eqs. (3.47) and (3.49), respectively, in the reduced dissipation equation (4.21), and following a procedure similar to that in §3, we find that the stress tensor is given by

$$\mathbf{T}_s = -p^s \mathbf{I} + \mu_1^s \mathbf{B}_{\kappa_{p_s}(t)} + \mu_2^s \mathbf{B}_{\kappa_r}, \quad (3.67)$$

where p^s is the Lagrange multiplier. The entropy, the internal energy, and the evolution equation for the natural configuration of the solid are given by the Eqs. (3.52), (3.60), and (3.66) respectively. The evolution equation for the natural configuration is obtained by maximizing the rate of dissipation (see Rajagopal and Srinivasa [58]). For the function ϵ_s , just as in §3, we shall require that $c_1^s > 0$ and $c_1^s \theta + c_2^s > 0$. In the limit $\alpha \rightarrow 0$, the model for the mixture regime tends to the same set of equations as that for the solid. Thus, there is a smooth transition from the equations representing the mixture to the equations for the solid (a similar smooth transition occurs as $\alpha \rightarrow 1$).

The evolving configuration $\kappa_{p_s}(t)$ captures the viscoelastic nature of the solid (temporal response of the body).

1. Relationship to the Standard Linear Solid (SLS)

The non-linear incompressible SLS may be defined through

$$\mathbf{T} = -p\mathbf{I} + \mathbf{S} \quad (3.68)$$

and

$$\mathbf{S} + \tau_1 \overset{\nabla}{\mathbf{S}} = 2\tau_1 \bar{\mu}_1 \mathbf{D} + \bar{\mu}_2 \mathbf{B}_{\kappa_r}. \quad (3.69)$$

By eliminating the tensor \mathbf{S} between the above two equations, adding and subtracting $2\tau_1 \bar{\mu}_2 \mathbf{D}$, and using (4.13), leads to

$$\frac{1}{\tau_1} \bar{\mathbf{T}}_e + \overset{\nabla}{\bar{\mathbf{T}}}_e = 2(\bar{\mu}_1 + \bar{\mu}_2) \mathbf{D} + \frac{\bar{\mu}_2}{\tau_1} (\mathbf{B}_{\kappa_r} - \mathbf{I}), \quad (3.70)$$

where $\bar{\mathbf{T}}_e = \mathbf{T} + \bar{p}\mathbf{I}$, $\bar{p} = p - \bar{\mu}_2$.

The above equation is a generalization of the to the one-dimensional mechanical analog of the SLS.

Then, Eqs. (3.68) and (3.69) can be recast (see Rajagopal and Srinivasa [58]) in the following form:

$$\mathbf{T} = -\tilde{p}\mathbf{I} + \bar{\mathbf{S}}, \quad \tilde{p} = p + \bar{\mu}_1 \text{ and } \bar{\mathbf{S}} = \mathbf{S} + \bar{\mu}_1 \mathbf{I} \quad (3.71)$$

and

$$\bar{\mathbf{S}} + \tau_1 \overset{\nabla}{\bar{\mathbf{S}}} = (\bar{\mu}_1 + \bar{\mu}_2) \mathbf{I} + \bar{\mu}_2 (\mathbf{B}_{\kappa_r} - \mathbf{I}). \quad (3.72)$$

To see the relationship of the model for the solid obtained in this paper to the Eqs. (3.71) and (3.72), the Eqs. (3.67) and (3.66) are rewritten as follows:

$$\mathbf{T}_s = -p^s \mathbf{I} + \hat{\mathbf{S}}, \quad \hat{\mathbf{S}} = \mu_1^s \mathbf{B}_{\kappa_{ps}(t)} + \mu_2^s \mathbf{B}_{\kappa_r}, \quad (3.73)$$

and

$$\hat{\mathbf{S}} + \frac{\nu^s}{\mu_1^s} \overset{\nabla}{\hat{\mathbf{S}}} = (\mu_1^s \hat{\lambda} + \mu_2^s) \mathbf{I} + \mu_2^s (\mathbf{B}_{\kappa_r} - \mathbf{I}), \quad \hat{\lambda} = \frac{3}{\mu_1^s \text{tr}(\hat{\mathbf{S}} - \mu_2^s \mathbf{B}_{\kappa_r})^{-1}} = \frac{3}{\text{tr} \mathbf{B}_{\kappa_{ps}(t)}^{-1}}. \quad (3.74)$$

Except for the form of $\hat{\lambda}$, the two sets of equation have a similar form. If $\| \mathbf{B}_{\kappa_{ps}(t)} - \mathbf{I} \| = O(\epsilon)$, $\epsilon \ll 1$, it can be shown that $\text{tr} \mathbf{B}_{\kappa_{ps}(t)}^{-1} = 3 + O(\epsilon^2)$ (see Rajagopal and Srinivasa [58]). In this sense the model for the solid obtained in this paper can be viewed as a generalization of the SLS described through the Eqs. (3.68) and (3.69).

2. An application of the model for solid

We shall now consider an application to evaluate the efficacy of the solid model that we have developed. Let us consider the following experiment for which the data is available.

Let us consider a cylindrical sample of about 8mm in diameter and about 12mm in length that is uniaxially compressed by applying a constant load rate for a duration of t_1 seconds until a given stress T_f is reached in a suitable testing machine (see Quinson *et al.* [56]) at some fixed temperature. At the end of the loading cycle, let us suppose that the material is unloaded at the same rate for a further duration of t_1 seconds. Further, let us suppose that it is held at constant strain for the remaining time and that the force is measured as a function of time (referred to as 'anti-stress relaxation'). The effect of preload is not taken into consideration because the duration of the same is unknown. Due to the viscoelastic nature of the solid, the force that is measured changes after the loading and unloading.

We shall assume that the deformation is homogeneous and in uniaxial compression, given by:

$$x = \frac{1}{\lambda^2(t)}X, \quad y = \lambda(t)Y, \quad z = \lambda(t)Z. \quad (3.75)$$

The components of velocity gradient tensor are

$$[\mathbf{L}] = [\mathbf{D}] = [\dot{\mathbf{F}}_{\kappa_r} \mathbf{F}_{\kappa_r}^{-1}] = \text{diag} \left\{ \frac{-2\dot{\lambda}(t)}{\lambda(t)}, \frac{\dot{\lambda}(t)}{\lambda(t)}, \frac{\dot{\lambda}(t)}{\lambda(t)} \right\}. \quad (3.76)$$

The components of $\mathbf{B}_{\kappa_{ps}(t)}$ are assumed to be

$$[\mathbf{B}_{\kappa_{ps}(t)}] = \text{diag}\left\{\frac{1}{B^2(t)}, B(t), B(t)\right\}. \quad (3.77)$$

Substituting the above two equations into Eq. (3.66) results in

$$4\frac{\dot{\lambda}(t)}{\lambda(t)}B(t) - \frac{\mu_1^s}{\nu^s}\left(\frac{3B^4(t)}{2+B^3(t)} - B(t)\right) = 2\dot{B}(t). \quad (3.78)$$

The components of the tensor \mathbf{B}_{κ_r} are

$$[\mathbf{B}_{\kappa_r}] = \text{diag}\left\{\frac{1}{\lambda^4(t)}, \lambda^2(t), \lambda^2(t)\right\}. \quad (3.79)$$

During the loading cycle, using the fact that the lateral surfaces are stress-free, the constitutive equation (3.67) reduces to

$$T_{xx} = T_{11} = -\frac{T_f t}{t_1} = \mu_1^s\left(\frac{1-B^3(t)}{B^2(t)}\right) + \mu_2^s\left(\frac{1-\lambda^6(t)}{\lambda^4(t)}\right), \quad T_f \geq 0, \quad 0 \leq t \leq t_1, \quad (3.80)$$

where T_f is the preset magnitude of the maximum stress applied during the loading cycle and t_1 is the duration of the loading cycle. One needs to solve the Eqs. (3.78) and (3.80) in tandem. We shall proceed to determine $\lambda(t)$ in terms of the remaining parameters.

The above equation is a cubic equation in $\bar{\lambda}(t)$ (sextic in $\lambda(t)$) with $\bar{\lambda}(t) = \lambda^2(t)$, i.e., $\bar{\lambda}^3(t) + b_l \bar{\lambda}^2(t) - 1 = 0$, where $b_l = \frac{\mu_1^s}{\mu_2^s}\left(\frac{B^3(t)-1}{B^2(t)}\right) - \frac{T_f t}{t_1 \mu_2^s}$. For any fixed $B(t)$, there are three roots for $\bar{\lambda}(t)$. If the value of the discriminant $D > 0$, where $D = \left(\frac{27-2b_l^3}{54}\right)^2 - \frac{b_l^6}{729}$, there is one real root and the other two are complex conjugates. If $D \leq 0$ all the roots are real (see Abramovitz and Stegun [1]). Since the stretch $\lambda(t) \geq 1$, using Eq. (3.80), it is easy to see that b_l has to be negative. But, $b_l < 0$ implies that $D > 0$. Thus, $\bar{\lambda}(t)$ has one real root and the other two are complex conjugates. Since $\lambda(t)$ ($\bar{\lambda}(t) = \lambda^2(t)$) cannot be negative or complex leads to a unique

expression, which is given by

$$\lambda(t) = \sqrt{\bar{\lambda}(t)}, \quad \bar{\lambda}(t) = -\frac{b_l(t)}{3} + \left(\frac{27 - 2b_l^3(t)}{54} + \sqrt{D} \right)^{1/3} + \left(\frac{27 - 2b_l^3(t)}{54} - \sqrt{D} \right)^{1/3}. \quad (3.81)$$

Substituting the Eq. (3.81) into Eq. (3.78) results in a differential equation for $B(t)$ that is numerically solved with the initial condition $B(0) = 1$. Alternatively, the Eq. (3.80) can be differentiated with respect to t to find $\dot{\lambda}(t)$ in terms of $\lambda(t)$, $\dot{B}(t)$, $B(t)$ and the other parameters; $\lambda(t)$ is given by the above equation with b_l being replaced by b_u .

During the unloading ($t_1 \leq t \leq 2t_1$), the evolution equation is the same as the Eq. (3.78), the term $\frac{-T_f t}{t_1}$ in the Eq. (3.80) is replaced by $\frac{T_f(t - 2t_1)}{t_1}$ and b_l in the Eq. (3.81) is replaced by b_u , where

$$b_u = \frac{\mu_1^s}{\mu_2^s} \left(\frac{B^3(t) - 1}{B^2(t)} \right) + \frac{T_f(t - 2t_1)}{t_1 \mu_2^s}, \quad t_1 \leq t \leq 2t_1. \quad (3.82)$$

A *posteriori* check of the Eq. (3.81), by solving the evolution equation (3.78) with appropriate initial conditions, revealed that $\lambda(t) \geq 1$ during loading and unloading. Since the sample is held at constant strain after the unloading period, the components of the velocity gradient tensor are all zero and the evolution equation is the same as Eq. (3.78) with $\frac{\dot{\lambda}(t)}{\lambda(t)} = 0$. During the constant strain period ($t \geq 2t_1$), the evolution equation is solved with the initial condition $B(2t_1)$ equal to the value of $B(t)$ at the end of the previous period. The whole problem is solved numerically using fourth order Runge-Kutta method implemented in Matlab.

For PMMA, in uniaxial compression, a strain (based on the current length) of about 8 ($\lambda \approx 1.04$) percent is the limit, after which permanent deformation sets in (see Quinson *et al.* [57]). The material constants were picked such that the strain is within this limit ('small' stretch regime). The results are presented in Fig. 15. We

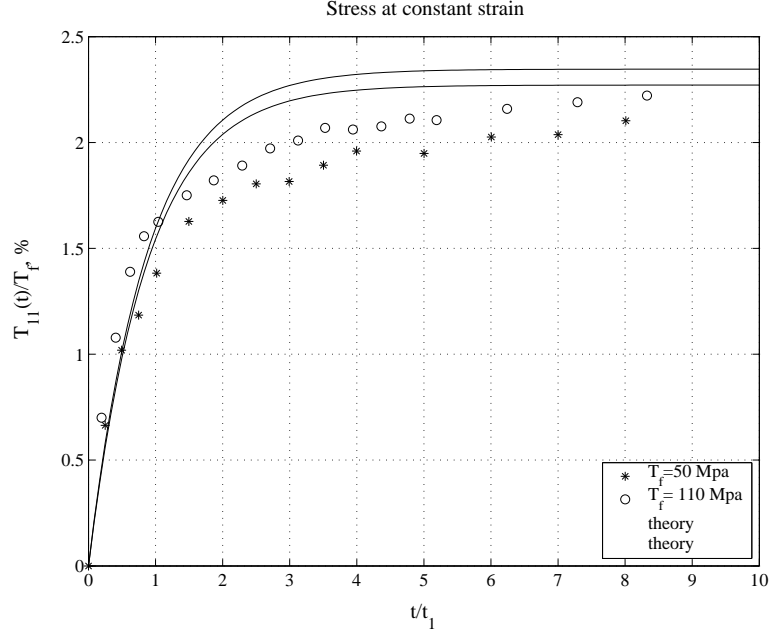


Fig. 15. The above figure shows the stress at constant strain after loading and unloading at 253K with $t_1 = 12$ s. The material constants used in the simulation are $\mu_1^s = 22.77$ Mpa, $\mu_2^s = 0.392$ Gpa, and $\nu^s = 0.24$ GPa.s. The initial conditions for $T_f = 50$ and 110Mpa are 0.9836 and 0.9636 respectively. The data for 170 and 230MPa is not shown.

find that the model predicts the asymptotic stresses that are within $\approx 8\%$ and $\approx 6\%$ of the experimental value for $T_f = 50$ and 110MPa respectively. Including the effect of preload could possibly improve the results. A better model can be obtained by picking a more complicated choice for the stored energy and the rate of dissipation. However, it is not our purpose here to build a more accurate model. Our main purpose is to develop a model that can predict the transition from a viscoelastic fluid to that of a viscoelastic solid, without adhoc assumptions for the transition or an assumption that the viscosity of the melt tends to infinity. The viscoelastic nature of the solid is clearly reflected in the Fig. 15. PMMA behaves like a solid, a constant stress (non zero) is reached after a sufficient length of time.

CHAPTER IV

FLOW INDUCED CRYSTALLIZATION IN FIBER SPINNING

In this paper, we extend the development of model within the thermomechanical framework due to Rao and Rajagopal [73] to describe the problem of polymer crystallization in general and the problem of fiber spinning in particular (see Kannan and Rajagopal [31]). This study is a generalization of previous study concerning fiber spinning by Kannan *et al.* [32] and it incorporates the effect due to material symmetry changes that take place during crystallization. The model incorporates the effects due melt viscoelasticity, drag on the fiber, gravity, inertia effects, the cooling of the fiber, the initiation of crystallization (that depends on both the temperature and deformation), flow induced crystallization and the anisotropy of the crystalline phase of the semicrystalline solid. The prediction of the model are compared with the experimental results that are available.

A. Introduction

There have been several models that have been developed to describe polymer crystallization. Recently, Rao and Rajagopal [73] put into place a general thermodynamic framework to describe polymer crystallization. The melt was modeled as a viscoelastic liquid and the semi crystalline solid was modeled as a mixture of elastic solids that are formed continuously and the original viscoelastic liquid. The material symmetry of the solid that is formed ('average' orientation of the crystals) at any particular instant, modeled as an orthotropic elastic solid, depends on deformation that the melt has suffered. Thus, the response of the final semicrystalline material depends on the process to which the melt was subjected during the course of crystallization. The initiation of crystallization would depends on the temperature and deformation,

the crystallization kinetics, the form of the stress, and so forth are obtained in a systematic manner from thermodynamic considerations. It should be mentioned that the evolving material symmetry is obtained as a part of the solution to the problem of interest.

We shall not get into a detailed review of the fiber spinning problem but refer the reader to Denn [10], Doufas *et al.* [14] and Kannan *et al.* [32] for the same (also see Ch. 2). Kannan *et al.* [32] used a simplified version of the theory in which the polymer melt was assumed to solidify into an isotropic elastic solid to describe low-speed fiber spinning of predominantly glassy polymers such as PET. Here, we consider the case of fiber spinning when crystallization takes place thereby leading to a semi-crystalline solid. There have been successful earlier studies (see Doufas *et al.* [14]) where fiber spinning has been considered within the context of crystallization. Patel *et al.* [49] used a Newtonian model to fit the data obtained by Bheda and Spruiell [4]. To capture the plateau in velocity after significant crystallization, the viscosity was allowed to increase to a large value. While this method is a good early attempt to model the problem, one does not obtain a solid in the semi-crystalline region and hence it is difficult to capture the velocity plateau that arises in fiber spinning due to solidification in spite of increasing the viscosity to a very high value (e.g. Zieminski and Spruiell [89]). Also, this model does not capture the anisotropy observed in the semicrystalline state, i.e., even if one decides to model the semicrystalline state as a liquid because given sufficient time a polymer in this state will behave like a liquid, one should model it as an anisotropic liquid (liquid being defined as a material that cannot resist shear stress). Sun *et al.* [77] used a viscoelastic liquid to simulate the problem (a modified PTT model) with the viscosity depending on temperature and crystallinity (2-D simulations) for the semicrystalline regime. Only a part of the data of Bheda and Spruiell [4] was used as the focus was on low-speed simulations.

Doufas *et al.* [15] modeled the melt as a viscoelastic liquid (Giesekus fluid) and the semicrystalline phase as a collection of rigid rods that grow, at the expense of the melt, and orient during deformation. Equilibrium melting temperature was used as an initiation criterion for crystallization. They obtained very good agreement with the industrial spinline data including the neck formation. Of all the models that are available, the microstructural model due to Doufas *et al.* [14] seems to be the most sophisticated and the predictions of their model agree very well with extensive sets of industrial spinline data. Studies on polyamides by Haberkorn *et al.* [27] indicate that the crystallization process is initiated towards the end of the necking phenomenon during high-speed fiber spinning, which occurs at a temperature that is much lesser than the equilibrium melting temperature. Doufas *et al.* [14] and [15] assume that the crystallization is initiated at the equilibrium melting temperature of the polymeric material, and they take the view that the crystallinity achieved between the equilibrium melting temperature and at a temperature near the end of the necking process is too small to show up in wide angle x-ray scattering (WAXS). Contrariwise, we take the view that the crystallization is initiated in non-equilibrium conditions at the end of the necking phenomenon and this is in keeping with the observation of Haberkorn *et al.* [27]. Haberkorn *et al.* [27] also noticed that the temperature at which solidification occurs is independent (to within experimental errors) of mass flow rate, capillary diameter, velocity and cross-flow cooling air velocity and dependent on the take-up velocity. In view of this we assume that the initiation condition for the crystallization process is only a function of temperature and deformation (see Eq. 4.1). We show that our model is able to describe equally well the same sets of industrial spinline data described by the model of Doufas *et al.* [14]. The material parameters in question are fixed with regard to one amongst a set of experiments and the other experiments in the set are correlated with the values for the material

parameters fixed in the first experiment. Here, we provide an alternate approach to the problem. As the approach is sufficiently different, we feel it is worth documenting our procedure.

In fiber spinning, we know that the crystals are always oriented along the length of the fiber (see Ziabicki [88]) during the course of crystallization. The axis of symmetry is *a priori* set as the direction along the length of the fiber. A number of authors have studied the fiber spinning problem and one may refer to, for example, Doufas *et al.* [14] for a detailed the list of relevant literature. In our analysis, unlike most previous studies the initiation of crystallization is assumed to depend on both the temperature and deformation and it naturally arises from the thermodynamic considerations. The appropriate averaged mass, momentum and the evolution equation and 2-D energy equation for the melt (radial resolution approximation) etc., are discussed elsewhere and it will not be discussed here (eg. see Vassilatos *et al.* [82]). First, the fiber spinning process is approximated by a thin-filament assumption (all the quantities of interest are assumed to be a function of the distance from the spinneret only, i.e., a 1-D approximation) to study the industrial spinline data reported in Doufas *et al.* [15] . Since the heat conduction in the radial direction cannot occur without a radial temperature gradient, one needs to make temperature a function of the radial distance r in addition to the distance from the spinneret z in the energy balance. However, the rest of the variables are assumed to be a function of z only. As a result, since the equations obtained for the mass, momentum and energy balance and the evolution equation are coupled, one needs to average the balance equations along the radial direction. Since the free surface of the fiber is obtained as a part of the solution and the governing equations are non-linear integro-differential equations and a non-linear integro-partial differential equation, numerical solution finding effort is considerable and time consuming due to the iterative nature of the

numerical procedure. Accordingly, the fiber spinning process is approximated using a radial resolution approximation and the predictions of the model are compared with the data of Patel *et al.* [49]. Our predictions of the model yield a slightly better prediction of temperature profiles compared to thin-filament approximation. Here, radial resolution approximation is used in the melt regime and thin-filament approximation, for simplicity, is used in the mixture regime. The governing equations for the thin-filament approximation used in the melt regime can be obtained by assuming radial independence of all the variables in §D.1.

B. Kinematics

As the general framework was discussed elsewhere (see Rao and Rajagopal [73]), we shall keep the discussion of modeling to that which is necessary to make the work comprehensible and self-contained. Let $\kappa_R(B)$ and $\kappa_t(B)$ denote the reference and the current configuration of the body B at time t respectively. By the motion of a body we mean a one to one mapping that assigns to each point $\mathbf{X} \in \kappa_R(B)$, a point $\mathbf{x} \in \kappa_t(B)$, for each t ,

$$\mathbf{x} = \boldsymbol{\chi}_{\kappa_R}(\mathbf{X}_{\kappa_R}, t). \quad (4.1)$$

We shall assume that this motion is sufficiently smooth and invertible. The velocity of a particle is defined through

$$\mathbf{v} = \frac{\partial \boldsymbol{\chi}_{\kappa_R}}{\partial t}. \quad (4.2)$$

For brevity, henceforth we shall drop the argument B in $\kappa_t(B)$. The deformation gradient, \mathbf{F}_{κ_R} , the left and right Cauchy-Green stretch tensors \mathbf{B}_{κ_R} and \mathbf{C}_{κ_R} are defined through

$$\mathbf{F}_{\kappa_R} = \frac{\partial \boldsymbol{\chi}_{\kappa_R}}{\partial \mathbf{X}_{\kappa_R}}, \quad \mathbf{B}_{\kappa_R} = \mathbf{F}_{\kappa_R} \mathbf{F}_{\kappa_R}^T, \quad \text{and} \quad \mathbf{C}_{\kappa_R} = \mathbf{F}_{\kappa_R}^T \mathbf{F}_{\kappa_R}. \quad (4.3)$$

The principal invariants of \mathbf{B}_{κ_R} are

$$I_{\kappa_R} = \text{tr}(\mathbf{B}_{\kappa_R}), \quad II_{\kappa_R} = \frac{1}{2} \left\{ [\text{tr}(\mathbf{B}_{\kappa_R})]^2 - \text{tr}(\mathbf{B}_{\kappa_R}^2) \right\}, \quad \text{and} \quad III_{\kappa_R} = \det(\mathbf{B}_{\kappa_R}). \quad (4.4)$$

Let $\kappa_{pm(t)}$ denote the configuration associated with the configuration at κ_t (see Fig. (16)). We refer the reader to Kannan *et al.* [32] and Rao and Rajagopal [73] where the notion of evolving natural configurations is discussed with regard to issues concerning polymer crystallization. The left and the right elastic Cauchy Green stretch tensors are defined through

$$\mathbf{B}_{\kappa_{pm(t)}} = \mathbf{F}_{\kappa_{pm(t)}} \mathbf{F}_{\kappa_{pm(t)}}^T \quad \text{and} \quad \mathbf{C}_{\kappa_{pm(t)}} = \mathbf{F}_{\kappa_{pm(t)}}^T \mathbf{F}_{\kappa_{pm(t)}}, \quad (4.5)$$

respectively, where $\mathbf{F}_{\kappa_{pm(t)}}$ is the mapping between the tangent spaces at the appropriate points belonging to the configurations $\kappa_{pm(t)}$ and κ_t . The principal invariants of $\mathbf{B}_{\kappa_{pm(t)}}$ are $I_{\kappa_{pm(t)}}$, $II_{\kappa_{pm(t)}}$ and $III_{\kappa_{pm(t)}}$.

The mapping \mathbf{G}_m is defined through (see Fig. (16))

$$\mathbf{G}_m = \mathbf{F}_{\kappa_R \rightarrow \kappa_{pm(t)}} = \mathbf{F}_{\kappa_{pm(t)}}^{-1} \mathbf{F}_{\kappa_R}. \quad (4.6)$$

The velocity gradient and the mapping $\mathbf{L}_{\kappa_{pm(t)}}$ are defined through

$$\begin{aligned} \mathbf{L} &:= \dot{\mathbf{F}}_{\kappa_R} \Big|_{\mathbf{x}_{\kappa_R} = \text{const.}} \mathbf{F}_{\kappa_R}^{-1} \quad \text{and} \\ \mathbf{L}_{\kappa_{pm(t)}} &= \dot{\mathbf{G}}_m \mathbf{G}_m^{-1}. \end{aligned} \quad (4.7)$$

The symmetric parts of \mathbf{L} and $\mathbf{L}_{\kappa_{pm(t)}}$ are

$$\mathbf{D} = \frac{1}{2}(\mathbf{L} + \mathbf{L}^T) \quad \text{and} \quad \mathbf{D}_{\kappa_{pm(t)}} = \frac{1}{2}(\mathbf{L}_{\kappa_{pm(t)}} + \mathbf{L}_{\kappa_{pm(t)}}^T). \quad (4.8)$$

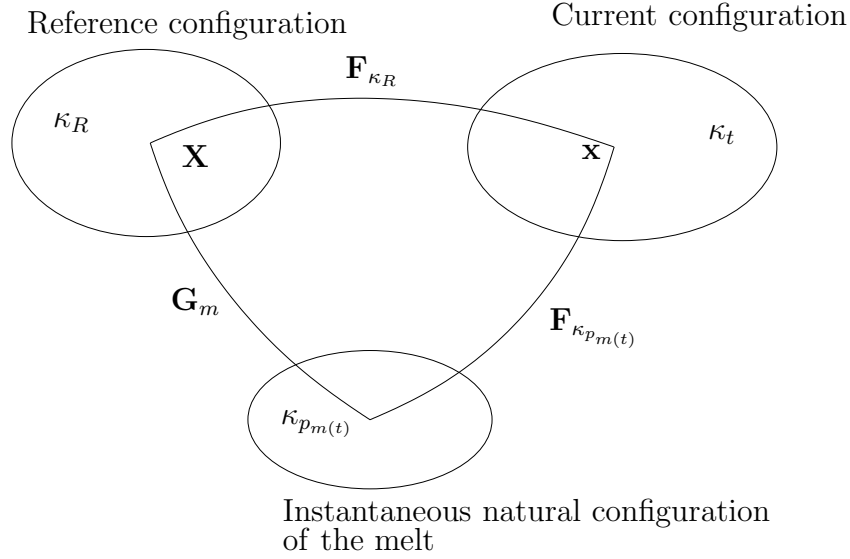


Fig. 16. The figure represents the configurations associated with the melt. The point \mathbf{X} is the position occupied by the particle in the reference configuration. The point \mathbf{x} is the current position of the particle.

The upper convected Oldroyd derivative of $\mathbf{B}_{\kappa_{p_m(t)}}$ is defined through (see Oldroyd (1950))

$$\overset{\nabla}{\mathbf{B}}_{\kappa_{p_m(t)}} = \dot{\mathbf{B}}_{\kappa_{p_m(t)}} - \mathbf{L}\mathbf{B}_{\kappa_{p_m(t)}} - \mathbf{B}_{\kappa_{p_m(t)}}\mathbf{L}^T = -2\mathbf{F}_{\kappa_{p_m(t)}}\mathbf{D}_{\kappa_{p_m(t)}}\mathbf{F}_{\kappa_{p_m(t)}}^T. \quad (4.9)$$

The mapping $\mathbf{F}_{\kappa_c(\tau)}$ (see Fig. (17)) is defined through

$$\mathbf{F}_{\kappa_c(\tau)} := \mathbf{F}_{\kappa_R}(\mathbf{X}_{\kappa_R}, t)\mathbf{F}_{\kappa_R}^{-1}(\mathbf{X}_{\kappa_R}, \tau), \quad t_o \leq \tau \leq t, \quad (4.10)$$

where t_o is the time at which crystallization is initiated. One can define relative left and right stretch tensors and the principal invariants that are related to $\mathbf{F}_{\kappa_c(\tau)}$.

We shall assume that the material is incompressible, i.e.,

$$\det(\mathbf{B}_{\kappa_{p_m(t)}}) = 1 \quad (\text{or } \text{tr}(\mathbf{L}_{\kappa_{p_m(t)}}) = 0) \quad \text{and} \quad \text{tr}(\mathbf{L}) = 0. \quad (4.11)$$

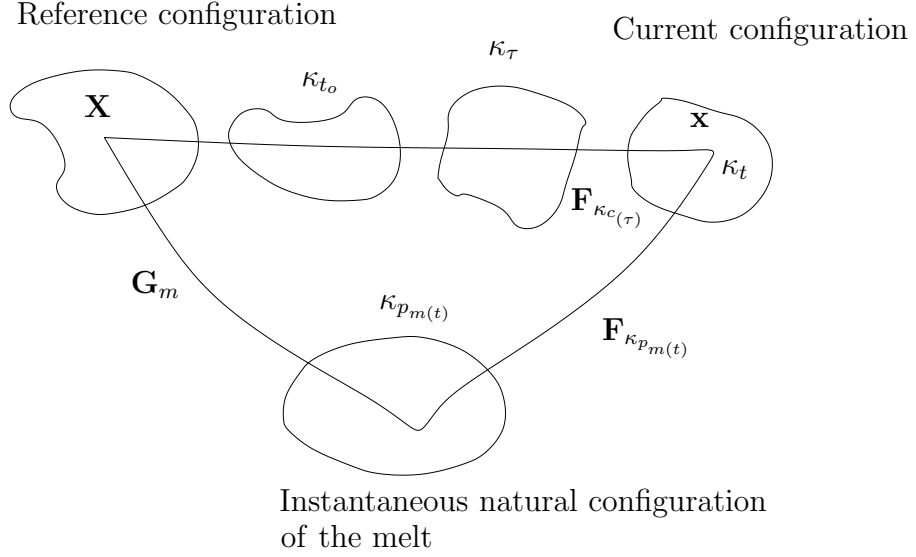


Fig. 17. The figure represents the configurations associated with the mixture.

C. Modeling the melt and the semicrystalline solid

1. Modeling the melt

The starting point for the derivation is the specification of two scalars namely, the Helmholtz per unit mass and the rate of dissipation per unit volume, which are defined as follows:

$$\begin{aligned} \Psi_m(\theta, I_{\kappa_{p_m(t)}}) &= A^m + (B^m + c_2^m)(\theta - \theta_m) - c_1^m \frac{(\theta - \theta_m)^2}{2} \\ &- c_2^m \theta \ln \left(\frac{\theta}{\theta_m} \right) + \frac{\mu^m \theta}{2\rho\theta_m b} \left\{ \left[1 + \frac{b}{n} (I_{\kappa_{p_m(t)}} - 3) \right]^n - 1 \right\}, \end{aligned} \quad (4.12)$$

where θ_m , A^m , B^m , c_1^m , c_2^m , b , n and μ^m are the reference temperature and the material constants, respectively, and

$$\xi_m(\theta, \mathbf{B}_{\kappa_{p_m(t)}}, \mathbf{D}_{\kappa_{p_m(t)}}) = 2\nu^m(\theta, \mathbf{B}_{\kappa_{p_m(t)}}) \left\{ \mathbf{D}_{\kappa_{p_m(t)}} \cdot \mathbf{B}_{\kappa_{p_m(t)}} \mathbf{D}_{\kappa_{p_m(t)}} \right\}^\beta, \quad (4.13)$$

where $\nu^m(\theta, \mathbf{B}_{\kappa_{p_m(t)}})$ is the viscosity of the melt and β is a constant. The above definition for the dissipation guarantees that it be non-negative.

The functional form of the Eq. (4.12) has been constructed in such a way that the specific heat of the melt is linear in θ , and at constant temperature the stored energy of the polymer melt is assumed to be that of a power law neo-Hookean material. Further, when $b, n = 1$, the shear modulus of the material is proportional to temperature, which is consistent with the Gaussian network theory (see Treolar [81]). The rate of dissipation function is of the same form as chosen by Srinivasa [76].

By following the procedure outlined in Rao and Rajagopal [73], it can be shown that the stress tensor has the form:

$$\mathbf{T}_m = -p\mathbf{I} + \frac{\mu^m \theta}{\theta_m} \left[1 + \frac{b}{n} (I_{\kappa_{pm}(t)} - 3) \right]^{n-1} \mathbf{B}_{\kappa_{pm}(t)}, \quad (4.14)$$

and the evolution of the natural configuration is given by

$$\begin{aligned} \overset{\nabla}{\mathbf{B}}_{\kappa_{pm}(t)} = & 2 \left\{ \frac{\mu^m \theta}{2\nu^m \theta_m} \left[1 + \frac{b}{n} (I_{\kappa_{pm}(t)} - 3) \right]^{n-1} \left[\text{tr} \mathbf{B}_{\kappa_{pm}(t)} - \frac{9}{\text{tr}(\mathbf{B}_{\kappa_{pm}(t)}^{-1})} \right]^{1-\beta} \right\}^{\frac{1}{2\beta-1}} \\ & \times \left[\frac{3}{\text{tr}(\mathbf{B}_{\kappa_{pm}(t)}^{-1})} \mathbf{I} - \mathbf{B}_{\kappa_{pm}(t)} \right]. \end{aligned} \quad (4.15)$$

The internal energy per unit mass and specific heat capacity of the melt are

$$\begin{aligned} \epsilon_m = & A^m - B^m \theta_m + \frac{1}{2} c_1^m (\theta^2 - \theta_m^2) + c_2^m (\theta - \theta_m) \text{ and} \\ \frac{\partial \epsilon_m}{\partial \theta} = & c_1^m \theta + c_2^m. \end{aligned} \quad (4.16)$$

2. Modeling the semicrystalline solid

The specific Helmholtz potential of the semicrystalline solid is partitioned into two parts, i.e., one that corresponds to the crystalline part and the other relates to the amorphous part with each part being weighted by their corresponding mass fractions.

We define the specific Helmholtz potential of the mixture, Ψ , as follows:

$$\begin{aligned}
\Psi &= \int_{t_o}^t \left\{ A^s + (B^s + c_2^s)(\theta(t) - \theta_s) - c_1^s \frac{(\theta(t) - \theta_s)^2}{2} - c_2^s \theta(t) \ln \left(\frac{\theta(t)}{\theta_s} \right) \right. \\
&+ \left. \frac{\mu_1^s}{2\rho} (I_{\kappa_c(\tau)} - 3) + \frac{\mu_2^s}{2\rho} (J_{\kappa_c(\tau)} - 1)^2 \right\} \frac{d\alpha(\tau)}{d\tau} d\tau + (1 - \alpha) \Psi_m \\
&= \Psi_s + (1 - \alpha) \Psi_m,
\end{aligned} \tag{4.17}$$

where $J_{\kappa_c(\tau)} := \mathbf{C}_{\kappa_c(\tau)} \mathbf{n}_{\kappa_c(\tau)} \cdot \mathbf{n}_{\kappa_c(\tau)}$ and $\mathbf{n}_{\kappa_c(\tau)}$ is the eigen vector of the tensor $\mathbf{B}_{\kappa_{pm}(t)}$ corresponding to the largest eigen value. The integral for the crystalline part reflects the fact that the solid is formed continuously from the melt over a period of time (see Rao and Rajagopal [73]). The integrand refers to the Helmholtz potential of a transversely isotropic elastic solid (due to flow induced anisotropy) that is in the configuration $\kappa(t)$, which came into being in the configuration $\kappa(\tau)$. The temperature in the integrand is only a function of current time t , i.e., the effect of the thermal history is not included in the Helmholtz potential. We note that as $t \rightarrow t_o$, $\alpha \rightarrow 0$ and one can recover the specific Helmholtz potential of the melt. Thus continuity is ensured as far as the specific Helmholtz potential is concerned.

The rate of dissipation per unit volume of the mixture is defined through

$$\xi = (1 - \alpha) 2\nu^m(\theta, \mathbf{B}_{\kappa_{pm}(t)}) \left\{ \mathbf{D}_{\kappa_{pm}(t)} \cdot \mathbf{B}_{\kappa_{pm}(t)} \mathbf{D}_{\kappa_{pm}(t)} \right\}^\beta. \tag{4.18}$$

The continuity of the rate of dissipation is ensured as well. As the crystallization process involves phase change, one needs to take into account the rate of entropy production that accompanies the phase change. Accordingly, we define the rate of entropy production (times $\rho\theta$), i.e., ξ_p as $\rho(\Psi_m - \hat{\Psi}_s)\dot{\alpha}$, where $\hat{\Psi}_s$ and $\dot{\alpha}$ are given by the right hand side of Eqs. (4.22) and (4.24) respectively.

Using the procedure developed by Rao and Rajagopal [73], it is straightforward to

show that the stress tensor is given by

$$\begin{aligned} \mathbf{T} = & -p\mathbf{I} + (1 - \alpha) \frac{\mu^m \theta}{\theta_m} \left[1 + \frac{b}{n} (I_{\kappa_{pm}(t)} - 3) \right]^{n-1} \mathbf{B}_{\kappa_{pm}(t)} + \int_{t_o}^t \left\{ \mu_1^s \mathbf{B}_{\kappa_c(\tau)} \right. \\ & \left. + 2\mu_2^s (J_{\kappa_c(\tau)} - 1) \mathbf{F}_{\kappa_c(\tau)} (\mathbf{n}_{\kappa_c(\tau)} \otimes \mathbf{n}_{\kappa_c(\tau)}) \mathbf{F}_{\kappa_c(\tau)}^T \right\} \frac{d\alpha(\tau)}{d\tau} d\tau, \end{aligned} \quad (4.19)$$

and the evolution equation is same as that of Eq. (4.15). The specific internal energy, specific heat capacity of the mixture are given by

$$\begin{aligned} \epsilon = & \alpha \left\{ A^s - B^s \theta_s + \frac{1}{2} c_1^s (\theta^2 - \theta_s^2) + c_2^s (\theta - \theta_s) \right\} + \int_{t_o}^t \left\{ \frac{\mu_1^s}{2\rho} (I_{\kappa_c(\tau)} - 3) \right. \\ & \left. + \frac{\mu_2^s}{2\rho} (J_{\kappa_c(\tau)} - 1)^2 \right\} \frac{d\alpha(\tau)}{d\tau} d\tau + (1 - \alpha) \epsilon_m, \end{aligned}$$

and thus

$$\frac{\partial \epsilon}{\partial \theta} = \alpha (c_1^m \theta + c_2^m) + (1 - \alpha) (c_1^s \theta + c_2^s). \quad (4.20)$$

The criterion that determinates the initiation of crystallization is given by

$$\begin{aligned} & A^m + (B^m + c_2^m)(\theta - \theta_m) - c_1^m \frac{(\theta - \theta_m)^2}{2} - c_2^m \theta \ln \left(\frac{\theta}{\theta_m} \right) + \frac{\mu^m \theta}{2\rho \theta_m b} \left\{ \left[1 \right. \right. \\ & \left. \left. + \frac{b}{n} (I_{\kappa_{pm}(t)} - 3) \right]^n - 1 \right\} - \left\{ A^s + (B^s + c_2^s)(\theta - \theta_s) - c_1^s \frac{(\theta - \theta_s)^2}{2} \right. \\ & \left. - c_2^s \theta \ln \left(\frac{\theta}{\theta_s} \right) \right\} = 0, \end{aligned} \quad (4.21)$$

while the crystallization kinetics is given through

$$\dot{\alpha} = K_o \left\{ \frac{\alpha_o - \alpha}{\alpha_o} \right\} \log \left(\frac{\alpha_o}{\alpha_o - \alpha} \right)^{2/3} \exp \left(\frac{-C_1}{\theta - \theta_c} \right) \exp \left(\frac{-C_2}{\theta(\hat{\Psi}_m - \hat{\Psi}_s)} \right), \quad (4.22)$$

where

$$\begin{aligned} \hat{\Psi}_m = & A^m + (B^m + c_2^m)(\theta - \theta_m) - c_1^m \frac{(\theta - \theta_m)^2}{2} - c_2^m \theta \ln \left(\frac{\theta}{\theta_m} \right) \\ & + C_b \frac{\mu^m \theta}{2\rho \theta_m b} \left\{ \left[1 + \frac{b}{n} (I_{\kappa_{pm}(t)} - 3) \right]^n - 1 \right\}, \end{aligned} \quad (4.23)$$

and

$$\hat{\Psi}_s = A^s + (B^s + c_2^s)(\theta - \theta_s) - c_1^s \frac{(\theta - \theta_s)^2}{2} - c_2^s \theta \ln \left(\frac{\theta}{\theta_s} \right). \quad (4.24)$$

In Eq.(4.22), α_o is the ultimate crystallinity and C_1 , C_2 , K_o and C_b are constants. It is worth observing that Eq. (4.22) has a form that is similar to the Nakamura equation (see Nakamura *et. al.* [44] and Patel *et al.* [49]).

D. Fiber spinning

1. Melt equations

The problem is solved numerically as a one-dimensional radial resolution axisymmetric problem in the melt regime. When crystallization is initiated, for simplicity, in the mixture regime, one-dimensional equations are used with the continuity of velocity, $B(z)$ and the surface temperature as the interfacial conditions. The results are compared with the experimental data obtained by Bheda and Spruiell [4]. The components of the tensors $\mathbf{B}_{\kappa_{p_m(t)}}$ and \mathbf{L} are assumed to be $\text{diag} \left\{ \frac{1}{\sqrt{B(z)}}, \frac{1}{\sqrt{B(z)}}, B(z) \right\}$ and $\text{diag} \left\{ -\frac{1}{2} \frac{dv(z)}{dz}, -\frac{1}{2} \frac{dv(z)}{dz}, \frac{dv(z)}{dz} \right\}$, respectively.

The balance of mass takes the following form:

$$W = \rho \pi R^2 v. \quad (4.25)$$

where W is the mass flow rate of the polymer and R is the radius of the fiber. The temperature is assumed to be a function of r and z in the melt regime. The position of the lateral surface of the fiber is determined as a part of the solution of the problem. The following transformation is used to map the computational domain to that of a rectangle (see chapter 15 of Pearson [51]) via the transformation $\xi = \frac{r}{R(z)}$. Accordingly, on assuming that the Fourier's law of conduction holds, and neglecting

radiation and axial conduction, the balance of energy reduces to

$$\begin{aligned} & \left(c_1^m \hat{\theta}(\xi, z) + c_2^m \right) \frac{\partial \hat{\theta}(\xi, z)}{\partial z} = \frac{\pi k_m}{W} \frac{1}{\xi} \frac{\partial}{\partial \xi} \left(\xi \frac{\partial \hat{\theta}(\xi, z)}{\partial \xi} \right) + \frac{1}{\rho v} \frac{\mu_m \hat{\theta}(\xi, z)}{\theta_m} \left\{ 1 + \frac{b}{n} \right. \\ & \times \left. \left(\frac{2}{\sqrt{B(z)}} + B(z) - 3 \right) \right\}^{n-1} \left(B(z) - \frac{1}{\sqrt{B(z)}} \right) \frac{dv}{dz}. \end{aligned} \quad (4.26)$$

The heat transfer coefficient in $W/m^2/^\circ K$, h , is given by (see Bheda and Spruiell [4]; the correlation is given in *cgs* units)

$$h = 1.0371(v(z)/A(z))^{0.287}, \quad (4.27)$$

where v and area of the cross section of the fiber, A are in SI units.

The averaged value of any quantity ϕ is represented as $\bar{\phi}$ and is defined through

$$\bar{\phi}(z) = 2 \int_0^1 \xi \phi(\xi, z) d\xi. \quad (4.28)$$

It is obvious that if ϕ is only a function of z , then $\phi = \bar{\phi}$. The averaged momentum balance equation, assuming $T_{rr} = T_{\theta\theta}$, is (see Vassilatos *et al.* [82])

$$\frac{dv}{dz} = \frac{d}{dz} \left\{ \frac{1}{\rho v} \left[(\bar{T}_m)_{zz} - (\bar{T}_m)_{rr} \right] \right\} - \frac{\pi \rho_a R v^2 C_d}{W} + \frac{\pi \rho R^2 g}{W}, \quad C_d = 0.37 \left\{ \frac{v(z) d(z) \rho_a}{\eta_a} \right\}^{-0.61}, \quad (4.29)$$

where

$$(\bar{T}_m)_{zz} - (\bar{T}_m)_{rr} = \frac{\mu_m \bar{\theta}(z)}{\theta_m} \left\{ 1 + \frac{b}{n} \left(\frac{2}{\sqrt{B(z)}} + B(z) - 3 \right) \right\}^{n-1} \left(B(z) - \frac{1}{\sqrt{B(z)}} \right). \quad (4.30)$$

The correlation for coefficient of drag, C_d , is taken from Matsui [37]. The averaged evolution equation, on suppressing the arguments, is

$$\begin{aligned} \frac{dB}{dz} &= 2 \frac{dv}{dv} \frac{B}{v} + \frac{2}{v} \left\{ \frac{1}{2} \frac{\mu^m}{\theta_m} \left[1 + \frac{b}{n} \left(\frac{2 + B^{3/2}}{\sqrt{B}} - 3 \right) \right] \right\}^{n-1} \\ &\times \left[\frac{2 + B^{3/2}}{\sqrt{B}} - \frac{9B}{2B^{3/2} + 1} \right]^{1-\beta} \left\{ \frac{1}{2\beta-1} \left\{ \frac{3B}{2B^{3/2} + 1} - B \right\} 2 \int_0^1 \xi \left(\frac{\hat{\theta}}{\nu^m} \right)^{\frac{1}{2\beta-1}} d\xi, \right. \\ \nu^m &= \nu_0^m \exp \left(C \left[\frac{1}{\hat{\theta}} - \frac{1}{\theta_r} \right] \right). \end{aligned} \quad (4.31)$$

2. Mixture equations

For simplicity, all the variables in the mixture regime are assumed to be function of z only. The components of the tensors $\mathbf{B}_{\kappa_{p_m(t)}}$ and \mathbf{L} are the same as that in the previous section. The mass balance equation is the same as that given by Eq. (4.25). For the solid born at time τ , using the components of the velocity gradient tensor, it follows that the components of $\mathbf{B}_{\kappa_{c(\tau)}}$, $t_o \leq \tau \leq t$, where t_o is the time at which crystallization process is initiated, are $\text{diag} \left\{ \frac{v(\tilde{z})}{v(z)}, \frac{v(\tilde{z})}{v(z)}, \frac{v(z)^2}{v(\tilde{z})^2} \right\}$. The normal component of the stress tensor in the z-direction is given by

$$\begin{aligned} T_{zz} - T_{rr} &= \int_{z_o}^z \left\{ \mu_1^s \frac{v(z)^2}{v(\tilde{z})^2} + 2 \mu_2^s \frac{v(z)^2}{v(\tilde{z})^2} \left(\frac{v(z)^2}{v(\tilde{z})^2} - 1 \right) - \mu_1^s \frac{v(\tilde{z})}{v(z)} \right\} \frac{d}{d\tilde{z}} \alpha(\tilde{z}) d\tilde{z} + (1 - \alpha(z)) \\ &\times \frac{\mu_m \theta(z)}{\theta_m} \left\{ 1 + \frac{b}{n} \left(\frac{2}{\sqrt{B(z)}} + B(z) - 3 \right) \right\}^{n-1} \left(B(z) - \frac{1}{\sqrt{B(z)}} \right). \end{aligned} \quad (4.32)$$

The averaged balance of linear momentum equation can be obtained by substituting the Eq. (4.32) in the Eq. (4.29).

The evolution equation, on using Eq. (4.15) and the appropriate components of the

tensors $\mathbf{B}_{\kappa_{pm}(t)}$ and \mathbf{L} reduce to

$$\begin{aligned} \frac{dB}{dz} &= 2 \frac{dv}{dv} \frac{B}{v} + \frac{2}{v} \left\{ \frac{1}{2} \frac{\mu^m \theta}{\nu^m \theta_m} \left[1 + \frac{b}{n} \left(\frac{2 + B^{3/2}}{\sqrt{B}} - 3 \right) \right] \right\}^{n-1} \\ &\times \left[\frac{2 + B^{3/2}}{\sqrt{B}} - \frac{9B}{2B^{3/2} + 1} \right]^{1-\beta} \left\{ \frac{1}{2\beta-1} \left\{ \frac{3B}{2B^{3/2} + 1} - B \right\} \right\}, \\ \nu^m &= (1 - \alpha) \nu_0^m \exp \left(C \left[\frac{1}{\hat{\theta}} - \frac{1}{\theta_r} \right] \right) + \alpha \nu_0^s. \end{aligned} \quad (4.33)$$

The energy equation, on substituting for the components of the tensors $\mathbf{B}_{\kappa_{pm}(t)}$ and \mathbf{L} , reduces to

$$\begin{aligned} \rho \{ (1 - \alpha)(c_1^m \theta + c_2^m) + \alpha(c_1^s \theta + c_2^s) \} v \frac{d\theta}{dz} &= (1 - \alpha) \frac{\mu_m \theta}{\theta_m} \left\{ 1 + \frac{b}{n} \left(\frac{2}{\sqrt{B(z)}} \right. \right. \\ &+ B(z) - 3 \left. \left. \right\}^{n-1} \left(B(z) - \frac{1}{\sqrt{B(z)}} \right) \frac{dv}{dz} - \frac{h}{d} (\theta - \theta_\infty) + \rho \left\{ A^m - B^m \theta_m \right. \right. \\ &+ \frac{1}{2} c_1^m (\theta^2 - \theta_m^2) + c_2^m (\theta - \theta_m) - \left. \left. \left(A^s - B^s \theta_m + \frac{1}{2} c_1^s (\theta^2 - \theta_s^2) + c_2^s (\theta - \theta_s) \right) \right\} \right. \\ &\times \frac{d\alpha}{dz} v. \end{aligned} \quad (4.34)$$

The crystallization kinetics is given through the Eqs. (4.22)-(4.24) with $I_{\kappa_{pm}(t)}$ being replaced by $\frac{2 + B^{3/2}}{\sqrt{B}}$ and the birefringence, Δn , is calculated through (see Patel et al. [49]):

$$\Delta n = (1 - \alpha) C_{op} [(\bar{T}_m)_{zz} - (\bar{T}_m)_{rr}] + \alpha f_c \Delta_c, \quad (4.35)$$

where $(\bar{T}_m)_{zz} - (\bar{T}_m)_{rr}$ is given by the Eq. (4.30). One can arrive at an expression for the birefringence by considering the interaction of the electromagnetic waves with matter. Instead, for simplicity, we use the above formula. In the semi-crystalline regime, the contribution to the birefringence is assumed to be the sum of birefringence of the stressed amorphous phase and the crystalline phase weighted by their respective mass fractions. In the mixture regime, recalling that the temperature is assumed to be a function of z , for the calculation of the stress in the amorphous phase, the term

$\bar{\theta}$ in the Eq. (4.30) is replaced by $\theta(z)$.

3. Boundary, initiation and interface conditions

The appropriate boundary conditions for the thin-filament approximation are as follows: The velocity at $z = 0$ can be computed using the capillary diameter and averaged mass balance. The temperature of the melt exiting the capillary and take up velocity are also known. These three pieces of information form the boundary conditions for the problem. The traction boundary condition on the free surface of the fiber due to air drag does not appear explicitly as a boundary condition, however it is incorporated into the linear momentum balance as a result of the averaging process employed during thin-filament approximation (one-dimensional) of the fiber spinning process (see Pearson [51]). A similar averaging procedure with respect to the energy balance, assuming Fourier heat conduction for the heat flux, with convective boundary condition on the free surface yields the averaged energy balance. If at some distance along the spinneret Eq. (4.21) is satisfied, then this point marks the initiation of crystallization. The continuity of the velocity, $B(z)$ and temperature across the initiation point separating the melt and mixture regime with $\alpha = 0$ on this interface are the interfacial conditions.

The boundary conditions that are appropriate with the radial resolution approximation are as follows. A uniform temperature of $553^\circ K$ is assumed at the exit of the spinneret because no other information is available that can be used in with respect to the temperature distribution at $z = 0$. Symmetry of the temperature condition is imposed at $\xi = 0$, i.e., $\frac{\partial \hat{\theta}}{\partial \xi} = 0$. The convection boundary condition is imposed on the lateral surface, i.e., it is assumed that $-\frac{k_m}{R} \frac{\partial \hat{\theta}}{\partial \xi} = h(\hat{\theta} - \theta_\infty)$ at $\xi = 1$. The velocity with which the melt is extruded from the spinneret at $z = 0$ is calculated using the

mass balance equation (4.25). The take-up velocity (at $z = 2$) is also known. The continuity of v , B and the surface temperature across the interface serve as the interfacial conditions. Recall that the temperature is assumed to be a function of ξ and z in the melt regime and for simplicity it is assumed to be a function of only z in the mixture regime. Since v and B are treated only as a function of z , the initiation criterion, Eq. (4.21), needs to be averaged, i.e.,

$$\int_0^1 \xi \left\{ \begin{aligned} & A^m + (B^m + c_2^m)(\hat{\theta} - \theta_m) - c_1^m \frac{(\hat{\theta} - \theta_m)^2}{2} - c_2^m \hat{\theta} \ln \left(\frac{\hat{\theta}}{\theta_m} \right) + \frac{\mu^m \hat{\theta}}{2\rho\theta_m b} \left\{ \left[1 \right. \right. \\ & + \left. \left. \frac{b}{n} \left(\frac{2 + B^{3/2}}{\sqrt{B}} - 3 \right) \right]^n - 1 \right\} - \left\{ A^s + (B^s + c_2^s)(\hat{\theta} - \theta_s) - c_1^s \frac{(\hat{\theta} - \theta_s)^2}{2} \right. \\ & \left. \left. - c_2^s \hat{\theta} \ln \left(\frac{\hat{\theta}}{\theta_s} \right) \right\} \right\} d\xi = 0. \end{aligned} \right. \quad (4.36)$$

4. Parameters

a. Thin-filament approximation

If one has the raw data from capillary rheometry of polymer melts (wall shear rate, pressure gradient and other geometric parameters of the capillary tube) at a few different temperatures, then one could determine ν_o^m , C , μ^m , b , n and β . Here ν_o^m assumes a larger value as the molecular weight of polymer melt increases (same qualitative trend as the correlation of zero shear viscosity of Doufas *et al.* [15]). For other material properties such as specific heat capacity and density we used the values provided in Doufas *et al.* [14] and Doufas *et al.* [15] (see Tables III and IV). The specific latent energy of crystallization is given by $A^m - B^m\theta_m + \frac{1}{2}c_1^m(\theta^2 - \theta_m^2) + c_2^m(\theta - \theta_m) - (A^s - B^s\theta_m + \frac{1}{2}c_1^s(\theta^2 - \theta_s^2) + c_2^s(\theta - \theta_s))$. The specific latent energy can be rearranged to be of the form given in Eq. (36) of Doufas *et al.* [14] and thus we find that $A^m - B^m\theta_m - \frac{1}{2}c_1^m\theta_m^2 - c_2^m\theta_m - (A^s - B^s\theta_m - \frac{1}{2}c_1^s\theta_s^2 - c_2^s\theta_s)$ is the expression which has been referred to as the reference heat of fusion, which has a value of 50 cal/g for

nylon (see Doufas *et al.* [14]). We determine B^s from the same expression knowing the other parameters appearing in it. The exponent m was chosen to be unity and the ultimate crystallinity α_o is 0.3 (see Doufas *et al.* [15]). As the value of the parameter C_b is increased, the predicted temperature of the fiber during crystallization increases (since it is an exothermic process). Care should be exercised in choosing C_b and the other relevant parameters such that the rate of entropy production due to crystallization is non-negative. Since the temperature data during crystallization is not available, the parameter C_b cannot be determined precisely and hence we pick it such that the rate of entropy production due to crystallization is non-negative.

The different tests are labelled S1-S20 and the precise conditions under which the tests were carried out are listed in Table II, which is a reproduction of the processing conditions listed in Table (1) of Doufas *et al.* [15]). It is important to note that, for a set of experiments, the material parameters are fixed with respect to one experiment and the results for the other experiments are predicted on the basis of the model fixed with the first experiment. For example, for the tests S12-S14, the material parameters are determined using S12 and the tests S13 and S14 are predicted on the basis of the parameters fixed by S12. Various nylons spun in such experiments are homopolymer nylons of different molecular weights with and without additives and a copolymer.

For the details regarding the nylons used and their material properties, we refer the reader to Doufas *et al.* [14] and [15]. The value of C_b , for example, for the test S6 and S10 are 52 and 48, respectively. The crystalline orientation function f_c is taken to be 0.9 and the intrinsic crystalline birefringence, assumed to be a constant, is determined from the peak birefringence data of the tests S6 and S10 to be 0.105 and 0.093, respectively. Doufas *et al.* [15] determined both the melt orientation factor (instead of using C_{op}) and semicrystalline orientation factor from microstructural tensors.

For the tests S6-S8 only A^m is different while for S9-S11 A^m and C_b are different. For the tests S15-S20, the same set of material parameters are used.

Table II. Processing conditions for various nylons from Doufas *et al.* [15]

Test	d_o (mils)	v_t (m/min)	W (g/min)	θ_o (°C)	L (cm)	z_1 (cm)	z_2 (cm)	v_c (ft/min)	θ_∞ (°C)
S1	8.5	5700	2.22	290	160	4	116	60	21
S2	8.5	5700	2.22	290	160	4	116	100	21
S2	8.5	5700	2.22	290	160	4	116	140	21
S4	8.5	5300	2.265	287	160	4.2	116.8	75	21
S5	14	5300	2.265	287	160	4.2	116.8	75	21
S6	13	5100	1.94	279.7	200	3.5	100	68.9	14.5
S7	13	5100	1.94	279.7	200	3.5	100	68.9	16
S8	13	5100	1.94	280.3	200	3.5	100	68.9	14.5
S9	13	5100	1.94	280.6	200	3.5	100	68.9	14.5
S10	13	5100	1.94	279	200	3.5	100	68.9	15.4
S11	13	5100	1.94	280.6	200	3.5	100	68.9	15.5
S12	15	1006	1.42	277	300	0.0	143	66.8	11.1
S13	15	396	2.85	299	300	0.0	300	94.2	11.1
S14	13	396	1.43	298	300	0.0	300	94.2	11.1
S15	10	5300	1.902	287	135	4.5	116	60	24
S16	10	5300	2.038	287	135	4.5	116	60	24
S17	10	5300	2.265	287	135	4.5	116	60	24
S18	10	5300	2.492	287	135	4.5	116	60	24
S19	10	5300	2.627	287	135	4.5	116	60	24
S20	10	5300	2.944	287	135	4.5	116	60	24

Table III. Parameters that are fixed in all the simulations

Parameter(s)	Numerical value	Reference
Density of air, ρ_a	1.2 Kg/m^3	[84]
Viscosity of air, η_a	1.8x10 ⁻⁵ $Pa\cdot s$	[84]
Ultimate crystallinity fraction (by weight), α_o	0.3	[15]
Material constant of the melt, μ^m	1000 Pa	
Material constant associated with the melt, b	1	
Power law index associated with the melt, n	8	
Power law index associated with the melt, β	0.8	
Reference temperature of the melt, θ_m	350° K	
Reference temperature in the Eq. (4.12), θ_r	560° K	
Other material constants associated with the melt, B^m	20.83 $J/Kg^\circ K$	
Reference temperature associated with the solid, θ_s	390° K	
Material moduli associated with the solid, μ_1^s and μ_2^s	0.2x10 ⁹ Pa and 0.45x10 ⁹ Pa	
Constant appearing in Eq. (4.12), ν_o^s	1x10 ⁸ $Pa\cdot s$	
Constants associated with the crystallization equation, K_o , C_1 and C_2	3x10 ⁶ s^{-1} , 590° K and 9.5x10 ¹⁰ $J^\circ K/Kg$	
The constant appearing in Eq. (4.6), θ_c	284° K	
Other material constants associated with the solid, A^s	393.2 J/Kg	
Stress optical coefficient, C_{op}	1.2x10 ⁻⁹ m^2/N	

Table IV. Parameters that are dependent on simulation

Test	$\nu_o^m (PaS^{2\beta-1})$	$C (^{\circ}K)$	$A^m (J/Kg)$
S1-S3	130	5800	19000
S4-S5	165	6100	21000
S6-S7	90	6950	19800
S8	90	6950	21500
S9	110	6950	8000
S10	110	6950	30500
S11	110	6950	23000
S12-S14	175	5500	20000
S15-S20	170	5500	21000

b. Radial resolution approximation

The following table, i.e., Table V, lists the parameters used during simulation using radial resolution approximation.

Table V. The parameters used in the simulation.

Parameter(s)	Numerical value	Reference
Length of the spinline	2 <i>m</i>	[4]
Diameter of the spinneret	0.000762 <i>m</i>	[4] and [34]
Density of air, ρ_a	1.2 <i>Kg/m³</i>	[84]
Viscosity of air, η_a	1.8x10 ⁻⁵ <i>Pas</i>	[84]
Extrusion temperature of the melt	553° <i>K</i>	[4]
Ambient temperature	298° <i>K</i>	[4] and [34]
Density of nylon 6	1132 <i>Kg/m³</i>	[34]
Specific heat capacity constants of the Eq. (4.20)	$c_1^m = c_1^s =$ 1.3522 <i>J/Kg⁰K²</i>	
	$c_2^m = c_2^s =$ 1984.5 <i>J/Kg⁰K</i>	[20]
Thermal conductivity of the melt	0.2 <i>W/m^oK</i>	[78]
Ultimate crystallinity fraction (by weight), α_o	0.487	[49] and [34]
Material modulus of the melt, μ^m	1000 <i>Pa</i>	
Material constant associated with the melt, b	1.56	
Power law index associated with the melt, n	8.3	
Power law index associated with the melt, β	0.955	
Reference temperature of the melt, θ_m	354.4° <i>K</i>	
Reference temperature in the Eq. (4.31), θ_r	553° <i>K</i>	
Viscosity of the melt at θ_r , ν_o^m	80 <i>Pas</i>	

Table V. continued.

Exponential constant in the Eq. (4.31), C	$4950^\circ K$	
Other material constants associated with the melt, A^m and B^m	$4500 J/Kg$ and $85.83 J/Kg^\circ K$	
Reference temperature associated with the solid, θ_s	$390^\circ K$	
Material moduli associated with with the solid, μ_1^s and μ_2^s	$1 \times 10^9 Pa$ and $2 \times 10^9 Pa$	[34]
Constant appearing in Eq. (4.33), ν_o^s	$1 \times 10^8 Pas$	
Constants associated with the crystallization equation, K_o , C_1 , C_2 , and C_b	$5 \times 10^6 s^{-1}$, $590^\circ K$, $1 \times 10^{11} J^\circ K/Kg$ and 50	
The constant appearing in Eq. (4.22), θ_c	$283^\circ K$	[49]
Other material constants associated with the solid, A^s and B^s	$393.2 J/Kg$ and $100.26 J/Kg^\circ K$	
Stress optical coefficient, C_{op}	$1.2 \times 10^{-9} m^2/N$	[49]
Crystalline orientation factor and intrinsic crystalline birefringence, f_c and Δ_c	0.9 and 0.082	[49] and [43]

We use the same constants associated with the specific heat of the melt and the mixture (see Eqs. (4.16) and (4.20) as that used by Gaur et al. [20] above the glass transition temperature ($313^\circ K$); below the glass transition temperature the constants associated with the specific heats show a significant departure from the corresponding constants above glass transition temperature. For the problem under consideration,

the temperature is always above the glass transition temperature. Referring to the Eq. (4.34), $A^m - B^m\theta_m + \frac{1}{2}c_1^m(\theta^2 - \theta_m^2) + c_2^m(\theta - \theta_m) - (A^s - B^s\theta_m + \frac{1}{2}c_1^s(\theta^2 - \theta_s^2) + c_2^s(\theta - \theta_s))$ represents latent energy of crystallization/fusion per unit mass. In general, this term is dependent on the temperature, but for $c_1^m = c_1^s$ and $c_2^m = c_2^s$ the specific latent energy is a constant, i.e., $A^m - B^m\theta_m - \frac{1}{2}c_1^m\theta_m^2 - c_2^m\theta_m - (A^s - B^s\theta_m - \frac{1}{2}c_1^s\theta_s^2 - c_2^s\theta_s)$. For the semi-crystalline material under consideration, the latent energy of fusion is approximately 1×10^5 J/Kg (see Wunderlich [86]). The constants A^m , B^m , A^s , B^s , θ_m and θ_s are chosen in such a way that the specific latent energy of fusion is 1×10^5 J/Kg. The material moduli μ_1^s and μ_2^s are of the order of a few Gpa (see Koyama *et al.* [34]). That crystallization occurs after the development of the neck (see Haberkorn *et al.* [27]), was confirmed by laser light scattering and WAXS for polyamides. In keeping with this observation, the initiation criterion (4.36) is such that the crystallization is triggered almost at the end of neck formation. The initiation of crystallization of nylon 6 (Patel and Spruiell [50]) as inferred from the crystallization data indicates that it depends on the cooling rate (the material is not deformed) as opposed to a equilibrium melting temperature at which the crystallization is initiated irrespective of the cooling rate. One may refer to Choi and White [8] for the former interpretation. However, for simplicity, the cooling rate effect is not included in the equation for the initiation criterion (only the effect of temperature and deformation is included in the Eq. (4.21)) and hence the data provided by Patel and Spruiell [50] is not used. Instead, the constants associated with the crystallization and initiation equations are chosen to fit the spinline data provided by Bheda and Spruiell [4] with the crystallization temperature determined by the Eq. (4.36). There is evidence for the presence of (see Koyama *et al.* [34]) α and γ phase. The intrinsic birefringence of the α and the monoclinic γ crystals was calculated by Murase *et al.* [43] to be 0.097 and 0.066. Since the fraction of both the crystal forms are not known for the take up speed of

6660 m/min where the crystallization is profuse, average of the intrinsic birefringence of both the crystal forms is used in the simulation.

5. Numerical method

For the thin-filament approximation, the two sets of equation for the melt and the mixture regime (after being converted into a system of odes) are solved using a stiff equation solver employing shooting technique.

The radial resolution approximation of fiber spinning was solved with the aid of Matlab using a pde solver with a guess for $v(z)$, $B(z)$ and $\frac{dv}{dz}$ using the appropriate boundary conditions: we guess values for v and B at discrete points along the spinline and cubic splines (piece-wise polynomials of third degree whose value for the function, first and the second derivatives are continuous in the entire region of interest) are fitted through these points. The solver interpolates at many points based on the specified tolerance. The entire problem is first solved by assuming v , B , θ and α as functions of z using the appropriate boundary, interface and initiation conditions using a stiff equation solver. The solution thus obtained for v , B and $\frac{dv}{dz}$ for the melt regime alone is used as the initial guess for the energy equation (4.26).

The integrals are evaluated using a adaptive quadrature function. The integrand in the Eqs. (4.29) and (4.31), for each z , is evaluated using the solution obtained from the energy balance equation (4.26) and the integrals are computed after fitting the integrand with cubic splines. The derivative of $\bar{\theta}$ that appear in the momentum balance equation (4.29) is obtained by fitting a cubic spline for $\bar{\theta}$ as a function of z and then by differentiating the spline. The equations (4.29) and (4.31) are solved using a stiff solver by assigning the exit velocity of the melt from the spinneret and a guess for B at $z = 0$ as boundary conditions. The new $v(z)$, $B(z)$ and $\frac{dv}{dz}$ obtained is updated and the Eq. (4.29) is solved once again. This procedure is repeated until

Φ becomes small ($\leq 10^{-5}$), where

$$\Phi = 100 \sum_{j=1}^n \left| \frac{v^{i+1}(z_j) - v^i(z_j)}{v^i(z_j)} \right| + \left| \frac{B^{i+1}(z_j) - B^i(z_j)}{B^i(z_j)} \right|, \quad (4.37)$$

and i is the iteration number; Φ represents the sum of the absolute value of percentage change of v and B between successive iterations at all z_j . The position along the spinline at which the initiation of crystallization occurs is determined using Eq. (4.36); the initiation criterion being only a function of z . Thus the position is varied while iterating between the ode's and pde until the Eq. (4.36) is met.

The mixture equations are a system of integro-differential equations defined on the remaining length of the spinline. This system is converted to a system of first order equations and solved with a stiff differential equation solver using the interfacial conditions. The velocity at $z = 2$ (take-up velocity) is checked against the desired take-up velocity. The boundary condition $B(0)$ is adjusted and the above mentioned procedure is repeated until the desired take-up velocity is achieved.

Since the rate of entropy production due to phase change is non-negative, $\Psi_m - \hat{\Psi}_s \geq 0$.

This constraint is satisfied in all the simulations.

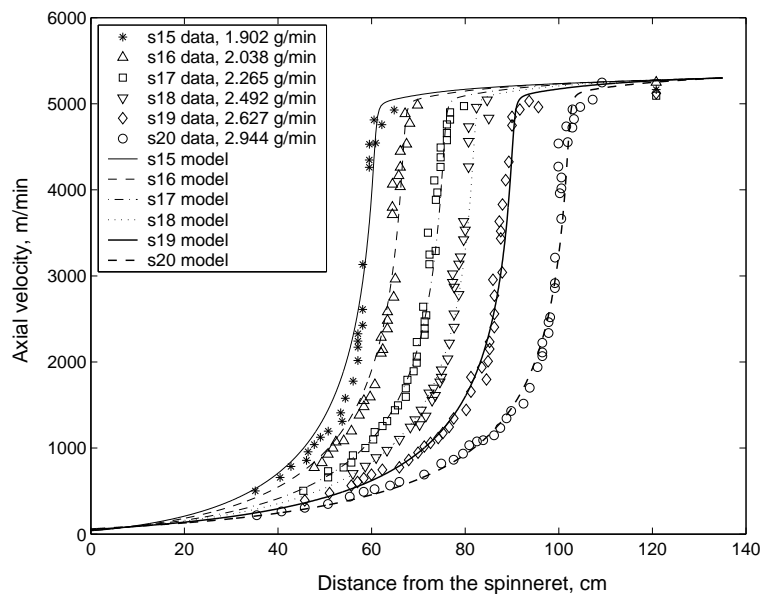
E. Results

1. Thin-filament approximation

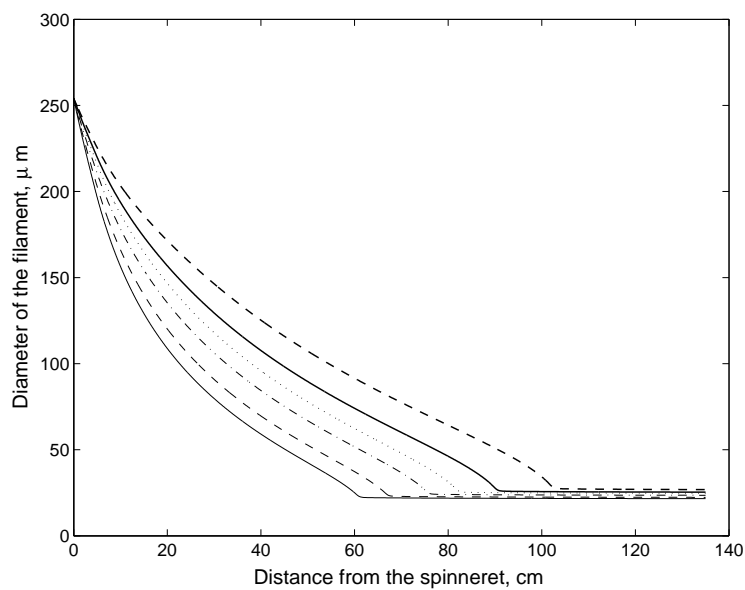
a. Effect of mass flow rate

For the experiments designated as S15-S20 (see Doufas *et al.* [15]), the data was obtained from filaments a few rows behind the quench screen in a commercial multi-filament spinning machine. The position of the neck point, where rapid diameter attenuation takes place, could differ by more than 10 cm compared to the filaments in the first row. This fact indicates that as the material and processing conditions

are fixed, heat transferred by the quench air of fixed speed at the source is different from the first and the last row. Since the temperature was measured, one could use this information to guide one concerning the nature of the heat transfer so that the predicted temperature is close to that which is measured. In our simulations, we fix the heat transfer coefficient given in (4.14) so that the velocity and temperature profiles can be matched, i.e., the heat transfer coefficient is modified for the different experiments. **All the other parameters are fixed.** On the other hand, Doufas *et al.* [15] fixed the heat transfer coefficient but changed the material parameters: *”Although profiles for these filaments differed considerably from those closer to the screen (differences as large as tens of degrees in the temperature profiles, and more than 10 cm in the location of the neck point), in the simulations, quench conditions for the exit of the screen were used. As a result, the model parameters for the same nylon (homopolymer of 70 RV) had to be changed for the different tests in order to fit the experimental velocity profiles (see Table (3) of Doufas et al. [15]).”* The crystallization process is initiated at almost the same temperature independent of mass flow rates (see Haberkorn *et al.* [27]). Fig. (18) shows very good agreement with the experimental data. In Fig. (18b) necking can be easily spotted and in Fig. (18d) a rapid increase in the stress corresponding to necking is also apparent.

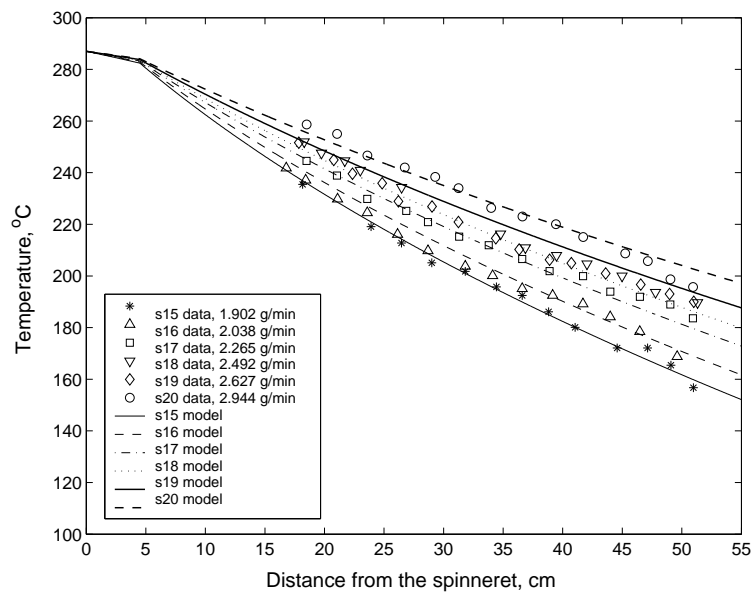


(a)

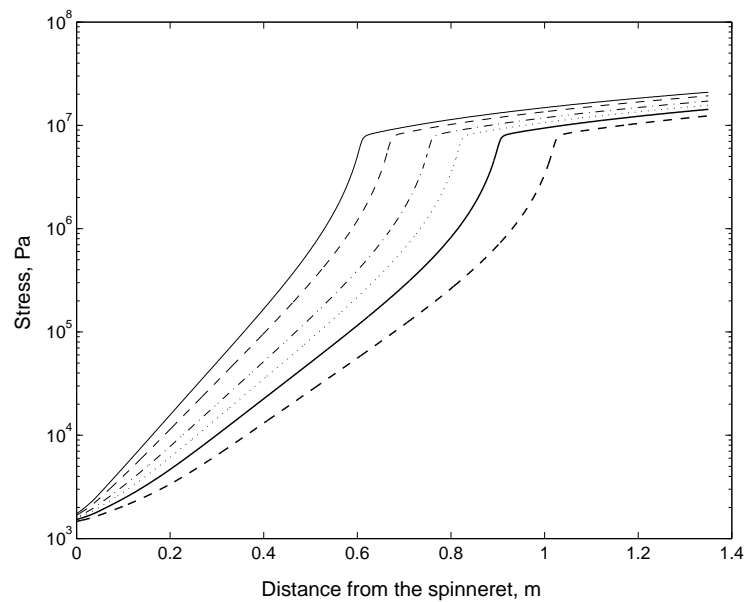


(b)

Fig. 18. Legends for the Figs. (b) and (d) indicating appropriate predictions of the model are the same as that of Figs. (a) or (c). These figures show the effect of mass flow rate.



(c)

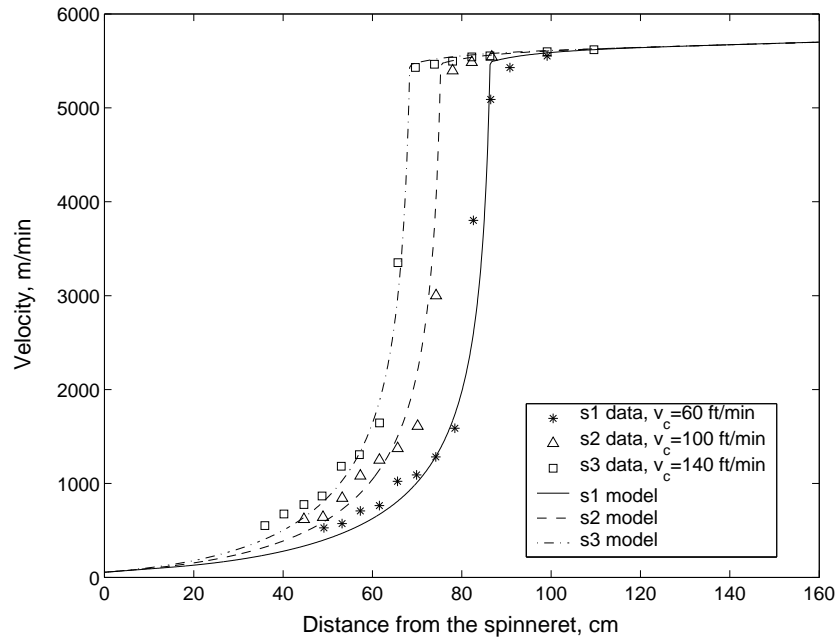


(d)

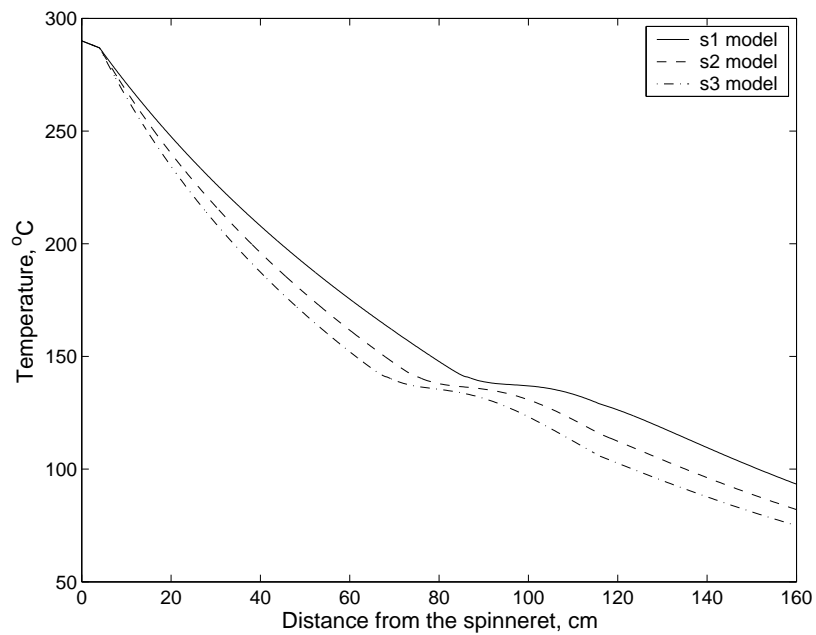
Figure 18 continued

b. Effect of quench air speed

The correlation in Eq. (4.14) was obtained by fitting the velocity profiles in Fig. (19a) so that the effect of quench air speed can be quantified in the correlation. The faster the quench air speed the closer to the spinneret is the neck region. The same correlation was used in all the simulations given in Figs. (20)-(24). The plateau in the temperature profile of Fig. (19b) corresponds to the crystallizing region. As the Fig. (19c) is related to rate of entropy production due to crystallization, the difference in Helmholtz potential of the melt and crystal during crystallization must be non-negative. This condition is checked *a posteriori* in all the simulations.

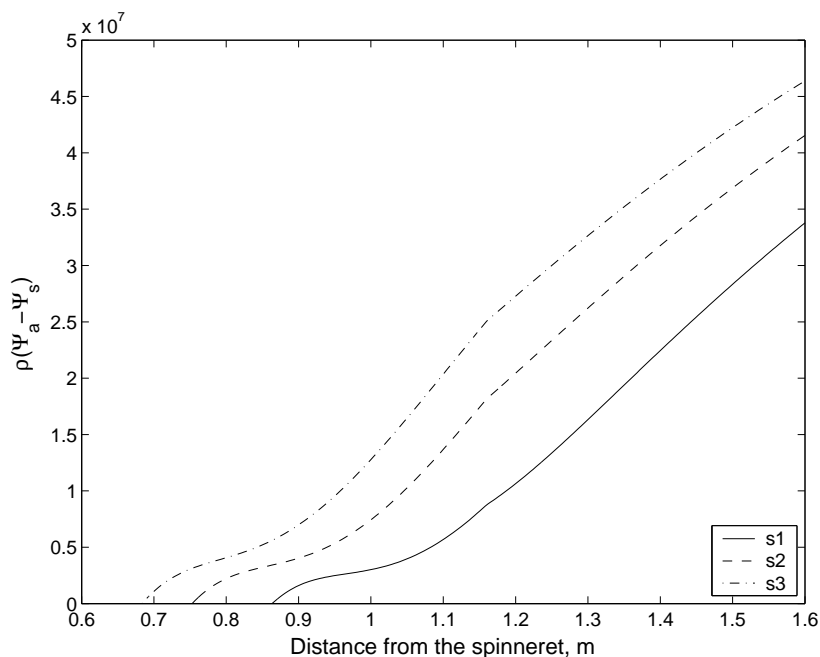


(a)



(b)

Fig. 19. The effect of quench air speed.

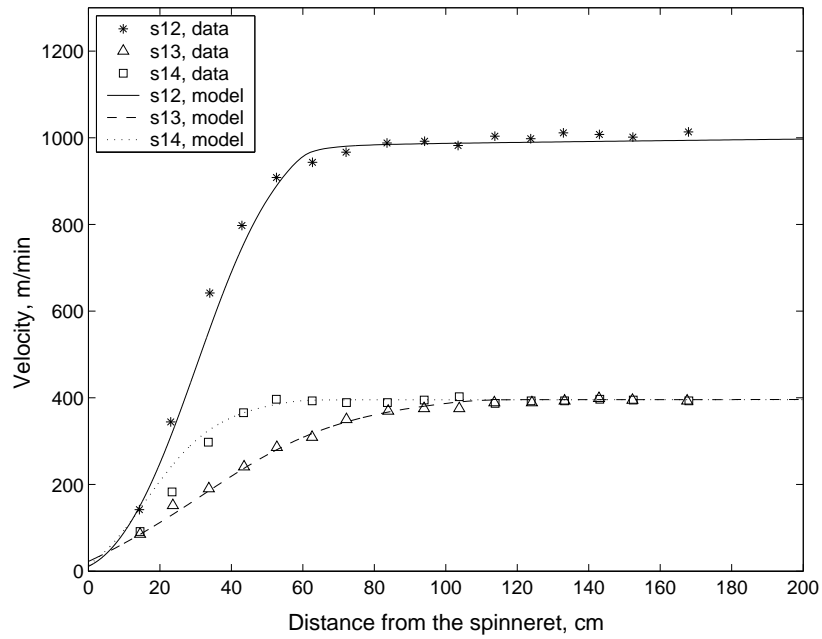


(c)

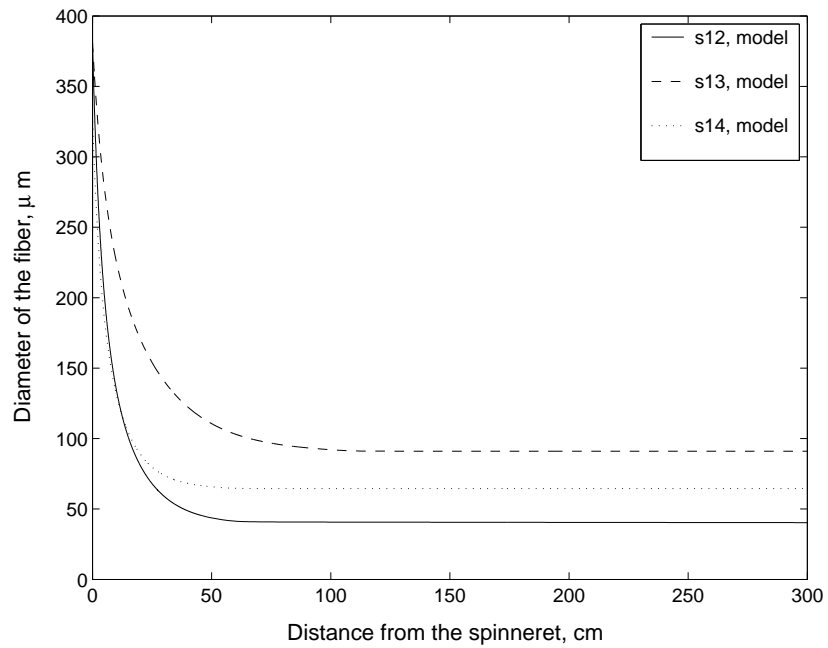
Figure 19 continued

c. Low speed spinning

The adjustable parameters are obtained by fitting the velocity profile of test S12 as shown in Fig. (20a) using the correlation of Eq. (4.14). Using the same parameters, the tests S13 and S14 were predicted. The Fig. (20c) shows the predicted temperature profile. The diameter does not show any necking behavior (see Fig. (20b)) as is to be expected of low speed conditions. The predicted crystallinity, as expected, is the smallest amongst all the simulations. Again the predictions agree very well with the experiments.

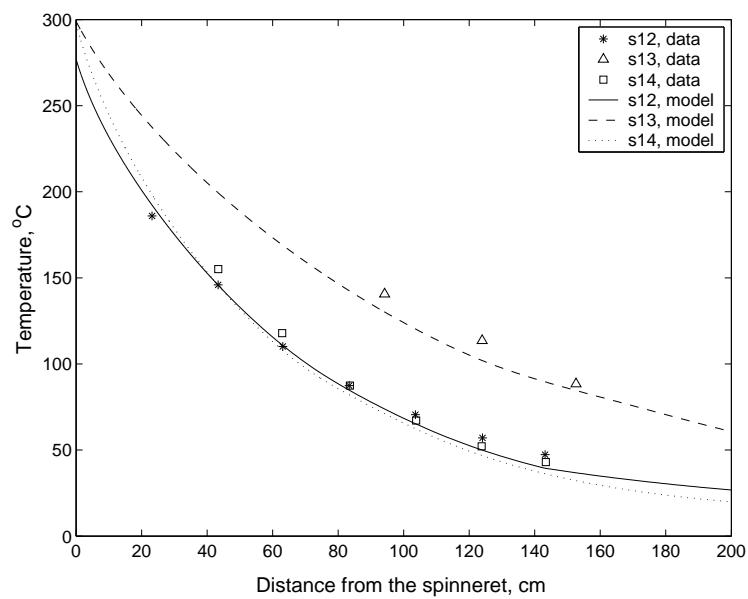


(a)

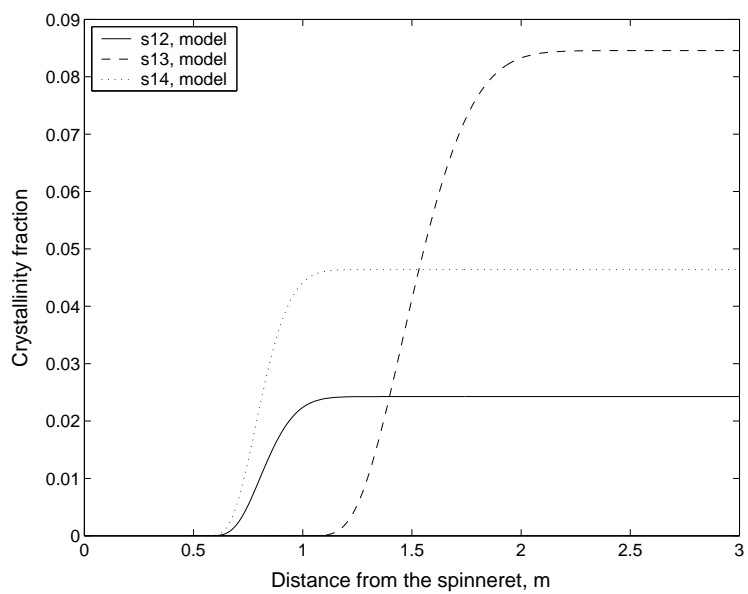


(b)

Fig. 20. Low speed spinning.



(c)

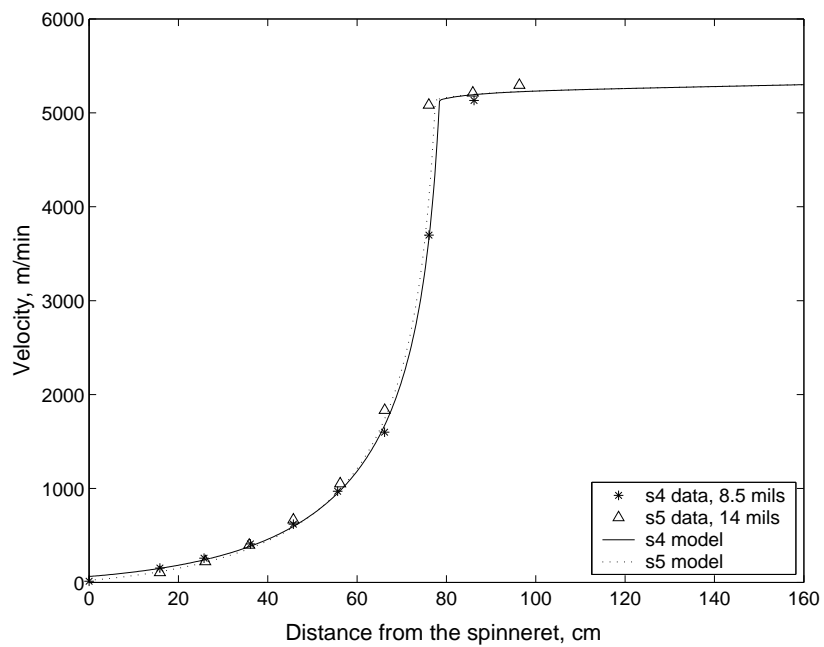


(d)

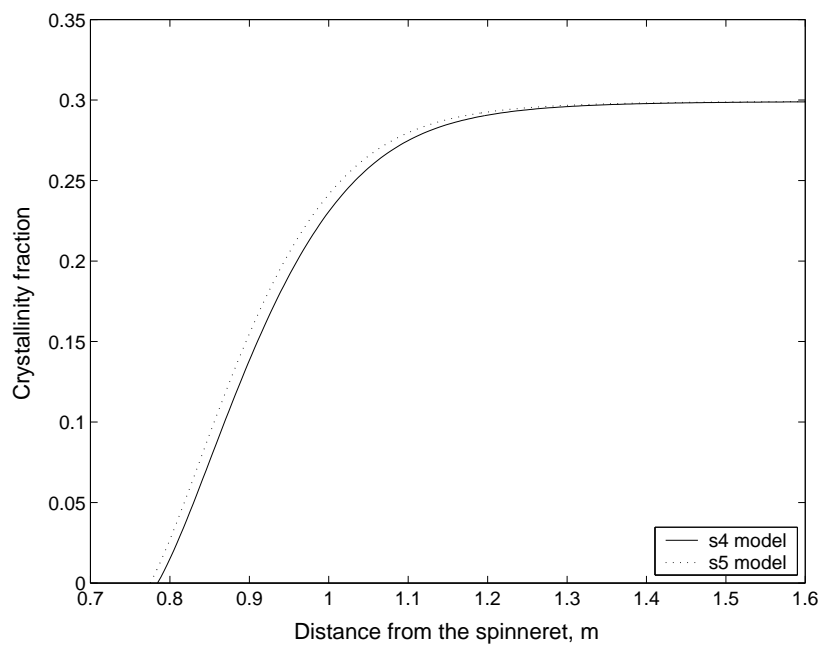
Figure 20 continued

d. Effect of capillary diameter

S4 data was used to obtain the adjustable parameters and S5 was predicted with the same parameters. As the diameter increases, the position of neck point moves closer to the spinneret because the surface area available for heat transfer increases. Figs. (6a) and (6b) show that the predictions of the model agree very well with the experimental results.



(a)

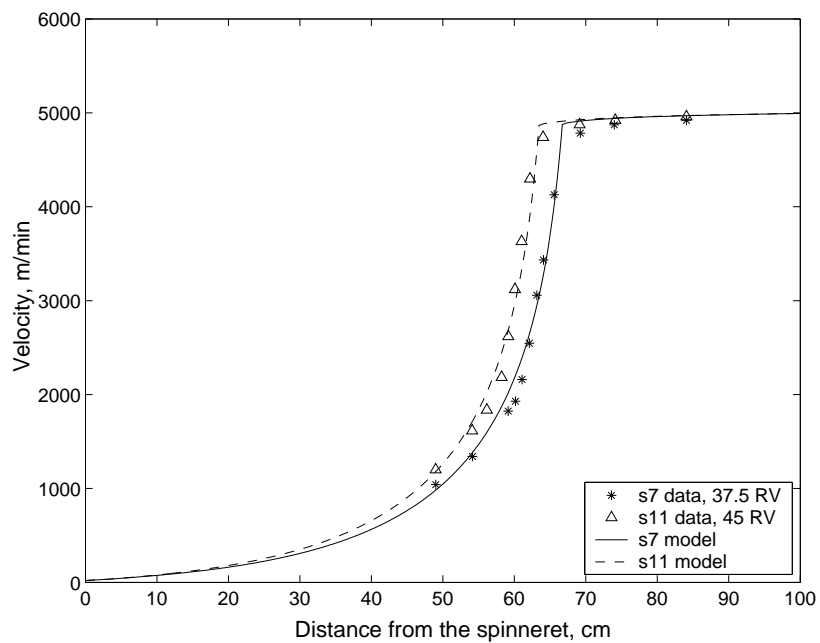


(b)

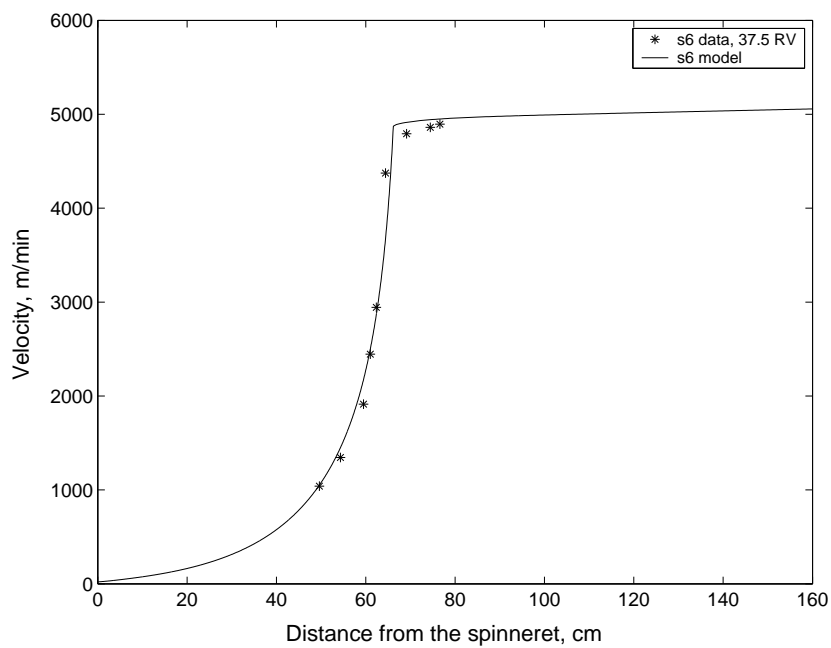
Fig. 21. The effect of changing capillary diameter.

e. Effect of molecular weight

[H] We find that the higher the molecular weight, for the same repeating unit and processing conditions, the larger the temperature at which crystallization is initiated (see Fig. (22a)). The same effect is also manifested in the case of nylon 6 (Koyama *et al.* [34]). The parameter A^m , enables us to change the temperature at which crystallization is initiated. This parameter is increased to move the freeze point closer to the spinneret and thus capture the effect of molecular weight towards initiation of crystallization. Also, the parameter ν_o^m is increased to allow for the increase in the viscosity of the S11 sample compared to the S7 sample. The same material parameters as that used in the case of S7 is used for S6 for predicting the velocity. The parameter C_b , which controls the extent to which the deformation increases the rate of crystallization, is determined so that birefringence data of Fig. (22c) can be fitted satisfactorily.

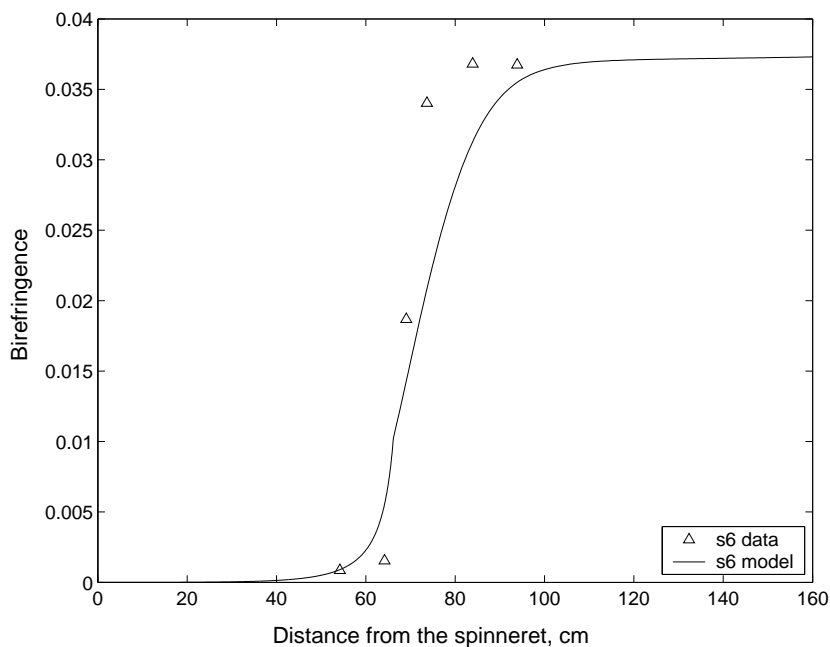


(a)



(b)

Fig. 22. The effect of molecular weight.

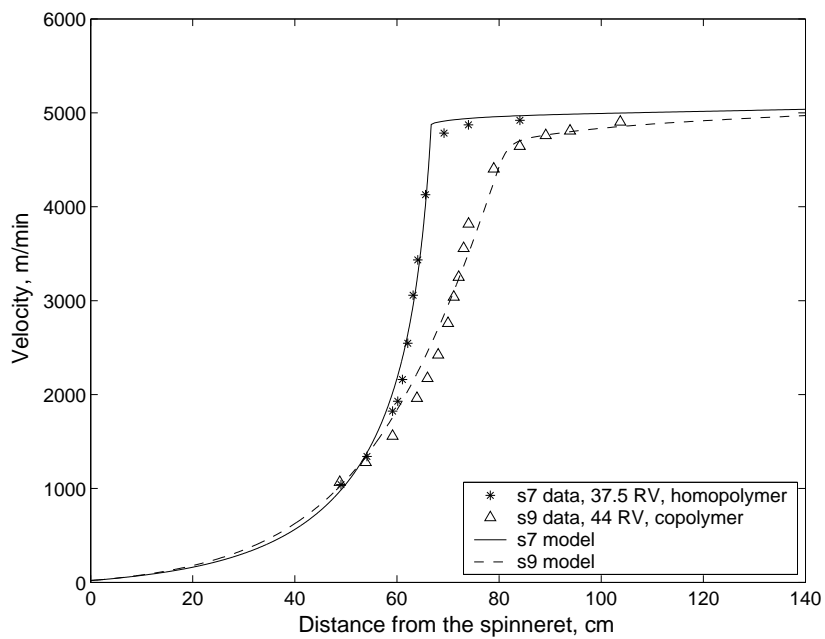


(c)

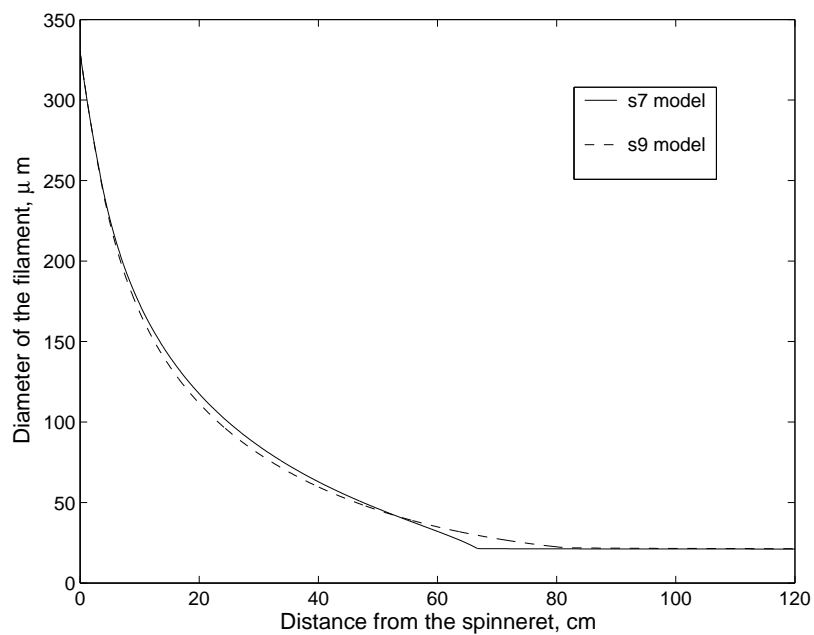
Figure 22 continued

f. Effect of the type of polymer

In spite of the S9 copolymer having a higher molecular weight with a slightly lower ambient temperature compared to the S7 homopolymer (see Fig. 23), the freeze point of the copolymer is further away from the spinneret indicating it does not readily crystallize compared to the homopolymer. To capture this effect, appropriate values are assigned to the parameters A^m and C_b . Since the copolymer has a higher molecular weight, the viscosity constant ν_o^m is increased. The diameter profile (Fig. 23b) of the homopolymer shows necking, while the copolymer does not. The copolymer develops lower final crystallinity compared to the homopolymer.

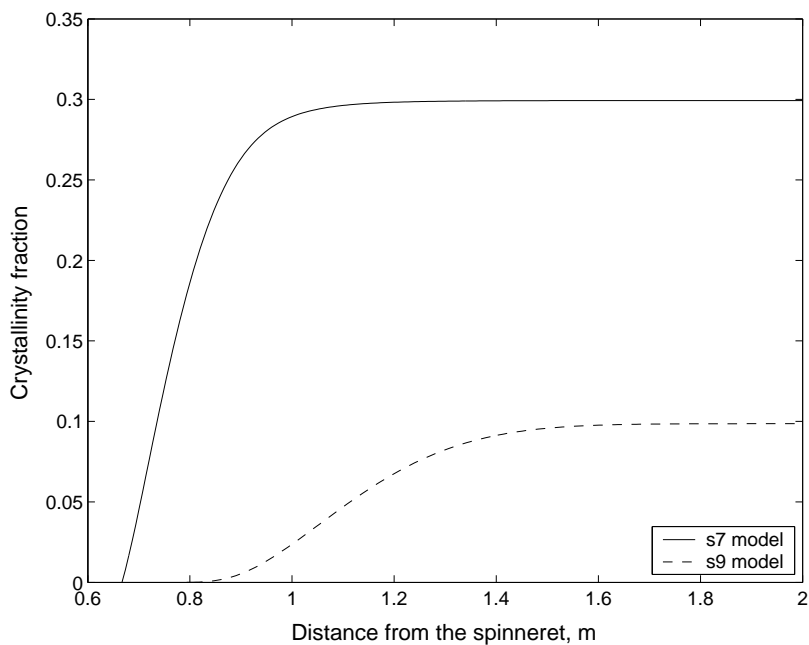


(a)



(b)

Fig. 23. Velocity, Filament diameter and crystallinity for different polymers.

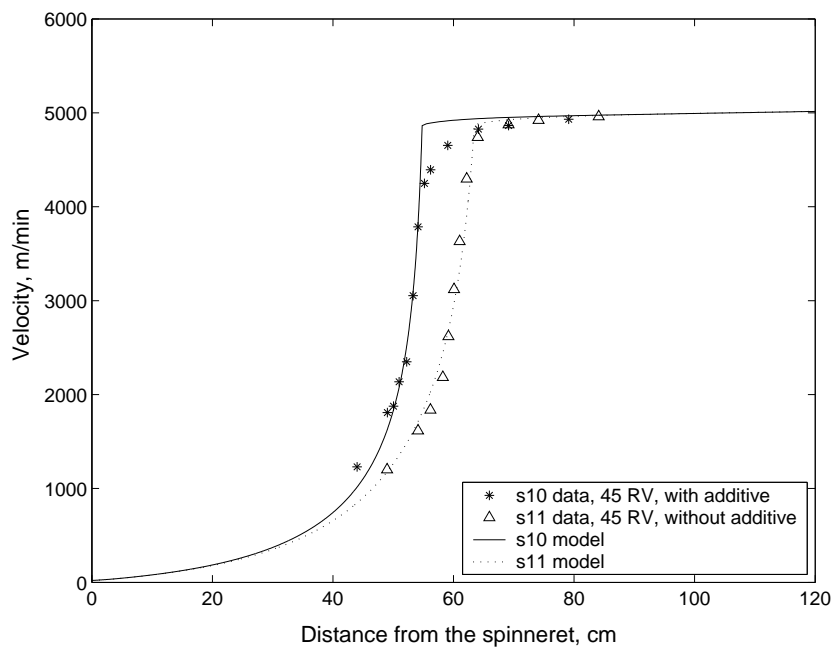


(c)

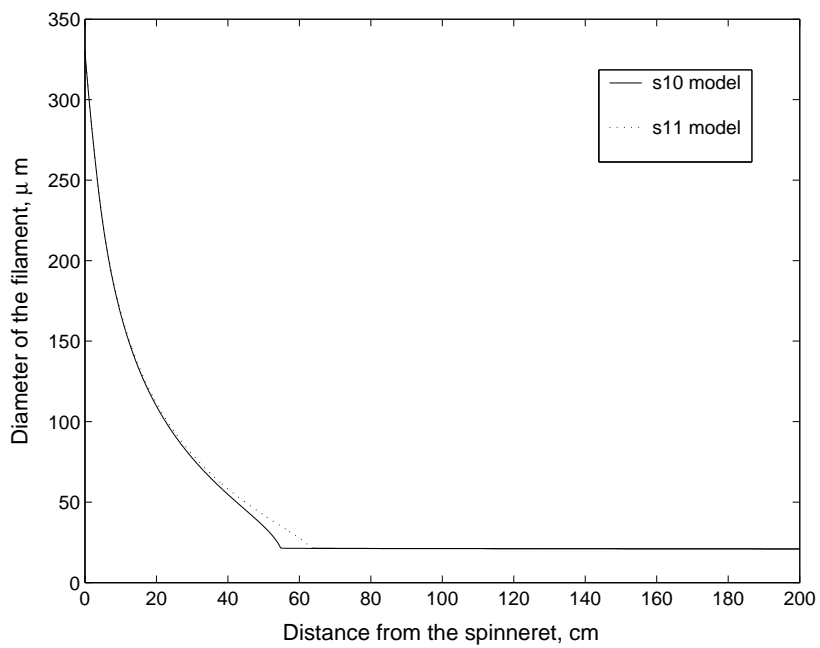
Figure 23 continued

g. Effect of additives

The additives move the freeze point closer to the spinneret. Since the intrinsic crystalline birefringence depends on the molecular weight of the melt from which crystals are formed, due to unavailability of such data, the intrinsic crystalline birefringence is determined so that the plateau of Fig. (24c) fits.

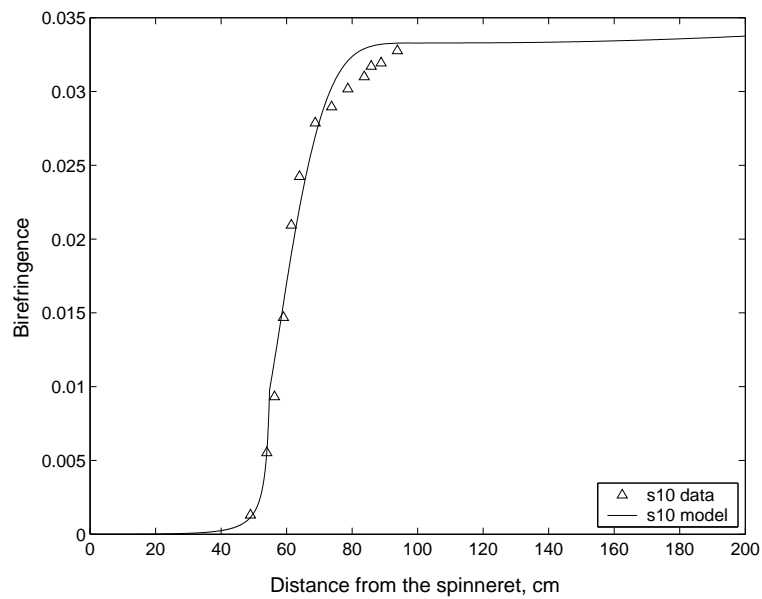


(a)

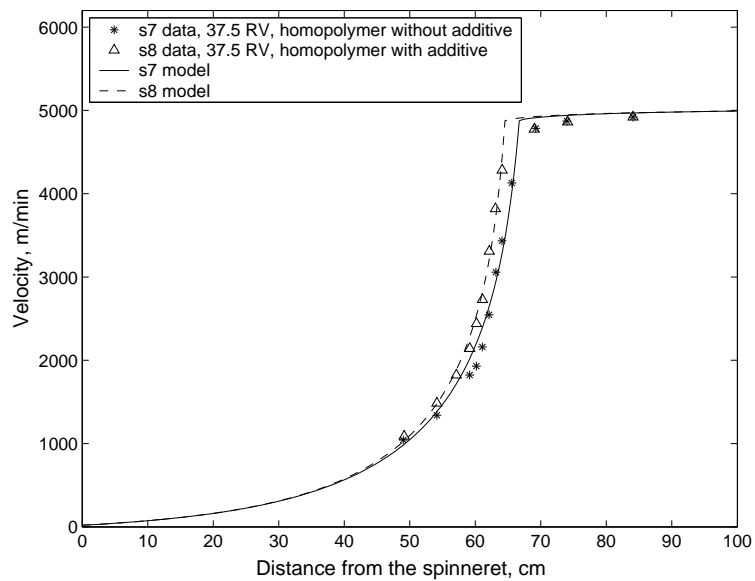


(b)

Fig. 24. The effect of additives on homopolymer nylon



(c)



(d)

Figure 24 continued

2. Radial resolution approximation

The results obtained for nylon 6 (BHS resin) at two different mass flow rates are depicted in the Figs. (25), (26) and (27). The Fig. (25) does not show neck formation even for the highest take-up speed. The crystallinity and the rate of crystallization achieved is very small for all the take-up speeds and hence there is no significant release of latent energy. For both the figures, we used the correlation of Matsui [37]. Patel *et al.* [49] used a correlation constant that is less than that reported by Matsui [37], i.e., $0.27\text{Re}^{-0.61}$. The experimental data shows an increased drop in the diameter for a take-up speed of 6660 m/min around 110 cms from the spinneret. The theory predicts the diameter of the filament quite accurately for all take up speeds except for that at 6660 m/min. Here, the prediction for the formation of the neck is not as pronounced as that observed in the experiment. At this take-up speed, for distances greater than around 1 m, the rate of crystallization reaches a maximum and since the crystallization is an exothermic process, the temperature of the material increases. This increase in temperature is predicted very well by the theory. The other four take-up speeds do not show such an increase in temperature. The theory predicts an increase in crystallinity to the ultimate value (0.487) only for the highest take-up speed; at all other take up speeds the increase in crystallinity is very small. The birefringence results that are presented for the take up speed of 6660 m/min is not satisfactory. Since there is evidence for the presence of two different types of crystals (α and γ) in nylon 6 (see Koyama *et al.* [34]), one may include the contribution of these crystals to the birefringence (one must have a theory to predict the amount of each crystals with each type of crystal being treated as a separate phase). By including these contributions, one may be able to obtain a better fit for the birefringence data depicted in Fig. (26); in fact, the crystalline phase is dominated by the γ phase (see

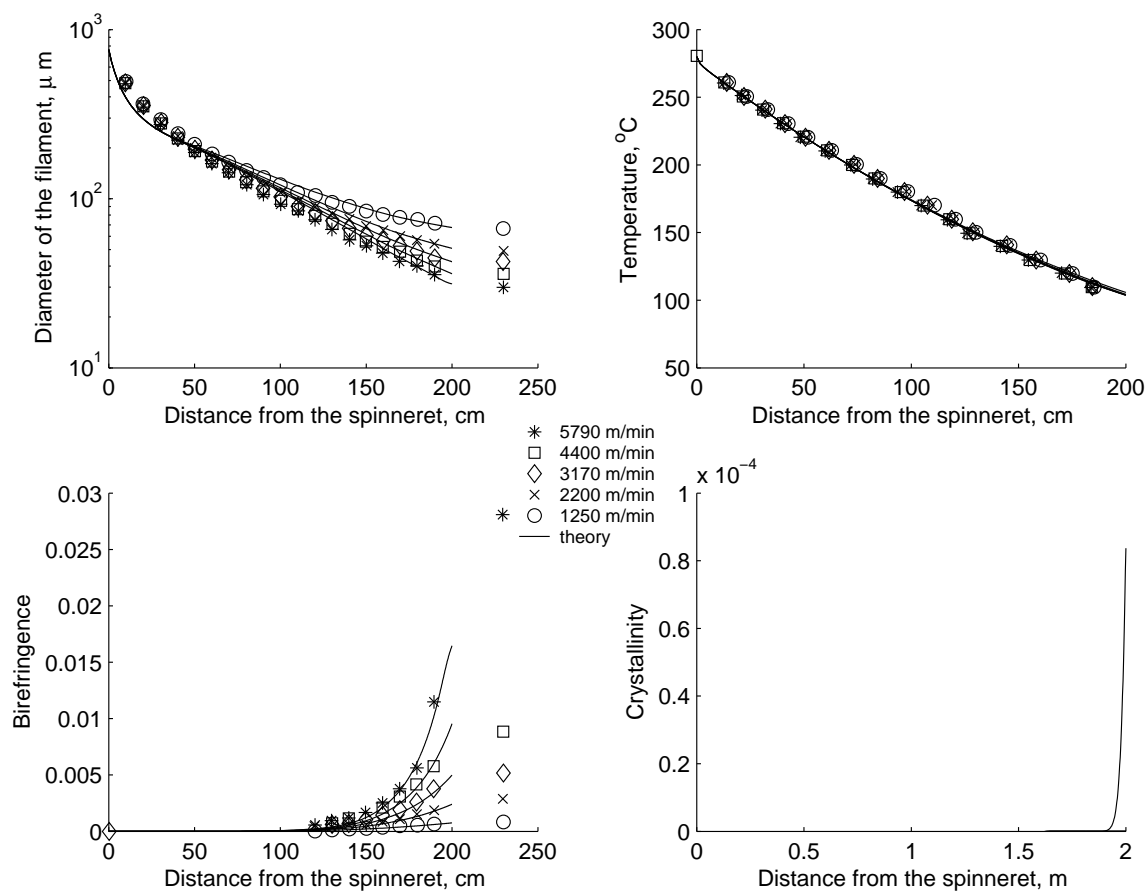


Fig. 25. The plots associated with the mass flow rate of nylon 6 (BHS) at 5.069 g/min.

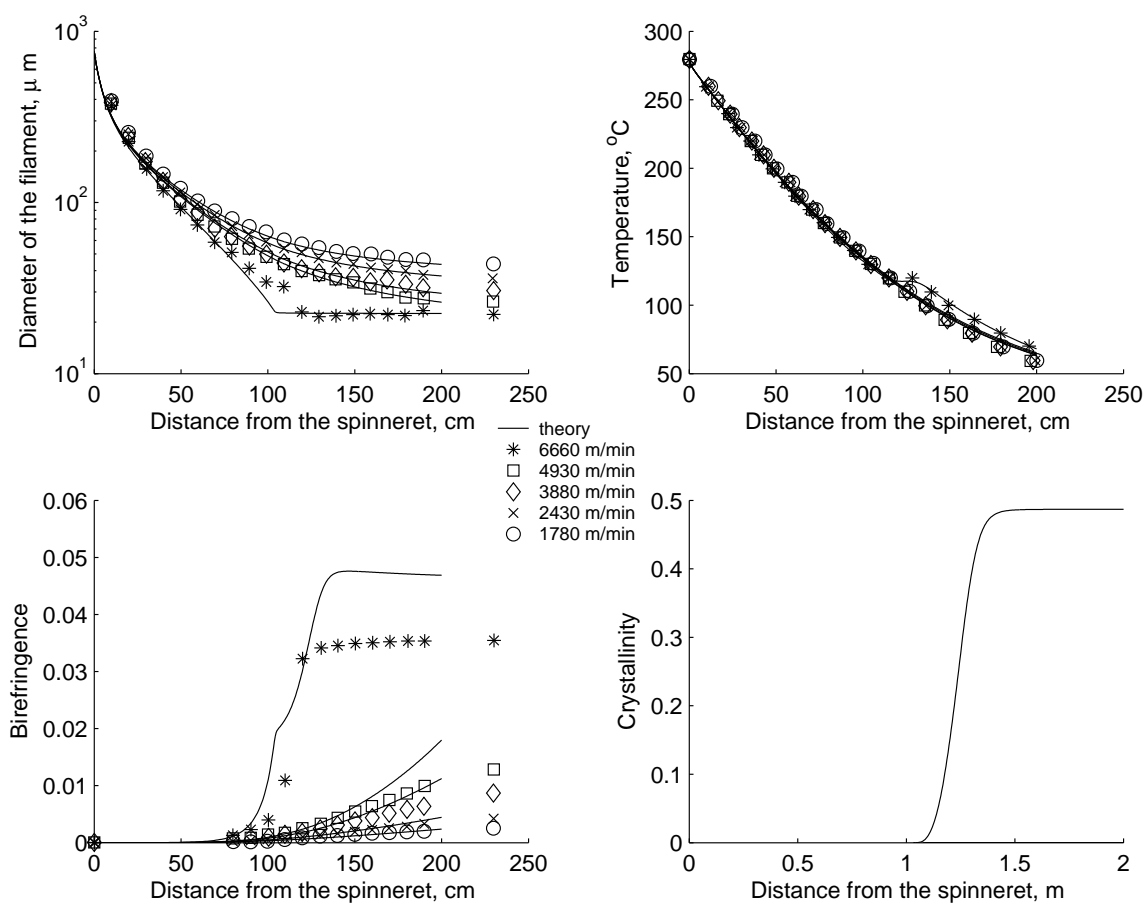


Fig. 26. The plots associated with the mass flow rate of nylon 6 (BHS) at 2.993 g/min.

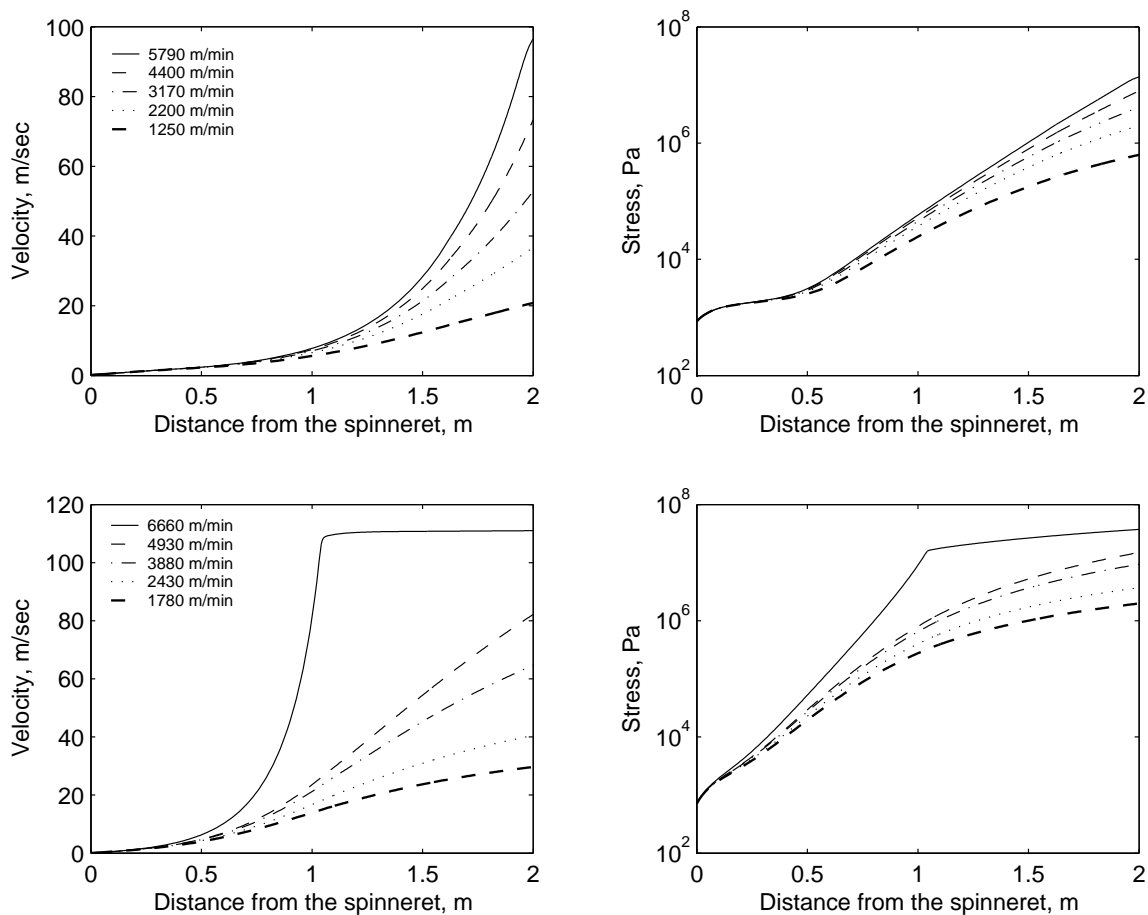


Fig. 27. The velocity and stress plots associated with the mass flow rate of nylon 6 (BHS) at 5.069 g/min (the top two figures) and 2.993 g/min respectively.

Koyama *et al.* [34]), which has lower intrinsic birefringence compared to the α phase. Patel *et al.* [49] have a similar overprediction of the birefringence for mass flow rate of 2.993 g/min. The Fig. (27) shows that, for a mass flow rate of 2.993 g/min, the velocity reaches a constant value. Such a plateau is not reached by using a Newtonian model in the melt and the mixture regime. Since the radial resolution approximation is used in the melt regime, the stress varies across the cross section of the filament (see Eq. (4.19)). For reasons of continuity of stress, the stress plots in the melt regime are calculated using the surface temperature. The stress plot for the same mass flow rate shows both qualitative and quantitative change in the behavior for the take up speed of 6660 m/min compared to the others. The stress, however does not show a considerable increase corresponding to the neck area as reported by Haberkorn *et al.* [27] .

The following two tables, i.e., Tables VI and VII, list the predicted take-up force and distance at which the mixture model is initiated.

Table VI. Take up force of BHS resin at a mass flow rate of 5.069 g/min.

Take up velocity (m/min)	Experimental (dynes)	Predicted (dynes)	Initiation distance (m)
1250	269.5	224.8	1.6598
2200	426.3	407.7	1.6433
3170	563.6	587.5	1.6343
4400	725.2	809.2	1.6274
5790	842.8	1062.4	1.6216

Table VII. Take up force of BHS resin at a mass flow rate of 2.993 g/min.

Take up velocity (m/min)	Experimental (dynes)	Predicted (dynes)	Initiation distance (m)
1780	279.3	294.7	1.0942
2430	347.9	403.3	1.0876
3880	475.3	638.6	1.0791
4930	553.7	803.8	1.0755
6660	999.6	1481.9	1.0326

F. Summary and conclusions

The melt was modeled as a viscoelastic liquid and the semicrystalline polymer is modeled as a mixture of elastic solids that are transversely isotropic and a viscoelastic liquid. An initiation criterion for crystallization, that is similar to that used by Nakamura *et al.* [44], that is dependent on temperature and deformation was obtained from thermodynamic considerations. By making a suitable choice of rate of the entropy production due to phase change (see Rao and Rajagopal [73]). By specializing this model to the fiber spinning problem, and using the balance equations, we obtained the equations for the melt and the mixture. The predictions of the theory agree well with the experimental data.

The development of the structure along the spinline is important because the mechanical properties of the solidified fiber depends on the final structure formed. While the model has shown the ability to fit the data quite well, better agreement can be achieved by a more judicious choice for the Helmholtz potential of the melt so that the stress tensor that is derived when used in the fiber spinning problem results in the formation of a sharper neck at a take up speed of 6660 m/min and by considering

a more detailed morphology of the semicrystalline solid. For instance, Koyama *et al.* [34], amongst others, have reported the presence of two crystals of nylon (α and γ) with the γ fraction dominating the α fraction. By incorporating this morphological detail into the correlation for birefringence, one may be able to achieve a better agreement with the birefringence data. Also, the cooling rate is not accounted for in the current model and this factor can play a major role in the determination of the final structure and hence the mechanical properties.

The model is able to predict much of the available industrial spinline data very well. Thus, one could possibly use this model to design the process, by simulating the appropriate problem in order to obtain solidified fibers with desired mechanical properties without having to resort to full scale experiments that are both expensive and time consuming. All the material properties for a particular type of polymer can be determined on the basis of a few simple experiments. This model could also be used in the design of blow molding and injection molding dies.

CHAPTER V

A THERMODYNAMICAL FRAMEWORK INCORPORATING THE EFFECT
OF THE THERMAL HISTORY ON THE SOLIDIFICATION OF MOLTEN
POLYMERS

So far, the effects of the thermal history were not included in the model. The cooling history has an effect on the total amount and the kind of the crystalline structure obtained at the end of the thermomechanical process. It also affects the temperature at which the crystallization is triggered. In this chapter, such effects are included and the framework developed by Rao and Rajagopal (2002) is extended. When the cooling rate is sufficiently slow, the crystallization kinetics described by Nakamura-type kinetics is insufficient as the slower "secondary" crystallization related to the lamellar thickening becomes important. Also, in some polymers, glass transition also occurs in conjunction with the crystallization and is usually triggered after the initiation of crystallization. These effects are also included and a model is obtained using a thermodynamic setting. As before, the melt is modeled as a viscoelastic liquid and the crystalline solid is modeled as a mixture of orthotropic elastic solid with the preferred directions of each crystalline solid born being determined by the eigen vectors $\mathbf{B}_{\kappa_{pm}(t)}$ of the melt. The amorphous glassy solid is modeled as an isotropic viscoelastic solid.

A. Introduction

The crystalline structure and hence the mechanical properties of the polymer depend on the thermal history to which the melt is subjected to prior to crystallization. However, the previous thermomechanical history of the polymer is not always known. There can be a number of reasons for the observed 'memory' effect. A small crystal

grown in the crack of a foreign substance in the previous polymer treatment may survive melting (see Tidick *et al.* [79]) and act as a nucleation center during the current process. Nuclei of subcritical size (embryos) may become supercritical (growth nuclei), self-nucleation of high-molecular weight crystals survive melting for a longer period compared to their low-molecular weight counterparts and self-nucleation caused by residual orientation due to previous thermomechanical history are some explanations for the memory effect. To erase the effects of previous thermomechanical history, the polymer is held at temperature above its melting point for a sufficient duration. Brucato *et al.* [6] and Piccarola *et al.* [54] conducted quenching, after nullifying memory effects, experiments on isotactic polypropylene (iPP), nylon-6 and PET under processing conditions (up to $\sim 2000^\circ$ C). The cooling rates are of the order of a few degrees per second was obtained using a differential scanning calorimeter (DSC) and the higher cooling rates were obtained by rapid quenching. About 100 – 200 μm samples were sandwiched between two pieces of Cu-Be alloy with very high thermal conductivity before the quenching under quiescent conditions. A thermocouple embedded in the sample measures the temperature. As opposed to DSC, where controlled cooling rates could be obtained (limited to a few hundred degrees per minute) rapid quenching, as expected, does not produce constant cooling rates. However, since the temperature history is measured, the results can be interpreted in terms of the thermal history undergone by the polymer. Wide angle X-ray diffraction (WAXD) was used to extract the amount of each phase present. At low cooling rates, iPP melt produced large quantities of α phase at room temperature, which is characterized by monoclinic crystals and at very high cooling rates (representative value of around

1000° C/sec) produced predominant mesomorphic phase¹; the cross over happens at around 100°C/sec. The maximum change in the density of the sample between the melt and α phase is around 2 – 3%. A similar behavior is also seen for nylon-6 and PET. As PET is largely an amorphous polymer, the transition from α triclinic at low cooling rates to amorphous glassy state takes place between 1 – 3°C/sec. Thus, iPP, nylon-6 and PET in the solid-like state is a mixture of α and mesomorphic phase, with the proportion of each constituent being determined by the thermal history undergone by the polymer.

In another study, Gogolewski et al. [23] studied the effects of annealing Nylon-6 samples at temperatures between 50°C and 220°C (Equilibrium melting temperature around 260°C) for duration up to 2000 hours. At such supercooled conditions, the melt begins to crystallize. It was found that at a fixed temperature below equilibrium melting temperature, the longer the annealing time the higher is the melting temperature, which was determined by subsequent heating cycle in a DSC. It was also found that, using X-ray diffraction, at 215°C, the lamellar crystal² thickness remains unchanged for a period of \sim 10hrs. (mirroring melting temperature) and then increases with annealing time and reaches a plateau. This implies that there is reordering of the crystals that had formed earlier after sufficient time (10hrs.), which increases the melting temperature. However, even after the cessation of lamellar thickening, the melting temperature of the nylon-6 sample continues to increase with annealing time. To explain this observation, secondary nucleation at the grain boundaries was proposed, which would increase the crystallinity and hence the melting temperature. The

¹IUPAC compendium of chemical technology: These are states of matter in which anisometric molecules (or particles) are regularly arranged in one (nematic state) or two (smectic state) directions, but randomly arranged in the remaining direction(s).

²IUPAC: A type of crystal with a large extension in two dimensions and a uniform thickness. The thickness of the crystal is around 5 – 50nm.

effect of temperature, at a fixed annealing time, on the thickening of lamellar crystals is the same as that of the annealing time. At sufficiently low temperature, there is very little molecular mobility and hence the lamellar thickness of nylon-6 does not change even after annealing for 1000hrs. As the temperature increases, the molecular mobility and the lamellar thickness increases. At sufficiently high temperature, the molecules have enough mobility to achieve equilibrium lamellar thickness. Gerardi *et al.* [22] also observed lamellar thickening during annealing of quenched iPP from the melt. Using small angle x-ray scattering (SAXS) , a set of lamellar thickness, corresponding to the monoclinic and mesomorphic phase was obtained. The melting temperature enhancement due to annealing, attributed to lamellar thickening, was also observed in syndiotactic polystyrene (sPS), PP and PET (see Gvozdic and Meier [26]). The change of the crystal structure during lamellar thickening due to annealing was ruled out because subsequent WAXD did not any change in the crystal structure itself. Petermann *et al.* [52] studied annealing of linear polyethylene at various temperatures using transmission electron microscopy and concluded that two mechanisms were in effect during crystal growth. One process involves selective melting of thinner lamellae, which gets incorporated into the unmelted crystal through epitaxial crystallization (recrystallization ³) when sufficient time is allowed. The other process involves snaking or gliding movements along the chain axis of the crystal at sufficiently high temperatures where molecular mobility is high (reorganization ⁴). During such a process, 3-dimensional crystalline order is not broken. The latter process increases the lamellar thickness while the former leads to a stacking of one lamellar crystal on

³Reorganization proceeding through partial melting.

⁴The molecular process by which (i) amorphous or poorly ordered regions of a polymer specimen become incorporated into crystals, or (ii) a change to a more stable crystal structure takes place, or (iii) defects within the crystal decrease.

the other. For a more detailed discussion of molecular mechanisms involved during annealing, refer to Dreyfus and Keller [16] and Yeh *et al.* [87].

Piccarola *et al.* [53] studied the effect of cooling rate on the crystallization of PET. All the samples were held at 280°C (above melting temperature) for 10 minutes to remove the effects of previous thermomechanical history. At low cooling rates ($\leq 1^\circ\text{C}/\text{sec}$), the effect of primary⁵ and secondary⁶ crystallization becomes important and at high cooling rates ($\geq 100^\circ\text{C}/\text{sec}$) forms an amorphous phase. At the intermediate cooling rates, the density (measured at 10°C after subjecting the sample to constant rate and quenching tests) change of PET is small, which is attributed to the changing quantities of the mixture of the mesomorphic and amorphous phase, and at the high cooling rates density change is almost zero and is presumed to be the amorphous phase density. The effect of cooling rate on the crystallization initiation temperature is significant. For example, the initiation temperature at 0.08°C/sec is around 230°C and at 2.33°C/sec is 170°C. In addition to the effects of cooling history on the quiescent polyethylene and polypropylene melt (see continuous cooling transformation curves in Spruiell and White [75]), which showed similar effects that of PET, the effect of stress in the melt is transparent, i.e., higher stress caused the crystallization start temperature to increase. Thus in a thermomechanical process, the competition between cooling history and deformation will decide the temperature at which crystallization starts.

⁵IUPAC: The first stage of crystallization, considered to be ended when most of the spherulite surfaces impinge on each other.

⁶IUPAC: Crystallization occurring after primary crystallization, usually proceeding at a lower rate.

B. Kinematics

The kinematics associated with the melt, glassy solid and the crystal is the same as that described in the previous two chapters, i.e.,

$$\overset{\nabla}{\mathbf{B}}^{\kappa_{pm}(t)} = \dot{\mathbf{B}}^{\kappa_{pm}(t)} - \mathbf{L}\mathbf{B}^{\kappa_{pm}(t)} - \mathbf{B}^{\kappa_{pm}(t)}\mathbf{L}^T = -2\mathbf{F}^{\kappa_{pm}(t)}\mathbf{D}^{\kappa_{pm}(t)}\mathbf{F}^{\kappa_{pm}(t)T}, \quad (5.1)$$

for the melt, where the above equation is valid until $f^{(1)} + f^{(2)} + f^{(3)} = 1$, where $f^{(i)}$, $i = 1, 2, 3$ are the weight fraction of the crystal form 1 and 2,

$$\overset{\nabla}{\mathbf{B}}^{\kappa_{ps}(t)} = \dot{\mathbf{B}}^{\kappa_{ps}(t)} - \mathbf{L}\mathbf{B}^{\kappa_{ps}(t)} - \mathbf{B}^{\kappa_{ps}(t)}\mathbf{L}^T = -2\mathbf{F}^{\kappa_{ps}(t)}\mathbf{D}^{\kappa_{ps}(t)}\mathbf{F}^{\kappa_{ps}(t)T}, t_3 \leq \tau \leq t \quad (5.2)$$

for the glassy solid,

$$\mathbf{F}^{\kappa_c(\tau)} := \mathbf{F}^{\kappa_R}(\mathbf{X}_{\kappa_R}, t)\mathbf{F}^{\kappa_R}{}^{-1}(\mathbf{X}_{\kappa_R}, \tau), \quad t_i \leq \tau \leq t, \quad i = 1, 2, \quad (5.3)$$

for the solid that came into being at time τ , where t_i , $i = 1, 2$ represent the time at which the crystal form 1 and 2 are born, respectively. As described in the previous chapters, one can define the left and the right Cauchy-Green stretch tensors (see Fig. 28) and their invariants associated with tensors $\mathbf{F}^{\kappa_c(\tau)}$, $i = 1, 2$.

We shall assume that the material is incompressible, i.e.,

$$\det(\mathbf{B}^{\kappa_{pm}(t)}), \det(\mathbf{B}^{\kappa_{ps}(t)}), \det(\mathbf{B}^{\kappa_r}) = 1 \quad (\text{or } \text{tr}(\mathbf{L}^{\kappa_{pm}(t)}), \text{tr}(\mathbf{L}^{\kappa_{ps}(t)}) = 0) \quad \text{and } \text{tr}(\mathbf{L}) = 0. \quad (5.4)$$

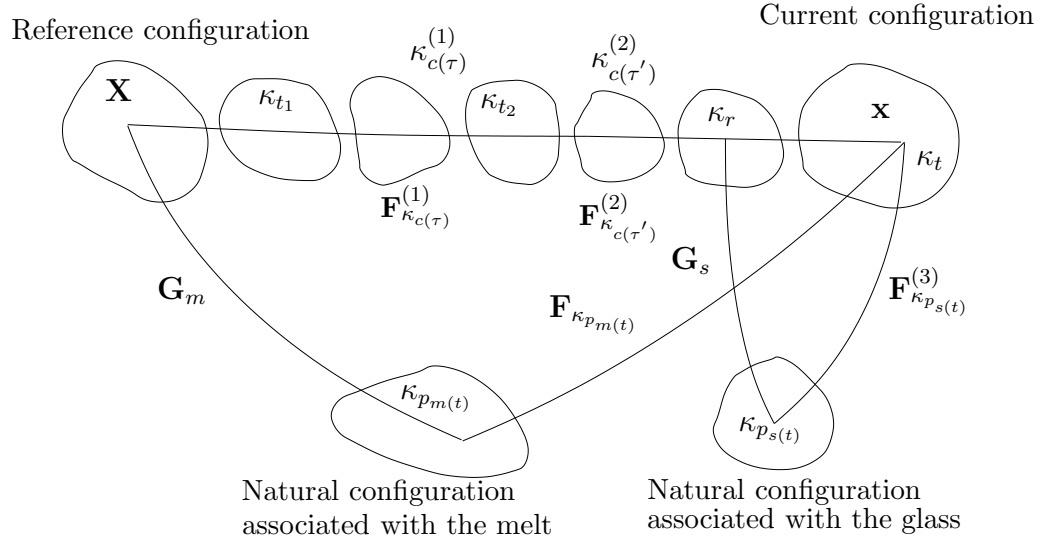


Fig. 28. The above figure represents the configurations associated with the solidifying mixture.

C. Modeling

The specific Helmholtz potential of the mixture is partitioned into four parts, with each part being weighted by their respective mass fractions, i.e.,

$$\begin{aligned}
\Psi = & (1 - f^{(1)} - f^{(2)} - f^{(3)}) \left\{ A^m + (B^m + c_2^m)(\theta - \theta_m) - c_1^m \frac{(\theta - \theta_m)^2}{2} \right. \\
& - c_2^m \theta \ln \left(\frac{\theta}{\theta_m} \right) + \frac{\mu^m \theta}{2\rho \theta_m b} \left\{ \left[1 + \frac{b}{n} (I_{\kappa_{p_m(t)}} - 3) \right]^n - 1 \right\} \left. \right\} \\
& + \sum_{i=1}^2 \int_{t_i}^t \left\{ A^{s,i} + (B^{s,i} + c_2^{s,i})(\theta(t) - \theta_{s,i}) - c_1^{s,i} \frac{(\theta(t) - \theta_{s,i})^2}{2} - c_2^{s,i} \theta(t) \ln \left(\frac{\theta(t)}{\theta_{s,i}} \right) \right. \\
& + D^{s,i} \exp \left\{ - E^{s,i} \left[\int_{t_o}^t \exp(F^{s,i}(\theta(\tau') - \theta_o)) d\tau' \right]^{n_i} \right\} \\
& + \frac{\mu_1^{s,i}}{2\rho} (I_{\kappa_{c(\tau)}}^{(i)}(t) - 3) + \frac{\mu_2^{s,i}}{2\rho} (J_{\kappa_{c(\tau)}}^{(i)}(t) - 1)^2 + \frac{\mu_3^{s,i}}{2\rho} (K_{\kappa_{c(\tau)}}^{(i)}(t) - 1)^2 \left. \right\} \frac{df^{(i)}}{d\tau} d\tau \\
& + f^{(3)} \left\{ A^{s,3} + (B^{s,3} + c_2^{s,3})(\theta - \theta_{s,3}) - c_1^{s,3} \frac{(\theta - \theta_{s,3})^2}{2} - c_2^{s,3} \theta \ln \left(\frac{\theta}{\theta_{s,3}} \right) \right. \\
& + \frac{\mu_1^{s,3}}{2\rho} (I_{\kappa_{p_s(t)}}^{(3)} - 3) + \frac{\mu_2^{s,3}}{2\rho} (I_{\kappa_r}^{(3)} - 3) \left. \right\} = (1 - f^{(1)} - f^{(2)} - f^{(3)}) \Psi^m \\
& + \sum_{i=1}^2 \Psi^{s,i} + f^{(3)} \Psi^{s,3}, \tag{5.5}
\end{aligned}$$

where $K_{\kappa_c(\tau)}^{(i)} := \mathbf{C}_{\kappa_c(\tau)}^{(i)} \mathbf{m}_{\kappa_c(\tau)} \cdot \mathbf{m}_{\kappa_c(\tau)}$, $J_{\kappa_c(\tau)}^{(i)} := \mathbf{C}_{\kappa_c(\tau)}^{(i)} \mathbf{n}_{\kappa_c(\tau)} \cdot \mathbf{n}_{\kappa_c(\tau)}$, $i = 1, 2$, $\mathbf{n}_{\kappa_c(\tau)}$ and $\mathbf{m}_{\kappa_c(\tau)}$ are the eigen vectors of $\mathbf{B}_{\kappa_{pm}(t)}$, θ_m , A^m , B^m , c_1^m , c_2^m , b , n and μ^m are the reference temperature and the material constants associated with the melt, $\{\theta_{s,i}$, $A^{s,i}$, $B^{s,i}$, $c_1^{s,i}$, $c_2^{s,i}$, $\{\mu_j^{s,i}$, $j = 1, 2, 3\}$, $D^{s,i}$, $E^{s,i}$, $F^{s,i}$ and n_i , $i=1,2\}$ are the reference temperature and the material constants associated with the crystal forms 1 and 2 and $\theta_{s,3}$, $A^{s,3}$, $B^{s,3}$, $c_1^{s,3}$, $c_2^{s,3}$, $\{\mu_j^{s,3}$, $j = 1, 2\}$ are the material constants associated with the glass. The specific functional form chosen for the melt and the glass (see previous chapters) is the same as before except for the crystalline solid. The crystallized material from the melt born at each instant τ is modeled as an orthotropic elastic solid. The term on the fourth line of the above equation quantifies the thermal history dependence. The polymer melt at time t_o is assumed to devoid of any previous thermomechanical history, i.e., memory effects are erased. The glassy solid is modeled as an amorphous viscoelastic solid (see Ch. 3). Note that the indices 1 and 2 refer to the crystal form 1 and 2 and the index 3 refers to the glassy solid. Since the melt and the glassy solid can dissipate, the rate of dissipation, appropriately weighted, is assumed to be of the following form:

$$\begin{aligned} \xi = & (1 - f^{(1)} - f^{(2)} - f^{(3)}) 2\nu^m(\theta, \mathbf{B}_{\kappa_{pm}(t)}) \{ \mathbf{D}_{\kappa_{pm}(t)} \cdot \mathbf{B}_{\kappa_{pm}(t)} \mathbf{D}_{\kappa_{pm}(t)} \}^\beta \\ & + f^{(3)} 2\nu^s(\theta, \mathbf{B}_{\kappa_{ps}(t)}) \mathbf{D}_{\kappa_{ps}(t)} \cdot \mathbf{B}_{\kappa_{ps}(t)} \mathbf{D}_{\kappa_{ps}(t)} \end{aligned} \quad (5.6)$$

The second law, used to place restrictions on the constitutive equations, is introduced in the following form (see Green and Naghdi [25]):

$$\mathbf{T} \cdot \mathbf{D} - \rho \dot{\Psi} - \rho \eta \dot{\theta} - \frac{\mathbf{q} \cdot \text{grad}(\theta)}{\theta} = \rho \theta \zeta = \hat{\xi}, \quad \hat{\xi} \geq 0, \quad (5.7)$$

Assuming additivity of the entropy producing mechanisms associated with solidification of molten polymers, the right hand side of Eq. (5.7) becomes

$$\hat{\xi} = \xi_c + \xi_d^m + \xi_d^{(3)} + \xi_p^{(1)} + \xi_p^{(2)} + \xi_r^{(1)} + \xi_r^{(2)} + \xi_p^{(3)}, \quad (5.8)$$

with each of the terms on the right hand side of Eq. (5.8) being non-negative; they represent the rate of entropy production (times $\rho\theta$) due to conduction, dissipation in the melt, dissipation in the glassy solid, crystallization of the melt to crystal forms 1 and 2, rearrangement of the crystals that had formed for the crystal forms 1 and 2, and solidification the remaining melt to a glassy solid, respectively.

As usual (see Chapter 2),

$$\xi_c = -\frac{\mathbf{q} \cdot \text{grad}(\theta)}{\theta}. \quad (5.9)$$

The rate of entropy production (times $\rho\theta$) due to conduction is assumed to be

$$\xi_c = \frac{\mathbf{k}(\mathbf{B}_{\kappa_{ps}(t)}, f^{(1)}, f^{(2)}, f^{(3)}) \text{grad}(\theta) \cdot \text{grad}(\theta)}{\theta}, \quad (5.10)$$

where $\mathbf{k}(\mathbf{B}_{\kappa_{ps}(t)}, f^{(1)}, f^{(2)}, f^{(3)})$ is positive definite and is given by:

$$\begin{aligned} \mathbf{k}(\mathbf{B}_{\kappa_{ps}(t)}, f^{(1)}, f^{(2)}, f^{(3)}) &= (1 - f^{(1)} - f^{(2)} - f^{(3)}) \mathbf{k}^m(\mathbf{B}_{\kappa_{pm}(t)}) \\ &+ f^{(1)} \mathbf{K}^{(1)} + f^{(2)} \mathbf{K}^{(2)} + f^{(3)} k^{(3)} \mathbf{I} \end{aligned} \quad (5.11)$$

The constitutive equation for the heat flux is assumed to be weighted with the mass fraction of each constituent:

$$\mathbf{q} = -\{(1 - f^{(1)} - f^{(2)} - f^{(3)}) \mathbf{k}^m(\mathbf{B}_{\kappa_{pm}(t)}) + f^{(1)} \mathbf{K}^{(1)} + f^{(2)} \mathbf{K}^{(2)} + f^{(3)} k^{(3)} \mathbf{I}\} \text{grad}(\theta), \quad (5.12)$$

where $\mathbf{k}^m(\mathbf{B}_{\kappa_{pm}(t)})$, $\mathbf{K}^{(1)}$ and $\mathbf{K}^{(2)}$ are symmetric and positive definite and $k^{(3)} > 0$. These requirements guarantee that the rate entropy production due to conduction to be positive for non-zero $\text{grad}(\theta)$ as required. When $\text{grad}(\theta)$ is zero, then there is

no conduction and the associated rate of entropy production is zero. As the melt stretches, the molecules tend to get aligned in a certain direction and hence the components of the heat flux vector will be different as compared to the components corresponding to the unstretched melt. The stretch in the crystal form 1 and 2, and the glassy solid is small in typical industrial processes such as fiber spinning, film blowing, blow molding, etc. Therefore, their respective thermal conductivity tensors do not depend on their stretch tensors. Eventhough the crystalline solid formed at every instant is assumed to be orthotropic, the preferred directions associated with the crystal forms 1 and 2 formed at every instant are dependant on the eigen vectors of the Cauchy stress \mathbf{T} (or $\mathbf{B}_{\kappa_{pm}(t)}$) at that instant and as a result tensor valued functional associated with their corresponding thermal conductivity, in general, should depend on the history of the eigen vectors of the crystal forms 1 and 2. Since such an approach is complicated, only a second order tensor is used in its place representing an average orientation of the crystals. The glassy solid is amorphous and hence a Fourier conduction is assumed.

In manner similar to that described in Ch 2 and 3, using reduced dissipation equation, it can be shown that the initiation conditions for the crystal forms 1 and 2 and the glass, crystallization equations, glass transition kinetics, stress tensor, internal energy, entropy can be obtained within a unified setting.

The initiation conditions are

$$\begin{aligned}
& A^m + (B^m + c_2^m)(\theta - \theta_m) - c_1^m \frac{(\theta - \theta_m)^2}{2} - c_2^m \theta \ln \left(\frac{\theta}{\theta_m} \right) \\
+ & \frac{\mu^m \theta}{2\rho\theta_m b} \left\{ \left[1 + \frac{b}{n}(I_{\kappa_{pm}(t)} - 3) \right]^n - 1 \right\} - \left\{ A^{s,i} + (B^{s,i} + c_2^{s,i})(\theta - \theta_{s,i}) \right. \\
- & \left. c_1^{s,i} \frac{(\theta - \theta_{s,i})^2}{2} - c_2^{s,i} \theta \ln \left(\frac{\theta}{\theta_{s,i}} \right) + D^{s,i} \exp \left\{ - E^{s,i} \left[\int_{t_o}^t \exp(F^{s,i}(\theta(\tau) \right. \right. \right. \\
- & \left. \left. \left. \theta_o) \right) d\tau \right]^{n_i} \right\} \right\} = \Psi^m - \hat{\Psi}^{s,i} = 0, \quad i = 1, 2, 3 \text{ with } D^{s,3} \equiv 0. \quad (5.13)
\end{aligned}$$

If the cooling rate is low, then the melt spends a longer time at higher temperatures and thus the last term of the Eq. (4.14) becomes small causing a high crystallization initiation temperature and vice versa as observed in experiments.

Eventhough there may be some melting of thinner lamellae during annealing or under very slow cooling rates, the overall crystallinity of the polymer continues to increase. The rate of entropy production, attributed to reorganization and recrystallization (annealing effects), are given through

$$\xi_r^{(i)} = -\rho f^{(i)} \frac{d}{dt} D^{s,i} \exp \left\{ -E^{s,i} \left[\int_{t_o}^t \exp(F^{s,i}(\theta(\tau) - \theta_o)) d\tau \right]^{n_i} \right\}, \quad i = 1, 2. \quad (5.14)$$

It is easy to check that the above equation is non-negative.

The Cauchy stress tensor is given through

$$\begin{aligned} \mathbf{T} = & -p\mathbf{I} + (1 - f^{(1)} - f^{(2)} - f^{(3)}) \frac{\mu^m \theta}{\theta_m} \left[1 + \frac{b}{n} (I_{\kappa_{pm}(t)} - 3) \right]^{n-1} \mathbf{B}_{\kappa_{pm}(t)} \\ & + \sum_{i=1}^2 \int_{t_i}^t \left\{ \mu_1^{s,i} \mathbf{B}_{\kappa_c(\tau)}^{(i)} + 2\mu_2^{s,i} (J_{\kappa_c(\tau)}^{(i)} - 1) \mathbf{F}_{\kappa_c(\tau)}^{(i)} (\mathbf{n}_{\kappa_c(\tau)} \otimes \mathbf{n}_{\kappa_c(\tau)}) \mathbf{F}_{\kappa_c(\tau)}^{(i)T} \right. \\ & + \left. 2\mu_3^{s,i} (K_{\kappa_c(\tau)}^{(i)} - 1) \mathbf{F}_{\kappa_c(\tau)}^{(i)} (\mathbf{m}_{\kappa_c(\tau)} \otimes \mathbf{m}_{\kappa_c(\tau)}) \mathbf{F}_{\kappa_c(\tau)}^{(i)T} \right\} \frac{df^{(i)}}{d\tau} d\tau \\ & + f^{(3)} (\mu_1^{s,3} \mathbf{B}_{\kappa_{ps}(t)} + \mu_2^{s,3} \mathbf{B}_{\kappa_r}), \end{aligned} \quad (5.15)$$

the entropy of the mixture is given by

$$\begin{aligned} \eta = & (1 - f^{(1)} - f^{(2)} - f^{(3)}) \left\{ -B^m + c_1^m (\theta - \theta_m) + c_2^m \ln \left(\frac{\theta}{\theta_m} \right) \right. \\ & - \frac{\mu^m}{2\rho\theta_m b} \left\{ \left[1 + \frac{b}{n} (I_{\kappa_{pm}(t)} - 3) \right]^n - 1 \right\} \left. + \sum_{i=1}^3 f^{(i)} \left\{ -B^{s,i} + c_1^{s,i} (\theta - \theta_{s,i}) \right. \right. \\ & \left. \left. + c_2^{s,i} \ln \left(\frac{\theta}{\theta_{s,i}} \right) \right\} \right\} \end{aligned} \quad (5.16)$$

and the internal energy is given through

$$\begin{aligned}
\epsilon = & (1 - f^{(1)} - f^{(2)} - f^{(3)}) \left\{ A^m - B^m \theta_m + \frac{1}{2} c_1^m (\theta^2 - \theta_m^2) + c_2^m (\theta - \theta_m) \right\} \\
& + \sum_{i=1}^2 \left\{ f^{(i)} \left\{ A^{s,i} - B^{s,i} \theta_{s,i} + \frac{1}{2} c_1^{s,i} (\theta^2 - \theta_{s,i}^2) + c_2^{s,i} (\theta - \theta_{s,i}) \right\} \right. \\
& + \int_{t_i}^t \left\{ \frac{\mu_1^{s,i}}{2\rho} (I_{\kappa_c^{(i)}}^{(i)}(t) - 3) + \frac{\mu_2^{s,i}}{2\rho} (J_{\kappa_c^{(i)}}^{(i)}(t) - 1)^2 + \frac{\mu_3^{s,i}}{2\rho} (K_{\kappa_c^{(i)}}^{(i)}(t) - 1)^2 \right\} \frac{df^{(i)}}{d\tau} d\tau \\
& + f^{(i)} D^{s,i} \exp \left\{ - E^{s,i} \left[\int_{t_o}^t \exp(F^{s,i}(\theta(\tau) - \theta_o)) d\tau \right]^{n_i} \right\} \\
& + f^{(3)} \left\{ A^{s,3} - B^{s,3} \theta_{s,3} + \frac{1}{2} c_1^{s,3} (\theta^2 - \theta_{s,3}^2) + c_2^{s,3} (\theta - \theta_{s,3}) \right. \\
& + \left. \frac{\mu_1^{s,3}}{2\rho} (I_{\kappa_{ps}^{(3)}}^{(3)} - 3) + \frac{\mu_2^{s,3}}{2\rho} (I_{\kappa_r}^{(3)} - 3) \right\}. \tag{5.17}
\end{aligned}$$

The rate of entropy production due to crystallization and glass transition is defined as

$$\xi_p^{(i)} = \frac{\rho(\Psi^m - \hat{\Psi}^{s,i})(\dot{f}^{(i)})^2}{d\phi^{(i)}/dt}, \quad i = 1, 2, 3, \tag{5.18}$$

where

$$\begin{aligned}
\phi^{(i)} = & \alpha_{p,i} \left\{ 1 - \exp \left\{ - \left[\int_{t_i}^t \hat{K}_{p,i}(\theta(\tau), \mathbf{B}_{\kappa_{pm}(\tau)}(\tau)) d\tau \right]^{n_{p,i}} \right\} \right\} \\
& + \alpha_{s,i} \int_{t_i}^t \frac{d}{d\tau} \left\{ 1 - \exp \left\{ - \left[\int_{t_i}^{\tau} \hat{K}_{p,i}(\theta(\tau'), \mathbf{B}_{\kappa_{pm}(\tau')}(\tau')) d\tau' \right]^{n_{p,i}} \right\} \right\} \\
& \times \left\{ 1 - \exp \left\{ - \left[\int_{\tau}^t \hat{K}_{s,i}(\theta(\tau'), \mathbf{B}_{\kappa_{pm}(\tau')}(\tau')) d\tau' \right]^{n_{s,i}} \right\} \right\} d\tau, \quad i = 1, 2 \\
\phi^{(3)} = & (1 - f^{(1)} - f^{(2)}) \left\{ 1 - \exp \left\{ - \left[\int_{t_3}^t \hat{K}_{p,3}(\theta(\tau), \mathbf{B}_{\kappa_{pm}(\tau)}(\tau)) d\tau \right]^{n_{p,3}} \right\} \right\} \\
\Rightarrow f^{(i)} = & \phi^{(i)}, \quad i = 1, 2, 3 \tag{5.19}
\end{aligned}$$

and the functions $\hat{K}_{s,i}(\theta, \mathbf{B}_{\kappa_{pm}(t)})$ are given by

$$\begin{aligned} \hat{K}_{q,i}(\theta, \mathbf{B}_{\kappa_{pm}(t)}) &= K_o^{q,i} \exp\left(\frac{-C_1^{q,i}}{\theta - \theta_c^{q,i}}\right) \exp\left(\frac{-C_2^{q,i}}{\theta(\hat{\Psi}_m - \hat{\Psi}^{s,i})}\right), \\ &\{q = p, s; i = 1, 2\}, \{q = p, i = 3\}, \end{aligned} \quad (5.20)$$

where

$$\begin{aligned} \hat{\Psi}_m &= A^m + (B^m + c_2^m)(\theta - \theta_m) - c_1^m \frac{(\theta - \theta_m)^2}{2} - c_2^m \theta \ln\left(\frac{\theta}{\theta_m}\right) \\ &+ C_b \frac{\mu^m \theta}{2\rho\theta_m b} \left\{ \left[1 + \frac{b}{n}(I_{\kappa_{pm}(t)} - 3) \right]^n - 1 \right\}. \end{aligned} \quad (5.21)$$

To get the last equation of Eq. (5.19), zero initial conditions are used. All the integrands in Eq. (5.19) are always positive and hence $\xi_p^{(i)}$ is non-negative provided that $\Psi^m - \hat{\Psi}^{s,i} \geq 0$. We shall use $\Psi^m - \hat{\Psi}^{s,i} \geq 0$ as a constraint, which places restrictions on the constants that appear in it. The transformation kinetics equation is allowed to proceed until $\sum_{i=1}^3 f^{(i)} = 1$. The crystallization kinetics equation has a similar structure as that of Hillier [29], Gordon and Hillier [24]. A modification to the Avrami equation was proposed (isothermal and quiescent) by Hillier [29] and Price [55] to explain the anomalous fractional values of the Avrami exponent when applied to certain polymers, which does not have physical meaning, and slow secondary crystallization. The primary crystallization is associated with the constant radial growth rate of spherulites (observed in experiments), which are semicrystalline, and further crystallization is allowed within a spherulite termed as post-Avrami crystallization. Price [55] showed that if the post-Avrami process is sufficiently slower than the primary crystallization, then the crystallization curves resemble that of polymers where secondary crystallization (crystallinity proportional to $\log(\text{time})$ and is related to lamellar thickening) is present. Hillier [29] showed that if the two processes have comparable half-lives, then the crystallization curves obtained resemble that of certain

polymers where secondary crystallization is absent, which further lead to anomalous fractional values when post-Avrami crystallization is ignored. The model was able to fit the isothermal quiescent crystallization data of polymethylene, polyethylene oxide, etc. Refer to Verhoyen [83] for the discussion of the other modifications of Avrami equation.

Equations (5.19), $i = 1, 2$ represent the non-isothermal version of Hillier's model including the effect of deformation. The first part of the equation represent the primary crystallization and has the same form as that of Nakamura equation (see Nakamura [44]). The maximum value taken by $f^{(i)}$ are $\alpha_{p,i} + \alpha_{s,i}$, $i = 1, 2$ and $f^{(3)} = 1 - f^{(1)} - f^{(2)}$. Since the total weight fraction of the crystalline phase is always less than unity, we have $\sum_{i=1}^2 \alpha_{p,i} + \alpha_{s,i} < 1$. The term within the curly braces is between 0 and 1 and represents the mass fraction of the spherulites (growing in the melt) of crystal form 1 under quiescent isothermal conditions when $f^{(2)} = f^{(3)} = 0$. The spherulites stop growing when they impinge upon one another consuming all the available melt and thus the mass fraction occupied by the spherulite is unity. But, the spherulites themselves are semicrystalline and thus necessitating a constant $\alpha_{p,i} < 1$. The second term represents the extra crystallinity due to post-Avrami or secondary crystallization within the spherulite and the extend of secondary crystallization depends on the age of the point within the spherulite.

The glass transformation kinetics $f^{(3)}$ has a similar mathematical form as that of the crystallization kinetics, but differ in the interpretation. All the available melt is assumed to be transformed into glass at the end of glass transition process.

The evolution equation for the natural configurations of the melt and the glass is the same as Eqs. (4.15) and (3.66), respectively.

D. Summary and conclusions

A specific model was obtained using a general thermodynamic setting including the effects of thermomechanical history dependant initiation of crystallization, primary and slow secondary crystallization and flow-induced crystallization. The amount and the type of crystalline phase attained depends on the thermomechanical history undergone by the polymer. For many polymers such as Nylon 6, Nylon 66, polypropylene and so forth, two phases have been found in their semicrystalline state, namely, mesomorphic and monoclinic or triclinic phase. Eventhough the lattice structure may be triclinic, monoclinic and so forth, they tend to get aligned as dictated by deformation giving an overall anisotropy that could be approximated as being orthotropic. The model can predict the amount and the type of crystalline structures formed. Here, the model takes into account two different crystalline structures, eventhough it can be easily generalized to account for more number of crystalline phases. If the cooling rate is sufficiently fast, it is possible to bypass the crystallization route and the polymer melt will solidify into a glass. Such effects could also be predicted by the model.

CHAPTER VI

SUMMARY AND CONCLUSIONS

A sufficiently general thermodynamic framework has been put into place taking into account the effects of viscoelasticity of polymer melts, thermomechanical history dependant crystallization initiation condition, flow-induced crystallization including the effects of evolution of symmetry of two different crystalline phases, secondary crystallization, viscoelasticity of the amorphous solid and the glass transition kinetics. The evolution equations for the melt and amorphous solid, initiation conditions for the crystallization and glass transition, crystallization and glass transition kinetics, the forms of stress tensor, entropy and internal energy have been obtained using an unified thermodynamical framework.

The predictions of the model obtained using simplified versions of the framework discussed in Ch. 5 (as deemed appropriate by the processes and class of polymers under consideration), after determining the material constants, were compared with extensive set of industrial spinline data. The predictions of the model agree well with the experimental data.

The thermodynamical framework put forth takes into account most of the attributes that are important for typical industrial processes. The effects of compressibility nor the effects of pressure (important in die casting) have not been taken into account. However, such effects are not important for fiber spinning, film blowing, blow molding and so forth. Since the mechanical properties of the final product obtained depends on the thermomechanical history undergone by a polymer, it is imperative that one designs the mold or the process or both so that one achieves the desired mechanical properties. To do this, without resorting to expensive full scale experiments, one needs a model that is calibrated using a simpler set of experiments to predict the

orientation and the amount crystals. The models proposed should be able to aid in the design process.

REFERENCES

- [1] M. Abramowitz and I.A. Stegun, *Handbook of Mathematical Functions*. New York: Dover, 1965.
- [2] C.A. Angell, “The old problems of the glass and the glass transition, and the many new twists”, *Proc. Natl. Acad. Sci. U.S.A.*, vol. 92, pp. 6675-6682, 1995.
- [3] R.J. Atkin and N. Fox, *An Introduction to the Theory of Elasticity*. New York: Longman, 1980.
- [4] J.H. Bheda and J.E. Spruiell, “Dynamics and structure development during high speed melt spinning of nylon 6. I. On-line experimental measurements”, *J. Appl. Polym. Sci.*, vol. 39, pp. 447-463, 1990.
- [5] J. Brandrup and E.H. Immergut, *Polymer Handbook*. New York: Interscience, 1966.
- [6] V. Brucato, S. Piccarola, and V. La Carrubba, “An experimental methodology to study polymer crystallization under processing conditions. The influence of high cooling rates”, *Chem. Eng. Sci.*, vol. 57, pp. 4129-4143, 2002.
- [7] H.B. Callen, *Thermodynamics and an Introduction to Thermostatistics*. New York: Wiley, 1985.
- [8] C.H. Choi and J.L. White, “Correlation and modeling of the occurrence of different crystalline forms of isotactic polypropylene as a function of cooling rate and uniaxial stress in thin and thick parts”, *Polym. Eng. Sci.*, vol. 40, pp. 645-655, 2000.

- [9] B.T.F. Chung and V. Iyer, "Heat-transfer from moving fibers in melt spinning process", *J. Appl. Polym. Sci.*, vol. 20, pp. 367-376, 1976.
- [10] M.M. Denn, "Continuous drawing of liquids to form fibers", *Ann. Rev. Fluid Mech.*, vol. 12, pp. 365-387, 1980.
- [11] M.M. Denn, "Fiber spinning", in *Computational Analysis of Polymer Processing*, J.R.A. Pearson and S.M. Richardson, eds. New York: Applied Science, 1983.
- [12] M.M. Denn, "Correlations for transport coefficients in textile fiber spinning", *Ind. Eng. Chem. Fundam.*, vol. 35, pp. 2842-2843, 1996.
- [13] A.K. Doufas and A.J. McHugh, "Simulation of melt-spinning including flow-induced crystallization. Part III. Quantitative comparisons with PET spinline data", *J. Rheol.*, vol. 45, pp. 403-420, 2001.
- [14] A.K. Doufas, A.J. McHugh, and C. Miller, "Simulation of melt spinning including flow-induced crystallization Part I. Model development and predictions", *J. Non-Newtonian Fluid Mech.*, vol. 92, pp. 27-66, 2000.
- [15] A.K. Doufas, A.J. McHugh, C. Miller, and A. Immaneni, "Simulation of melt spinning including flow-induced crystallization Part II. Quantitative comparisons with industrial spinline data", *J. Non-Newtonian Fluid Mech.*, vol. 92, pp. 81-103, 2000.
- [16] P. Dreyfus and A. Keller, "A simple chain refolding scheme for the annealing behavior of polymer crystals", *Polymer Lett.*, vol. 8, pp. 253-258, 1970.
- [17] C. Eckart, "The thermodynamics of irreversible processes IV, the theory of elasticity and anelasticity", *Phys. Rev.*, vol. 73, pp. 373-382, 1948.

- [18] R.J. Fisher and M.M. Denn, "Mechanics of non-isothermal polymer melt spinning", *AIChE.*, vol. 23, pp. 23-28, 1977.
- [19] D.K. Gagon and M.M. Denn, "Computer simulation of steady polymer melt spinning", *Polym. Eng. Sci.*, vol. 21, pp. 844-853, 1981.
- [20] U. Gaur, S. Lau, B.B. Wunderlich, and B. Wunderlich, "Heat capacity and other thermodynamic properties of linear macromolecules. VIII. Polyesters and polyamides", *J. Phys. Chem. Ref. Data*, vol. 12, pp. 65-89, 1983.
- [21] H.H. George, "Model of steady-state melt spinning at intermediate take-up speeds", *Polym. Eng. Sci.*, vol. 22, pp. 292-299, 1982.
- [22] F. Gerardi, S. Piccarola, A. Martorana, and D. Sapoundjieva, "Study of the long-period changes in samples of isotactic poly(propylene) obtained by quenching from the melt and subsequent annealing at different temperatures", *Macromol. Chem. Phys.*, vol. 198, pp. 3979-3985, 1997.
- [23] S. Gogolewski, M. Gasiorek, K. Czerniawska, and A.J. Pennings, "Annealing of melt-crystallized nylon-6", *Colloid & Polymer Sci.*, vol. 260, pp. 859-863, 1982.
- [24] M. Gordon and I.H. Hillier, "Mechanism of secondary crystallization of polymethylene", *Phil. Mag.*, vol. 11, pp. 31-41, 1965.
- [25] A.E. Green and P.M. Naghdi, "On thermodynamics and nature of second law", *Proc. R. Soc. Lond. A.*, vol. 357, pp. 253-270, 1977.
- [26] N.V. Gvozdic and D.J. Meier, "On the melting temperature of syndiotactic polystyrene: 2. Enhancement of the melting temperature of semicrystalline polymers by a novel annealing procedure", *Polymer Communications*, vol. 32, pp. 493-494, 1991.

- [27] H. Haberkorn, K. Hahn, H. Breuer, H.D. Dorrer, and P. Matthies, "On the neck-like deformation in high-speed spun polyamides", *J. Appl. Polym. Sci.*, vol. 47, pp. 1551-1579, 1993.
- [28] G.M. Henson, D. Cao, S.E. Bechtel, and M.G. Forest, "A thin-filament melt spinning model with radial resolution of temperature and stress", *J. Rheol.*, vol. 42, pp. 329-360, 1998.
- [29] I.H. Hillier, "Modified Avrami equation for the bulk crystallization kinetics of spherulitic polymers", *J. Polymer Sci.*, vol. 3, pp. 3067-3078, 1965.
- [30] J.D. Humphrey and K.R. Rajagopal, "A constrained mixture model for growth and remodelling of soft tissues", *Math. Methods. Appl. Sci.*, vol. 12., pp. 407-430, 2003.
- [31] K. Kannan and K.R. Rajagopal, "Simulation of fiber spinning including flow induced crystallization", *J. Rheol.*, 2004 (Submitted).
- [32] K. Kannan, I.J. Rao, and K.R. Rajagopal, "A thermomechanical framework for the glass transition phenomenon in certain polymers and its application to fiber spinning", *J. Rheol.*, vol. 46, pp. 979-999, 2002.
- [33] S. Kase and T. Matsuo, "Studies on melt spinning II. Steady-state and transient solutions of fundamental equations compared with experimental results", *J. Appl. Polym. Sci.*, vol. 11, pp. 251-287, 1967.
- [34] K. Koyama, J. Suryadeva, and J.E. Spruiell, "Effect of molecular weight on high-speed melt spinning of nylon 6", *J. Appl. Polym. Sci.*, vol. 31, pp. 2203-2229, 1986.
- [35] A.Y. Malkin, A.E. Teishev, and M.A. Kutsenko, "Creep of polycarbonate: experiments and correlation with relaxation", *J. Appl. Polymer Sci.*, 45, 237-244

- (1992).
- [36] J.E. Mark and B. Erman, *Rubberlike Elasticity: A Molecular Primer*. New York: Wiley, 1988.
- [37] M. Matsui, "Air drag on a continuous filament in melt spinning", *Trans. Soc. Rheol.*, vol. 20, pp. 465-473, 1976.
- [38] T. Matsuo and S. Kase, "Studies on melt spinning: temperature profile within filament", *J. Appl. Polym. Sci.*, vol. 20, pp. 367-376, 1976.
- [39] J. Meissner, "Elongation of polymer melts-experimental methods and recent results", in *Proc. XIIth Int. Congr. on Rheology*, A. Ait-Kadi, J.M. Dealy, D.F. James, and M.C. Williams, eds. Quebec: Chemical Engineering Department, Laval University, Aug. 18-23, 1996, pp. 7-10.
- [40] J. Meissner and J. Hostettler, "A new elongational rheometer for polymer melts and other highly viscoelastic liquids", *Rheol Acta*, vol. 33, pp. 1-21, 1994.
- [41] W.V. Metanovski, *Compendium of Macromolecular Nomenclature*. Oxford: Blackwell Scientific Publications, 1991.
- [42] J. Murali Krishnan and K.R. Rajagopal, "A thermodynamic framework for the constitutive modeling of asphalt concrete: theory and applications", *J. Mater. Civ. Eng.*, vol.16, pp.155-166, 2004.
- [43] S. Murase, T. Matsuda, and M. Hiram, "Intrinsic birefringence of γ -form crystal of nylon 6: application of orientation development in high-speed spun fibers of nylon 6", *Macromol. Mater. Eng.*, vol. 286, pp. 48-51, 2001.
- [44] K. Nakamura, T. Watanabe, and K. Katayama, "Some aspects of nonisothermal crystallization of polymers. I. Relationship between crystallization temperature,

- crystallinity and cooling conditions”, *J. Appl. Polym. Sci.*, vol. 16, pp. 1077-1091, 1972.
- [45] J.G. Oldroyd, “On the formulation of rheological equation of state”, *Proc. Roy. Soc. London*, vol. A200, pp. 523-591, 1950.
- [46] K. Onaran and W.N. Findley, “Combined stress-creep experiments on a nonlinear viscoelastic material to determine the kernel functions for a multiple integral representation of creep”, *Trans. Soc. Rheol.*, vol. 9, pp. 299-327, 1965.
- [47] M.L. Ottone and J.A. Deiber, “Modeling the melt spinning of polyethylene terephthalate”, *J. Elastomers Plast.*, vol. 32, pp. 119-139, 2000.
- [48] M.J. Panik, *Classical Optimization: Foundations and Extensions*. Amsterdam, The Netherlands: North-Holland Publishing Company, 1976.
- [49] R.M. Patel, J.H. Bheda, and J.E. Spruiell, “Dynamics and structure development during high speed melt spinning of nylon 6. II. Mathematical modeling”, *J. Appl. Polym. Sci.*, vol. 42, pp. 1671-1682, 1991.
- [50] R.M. Patel and J.E. Spruiell, “Crystallization kinetics during polymer processing - analysis of available approaches for process modeling”, *Polym. Eng. Sci.*, vol. 31, pp. 730-738, 1991.
- [51] J.R.A. Pearson, *Mechanics of Polymer Processing*. London: Elsevier, 1985.
- [52] J. Petermann, M. Miles, and H. Gleiter, “Growth of polymer crystals during annealing”, *J. Macromol. Sci.*, vol. B12, pp. 393-404, 1976.
- [53] S. Piccarola, V. Brucato, and Z. Kiflie, “Non-isothermal crystallization kinetics of PET”, *Polym. Eng. Sci.*, vol. 40, pp. 1263-1272, 2000.

- [54] S. Piccarola, M. Saiu, V. Brucato, and G. Titomanlio, “Crystallization of polymer melts under fast cooling. II. High-purity iPP”, *J. Appl. Polymer Sci.*, vol. 46, pp. 625-634, 1992.
- [55] F.P. Price, “A phenomenological theory of spherulitic crystallization: primary and secondary crystallization processes”, *J. Polymer Sci.*, vol. 3, pp. 3079-3086, 1965.
- [56] R. Quinson, J. Perez, Y. Germain, and J.M. Murraciale, β - and α -relaxations in poly(methylmethacrylate) and polycarbonate: non-linear anelasticity studies by antistress relaxation. *Polymer*, vol. 36, pp. 743-752, 1995.
- [57] R. Quinson, J. Perez, M. Rink, and J. Pavan, “Yield criteria for amorphous glassy polymers”, *J. Mater. Sci.*, vol. 32, pp. 1371-1379, 1997.
- [58] K.R. Rajagopal, “Multiple configurations in continuum mechanics”, in *Report 6*. Pittsburgh: Institute of Computational and Applied Mechanics, University of Pittsburgh, 1995.
- [59] K.R. Rajagopal “On implicit constitutive theories”, *Appl. Math.*, vol. 48, pp. 279-319, 2003.
- [60] K.R. Rajagopal and N. Chandra, “A thermodynamic framework for the superplastic response of materials”, *Superplast. Adv. mater. ICSAM-2000 Mater. Sci. Forum*, vol. 357, pp. 261-271, 2001.
- [61] K.R. Rajagopal and A.R. Srinivasa, “On the inelastic behavior of solids-part I: twinning”, *Int. J. Plast.*, vol. 11, pp. 653-678, 1995.
- [62] K.R. Rajagopal and A.R. Srinivasa, “Inelastic behavior of materials-II: energetics associated with discontinuous twinning”, *Int. J. Plast.*, vol. 13, pp. 1-35, 1997.

- [63] K.R. Rajagopal and A.R. Srinivasa, “Mechanics of the inelastic behavior of materials - Part I, theoretical underpinnings”, *Int. J. Plast.*, vol. 118, pp. 945-967, 1998.
- [64] K.R. Rajagopal and A.R. Srinivasa, “Mechanics of the inelastic behavior of materials - Part II: inelastic response”, *Int. J. Plast.*, vol. 14, pp. 969-995, 1998.
- [65] K.R. Rajagopal and A.R. Srinivasa, “On the thermomechanics of shape memory wires”, *Z. Angew. Math. Phys.*, vol. 50, pp. 459-496, 1999.
- [66] K.R. Rajagopal and A.R. Srinivasa, “A thermodynamic framework for rate type fluid models”, *J. Non-Newtonian Fluid Mech.*, vol. 88, pp. 207-227, 2000.
- [67] K.R. Rajagopal and A.R. Srinivasa, “Modeling anisotropic fluids within the framework of bodies with multiple natural configurations”, *J. Non-Newtonian Fluid Mech.*, vol. 99, pp. 109-124, 2001.
- [68] K.R. Rajagopal and L. Tao, “Modeling of the microwave drying process of aqueous dielectrics”, *Z. Angew. Math. Phys.*, vol. 53, pp. 923-948, 2002.
- [69] K.R. Rajagopal and A.S. Wineman, “A constitutive equation for non-linear solids which undergo deformation induced microstructural changes”, *Int. J. Plast.*, vol. 8, pp. 385-395, 1992.
- [70] I.J. Rao, J.D. Humphrey, and K.R. Rajagopal, “Biological growth and remodeling: a uniaxial example with possible application to tendon and ligaments”, *Comput. Model. Eng. Sci.*, vol 4, pp. 439-455, 2003.
- [71] I.J. Rao, and K.R. Rajagopal, “Phenomenological modeling of polymer crystallization using the notion of multiple natural configurations”, *Interfaces Free Bound.*, vol. 2, pp. 73-94, 2000.

- [72] I.J. Rao, and K.R. Rajagopal, “A study of strain-induced crystallization in polymers”, *Int. J. Solids. Struct.*, vol. 38, pp. 1149-1169, 2001.
- [73] I.J. Rao and K.R. Rajagopal, “A thermodynamic framework for the study of crystallization in polymers”, *Z. Angew. Math. Phys.*, vol. 53, pp. 365-406, 2002.
- [74] M.J. Richardson and N.G. Savill, “Derivation of accurate glass transition temperatures by differential scanning calorimetry”, *Polymer*, vol. 16, pp. 753-757, 1975.
- [75] J.E. Spruiell and J.L. White, “Structure development during polymer processing: studies of the melt spinning of polyethylene and polypropylene fibers”, *Polym. Eng. Sci.*, vol. 15, pp. 660-667, 1975.
- [76] A.R. Srinivasa, “Flow characteristics of a “multiconfigurational”, shear thinning viscoelastic fluid with particular reference to the orthogonal rheometer”, *Theor. Comp. Fluid Dyn.*, vol. 13, pp. 305-325, 2000.
- [77] J. Sun, S. Subbiah, and J.M. Marchal, “Numerical analysis of nonisothermal viscoelastic melt spinning with ongoing crystallization”, *J. Non-Newtonian Fluid Mech.*, vol. 93, pp. 133-151, 2000.
- [78] R.I. Tanner, *Engineering Rheology*. New York: Oxford University Press, 1988.
- [79] P. Tidick, S. Fakirov, Avramova, and H.G. Zachmann, “Effect of the melt annealing time on the crystallization of nylon-6 with various molecular weights”, *Colloid & Polymer Sci.*, vol. 262, pp. 445-449, 1984.
- [80] A.V. Tobolsky, and H.F. Mark, *Polymer Science and Materials*. New York: Wiley, 1980.

- [81] L.R.G. Treloar, *The Physics of Rubber Elasticity*. Oxford: Clarendon Press, 1975.
- [82] G. Vassilatos, E.R. Schmelzer, and M.M. Denn, "Issues concerning the rate of heat-transfer from a spinline", *Int. Polym. Proc.*, vol. 7, pp. 144-150, 1992.
- [83] O. Verhoyen, F. Dupret, and R. Legras, "Isothermal and non-isothermal crystallization kinetics of polyethylene terephthalate: mathematical modeling and experimental measurement", *Polymer Eng. Sci.*, vol. 38, pp. 1594-1610, 1998.
- [84] F.M. White, *Fluid Mechanics*. New York: McGraw-Hill, 2003.
- [85] A.S. Wineman and K.R. Rajagopal, "On a constitutive theory for materials undergoing microstructural changes", *Arch. Mech.*, vol. 42, pp. 53-75, 1990.
- [86] B. Wunderlich, *Macromolecular Physics vol. III*. New York: Academic Press, 1980.
- [87] G.S.Y. Yeh, R. Hosemann, J. Loboda-Cackovic, and H. Cackovic, "Annealing effects of polymers and their underlying molecular mechanisms", *Polymer*, vol. 17, pp. 309-318, 1976.
- [88] A. Ziabicki, *Fundamentals of Fiber Formation*. London: Wiley, 1976.
- [89] K.F. Zieminski and J.E. Spruiell, "On-line studies and computer simulations of the melt spinning of nylon-66 filaments", *J. Appl. Polym. Sci.*, vol. 35, pp. 2223-2245, 1988.

VITA

Krishna Kannan was born on 12th September, 1973 in the southern Indian city of Madurai in the state of Tamilnadu. He grew up in Trichy, a city belonging to the same state. He received his high school education in the same city. He obtained his Bachelor of Engineering degree from PSG College of Technology, Coimbatore. He then travelled to College Station, Texas where he obtained a M.S. degree from Texas A&M University with a major in mechanical engineering. His permanent address is

C/O S.V. Kannan
Ankur Bob Classics
11-Rathnambal Street
Rangarajapuram main road
Chennai, Tamil Nadu 600024
India

The typist for this thesis was Krishna Kannan.